FINAL REPORT

DOE NEUP Project

RELAP-7 Application and Enhancement for FLEX Strategies and ATF Behavior under Extended Loss of AC Power Conditions

Dean Wang [1]

Karen Vierow Kirkland [2]

Hongbin Zhang [3]

Kevin R Robb [4]

[1] The Ohio State University

[2] Texas A&M University

[3] Idaho National Laboratory

[4] Oak Ridge National Laboratory

April 30, 2020

ABSTRACT

This report summarizes the results of a three-year research project sponsored by the U.S. Department of Energy (DOE) Nuclear Energy University Program (NEUP) to enhance and apply the RELAP-7 code by adding and improving several important components (e.g., a mechanistic Reactor Core Isolation Cooling (RCIC) system model) for thermal hydraulic studies of LWRs under ELAP conditions and evaluating the time available for transition to portable FLEX equipment. The project team included University of Massachusetts–Lowell, The Ohio State University, Texas A&M University, Idaho National Laboratory and Oak Ridge National Laboratory.

In the Fukushima accident, it was found that the RCIC system played a crucial role in delaying core meltdown by almost three days in Fukushima Daiichi Unit 2, because of self-regulated operation of the steam driven RCIC turbine-pump injection system. Steam flow in the convergent-divergent nozzles of the RCIC Terry turbine is two-phase non-equilibrium transonic flow with homogenous nucleation condensation. To more accurately predict the dynamic process and behavior of the transonic compressible steam flow, a one-dimensional transient two-phase analytical model is presented. A simplified four-fluid model was employed in the present work with the consideration of four separate fluid fields: vapor, liquid film, entrained droplets and condensed droplets. The mass, momentum and energy interactions between the fluids were considered and modeled. An extended seven-equation non-equilibrium critical flow model was developed to obtain the critical pressure and velocities of each phase at the nozzle throat. To predict the wetness in the divergent section, a mechanistic nucleation condensation model was integrated in the nozzle analysis model, considering the generation and consequent growth of droplets. The governing differential equations on a staggered grid were discretized using the second-order Lax-Wendroff scheme with a flux limiter, and the Semi-Implicit Method for Pressure-Linked Equation (SIMPLE) algorithm was employed to solve the discrete linear system. To demonstrate the predictability and reliability of the physical models and the numerical method proposed in the present work, three representative nozzles were modeled and simulated. The results show good agreement with the available experimental data, even for condensation shock. Then, the 1D nozzle model was employed to obtain nozzle flow tables of the Terry turbine nozzle for different working pressures which can cover the operation pressure range of the RCIC system.

A mechanistic RCIC turbine-pump system model was developed and implemented in the system code TRACE to simulate dynamic responses of the RCIC system under Beyond Design Basis Accident (BDBA) conditions. The turbine-pump governing equations are based on the control volume approach of the angular momentum balance. The physics based mechanistic RCIC model was developed using the TRACE control system components (i.e., signal variables, control blocks, and tables), and incorporated into a TRACE boiling water reactor (BWR) model. The TRACE model in this report has a detailed nodalization of the reactor pressure vessel (RPV), and all of the major flow paths and system components, including the safety relief valves (SRVs) and the containment suppression pool and drywell. Based on the nozzle flow tables generated from the 1D nozzle model developed, the turbine drive torque can be calculated from table lookup. Since the detailed specifications of the RCIC pump are

unavailable, the homologous curves for a Bingham pump were used in the current pump component. A station black-out (SBO) accident test problem was selected to demonstrate the TRACE RCIC model. The short-term SBO simulations were performed for two cladding materials: Zircaloy and FeCrAl, to demonstrate the effect of the accident tolerant fuel cladding on fuel heat-up under BDBA accident conditions.

The wetwell plays a vital safety role in SBO and other BWR accident scenarios in that it can reduce containment pressure and supply additional core make-up water. The suppression pool temperature distribution has a very large impact on both RPV and containment pressure. Thus, another novel contribution of the project comes mainly from an improved, systems-level wetwell model which can capture buoyancy-induced thermal stratification effects due to steam injection and condensation. A two-zone stratified wetwell model has been implemented in RELAP-7 and some results from that model are presented. This wetwell model is capable of simulating thermal stratification due to a low steam mass injection rate. With a low mass flow rate, the model assumes that all the steam condenses within the pipe and the resulting plume can be approximated with a purely buoyant, heat-source driven model. The wetwell model developed with these assumptions is adequate to simulate slow transients such as extended SBO transients.

ACKNOWLEDGEMENTS

We would like to thank the U.S. Department of Energy Office of Nuclear Energy for their support of this project through the Nuclear Energy University Program.

TABLE OF CONTENTS

Abstract *2*

ACKNOWLEDGEMENTS *5*

Table of Contents *6*

List of figures *8*

List of tables *10*

1. Introduction *11*

2. Development of Four-fluid Nozzle Analysis Model *13*

2.1 General description of physical models **13**

2.1.1 Fluid field conservation equations 13

2.1.2 Closure relations 15

2.2 Flow process and special models **19**

2.2.1 Critical flow model 19

2.2.2 Nucleation condensation model in flowing steam 22

2.2.3 Flashing model 25

2.3 Numerical method **26**

2.3.1 Discretization of conservation equations 27

2.3.2 Numerical solution 30

2.4 Summary **33**

3. Assessment of the Nozzle Model and Table Generation *35*

3.1 Benchmark with steam nozzle tests **35**

3.1.1 Analysis of Moore nozzle 35

3.1.2 Analysis of Barschdorff nozzle 37

3.2 Analysis of Kneass nozzle **40**

3.2.1 Validation with the test data 41

3.2.2 Comparison with FLUENT 43

3.2.3 Simulation of the flow with inlet droplets and high liquid fraction 47

3.3 Generation of nozzle flow tables **49**

3.4 Summary **51**

4. RCIC System-level Model Development and Implementation *52*

4.1 RCIC system description **52**

4.2 Terry turbine and pump model **54**

4.2.1 Terry Turbine model 54

4.2.2 Homologous pump model 57

4.3 TRACE model of RCIC system **58**

4.4 RCIC system model demonstration **62**

4.5 ATF demonstration **68**

4.6 Summary **73**

5. Development and Implementation of Stratified Wetwell Model ***74***

5.1 Pool thermal stratification **74**

5.1.1 Stably stratified criterion 75

5.1.2 Buoyant jets 77

5.2 Stratified Wetwell Model **83**

5.2.1 Pool heater experiment 87

5.2.2 POOLEX STB-20 Experiment 90

5.3 Summary **95**

6. Conclusions ***96***

References ***98***

Appendices ***103***

A. Program structure of nozzle two-phase model **103**

B. Nozzle steam flow tables **105**

C. List of publications supported by the project **112**

LIST OF FIGURES

Figure 2-1. Interactions between the fluids. 15
Figure 2-2. Transonic flow in convergence-divergence nozzle. 19
Figure 2-3. Implementation strategy for the condensation model. 25
Figure 2-4. Nucleation rate as a function of supercooling and pressure. 25
Figure 2-5. Liquid temperature and vapor temperature profiles. 26
Figure 2-6. Schematic of staggered grid. 27
Figure 2-7. Flowchart for the two-phase critical flow with condensation through a nozzle. 33
Figure 3-1. Geometry of Moore nozzle Type B. 35
Figure 3-2. Distributions of flow variables along the axis of Moore nozzle. 36
Figure 3-3. Distributions of condensation variables along the axis of Moore nozzle. 37
Figure 3-4. Geometry of Barschdorff nozzle. 38
Figure 3-5. Distributions of main flow parameters along the axis of Barschdorff nozzle. 39
Figure 3-6. Distributions of condensation variable along the axis of Barschdorff nozzle. 40
Figure 3-7. Geometry of Kneass nozzle. 41
Figure 3-8. Computational mesh for Kneass nozzle. 41
Figure 3-9. Comparison of static pressure distributions. 42
Figure 3-10. Pressure contours at cross-section plane of the calculated nozzle. 44
Figure 3-11. Velocity contours at cross-section plane of the calculated nozzle. 44
Figure 3-12. Temperature contours at cross-section plane of the calculated nozzle. 45
Figure 3-13. Wetness contours at cross-section plane of the calculated nozzle. 45
Figure 3-14. Comparison with FLUENT results (p_in=120psi). 46
Figure 3-15. Distributions of main variables along the nozzle axis. 47
Figure 3-16. Distributions of nucleation condensation along the nozzle axis. 47
Figure 3-17. Results of mixture inlet conditions. 49
Figure 3-18. High liquid fraction results. 49
Figure 3-19. Geometry of Terry turbine nozzle. 50
Figure 3-20. Distributions of main flow parameters along the axis of Terry nozzle. 51
Figure 4-1. Configuration of typical BWR RCIC system 53
Figure 4-2. Terry turbine drawing and configuration. 54
Figure 4-3. Control volume for angular momentum equation of Terry turbine. 55
Figure 4-4. TRACE SNAP model of BWR with the RCIC system. 59
Figure 4-5. TRACE nodalization of steam piping to RCIC and injection components. 60
Figure 4-6. Control system for RCIC pump-turbine calculation. 61
Figure 4-7. TRACE calculations of RPV pressure compared to Fukushima data. 62
Figure 4-8. TRACE evaluation of RPV pressure. 63
Figure 4-9. TRACE evaluation of reactor downcomer water level. 63
Figure 4-10. Calculated void fraction of channels and nozzle chamber. 64
Figure 4-11. TRACE calculations of Terry turbine exhaust discharge flow rates. 64
Figure 4-12. Calculated RCIC pump torque. 65
Figure 4-13. Calculated RCIC pump rotation speed. 65
Figure 4-14. Calculated RCIC pump loop mass flow rate. 66
Figure 4-15. Calculated mass flow rate of SRV. 66
Figure 4-16. Calculated liquid temperature of wetwell. 67
Figure 4-17. Calculated pressure of wetwell gas space. 67
Figure 4-18. Calculated liquid water mass of wetwell reservoir. 68
Figure 4-19. Bundle configuration 10×10 fuel assembly. 69
Figure 4-20. Specific heat of two cladding materials. 70

Figure 4-21. Density of two cladding materials. 70
Figure 4-22. Thermal conductivity of two cladding materials. 71
Figure 4-23. Collapsed water level of Downcomer. 72
Figure 4-24. Peak cladding temperatures (without RCIC operation). 72
Figure 4-25. Peak cladding temperature (with RCIC operation). 73
Figure 5-1. Sketch of development of a stratified environment due to a heat source, showing the motions in the plume and environment (Zhao, 2003). 75
Figure 5-2. Axisymmetric buoyant jet (Zhao, 2003). 78
Figure 5-3. RELAP-7's simplified wetwell model diagram (Berry et al., 2016). 83
Figure 5-4. Thermal stratification experiment in cylindrical water tank (Christensen and Peterson, 2001). 88
Figure 5-5. Comparison of the numerically and analytically calculated location of the first front. 90
Figure 5-6. Error in the numerically calculated first front position. 90
Figure 5-7. POOLEX test rig (Laine and Puustinen, 2005). 91
Figure 5-8. Measured vertical temperature distribution in the pool in STB-20 during the heating phase. 92
Figure 5-9. POOLEX thermocouple placement (Laine and Puustinen, 2005). 93
Figure 5-10. Simulation vertical temperature distributions at various times. 94
Figure 5-11. Pool temperature versus time comparison of the simulation and experimental results. 95

LIST OF TABLES

Table 2-1. Summary of the interfacial drag model. 16
Table 2-2. Basic conservation equations in Ransom-Trapp and Henry-Fauske models. 20
Table 2-3. Definitions of abbreviated variables. 21
Table 2-4. Modifications of TRACE flashing model. 26
Table 2-5. The velocity coefficient matrix and source term vector. 29
Table 2-6. Source terms in the mass and energy equations. 29
Table 2-7. SIMPLE algorithm for two-phase four-fluid flow. 31
Table 3-1. Comparison of velocities near nozzle exit 43
Table 4-1. Input values for TRACE pump ratings and turbine data 58
Table 4-2. Fuel and cladding dimensional design parameters. 69
Table 5-1. Test rig vs. Olkiluoto 1 and 2 BWRs (Laine and Puustinen, 2005). 91

1. INTRODUCTION

The RCIC system of BWR power plants consists of safety-related equipment intended to provide make-up coolant to the RPV when it is isolated from the power-producing steam turbine and condenser (Beeny, 2017). The RCIC system has received much attention in recent years from experimentalists such as those at POOLEX (Laine and Puustinen, 2005), SIET (Pellegrini, 2016), and the Nuclear Heat Transfer Lab (Solom, 2016). There have also been recent RCIC modeling efforts from researchers either creating original component models (original MELCOR turbine/pump models (Beeny, 2017), or from modifying existing flow models with additional boundary conditions and closure relations (effective momentum and energy source terms applied to GOTHIC (Li et al., 2011), tuning form loss coefficients in the TRACE VESSEL component (Okawa and Furuya, 2019). To more accurately understand the behavior of the RCIC system under BDBA conditions, one of the most important tasks is the modeling of two-phase critical flow through Terry turbine nozzles to obtain the nozzle outlet velocity and two-phase mixture composition. The modeling of the spontaneous nucleation condensation process is a key point to accurately predict the wetness of the nozzle flow.

Sandia National Laboratories developed and qualified a system-level model of a RCIC steam-turbine-pump to inform the design of experimental configurations using MELCOR and RELAP. CFD analyses of the Terry turbine model were also performed to complement the system-level modeling (Caroni et al., 2018). Kirkland et al. worked on modeling a quasi-two-fluid dispersed phase flow model using the STAR-CCM+ software and developing a Terry turbine mathematical model for implementation into the MELCOR code for system level analysis (Kirkland et al., 2017). Idaho National Laboratory proposed a set of analytical models for simulating normal operating conditions of Terry turbine nozzles with pure steam (Zhao et al., 2016). An adiabatic expansion process inside the nozzle was modeled. Then a modified version with a two-phase choking model and expansion model was developed to cover two-phase off-design conditions (Zhao and O'Brien, 2017).

The commercial CFD software has reached a very high level of maturity for simulating complicated single-phase flow phenomena. Some studies were attempted to simulate the nozzle flow using the CFD software in various industrial applications, such as the steam ejector in the refrigeration cycle (Ruangtrakoon et al., 2013; Geng et al., 2019), combustion unit with the winged nozzle (Law and Grimbun, 2019), conical and scarfed nozzle in the aerospace vehicle (Sushma et al., 2016), supersonic lance tip nozzles (Garajau et al., 2019). The simulation of wet-steam flows in low-pressure turbine was also performed by the integrated wet steam model in ANSYS FLUENT (Zori and Kelecy, 2005; Wróblewski et al., 2009; Halama and Fort, 2012). Nevertheless, flow simulations with high liquid contend through the nozzles are not attempted with the CFD software. The two-phase flow models used in these studies are geared toward dry and wet steam analysis, and not capable of assessing two-phase problems with high liquid content. However, it should be noted that high-fidelity CFD based two-phase flow simulation still remains a big challenge.

Current best-estimate thermal-hydraulic system codes, e.g., TRACE and RELAP5, have good principal capabilities to perform transient simulation and safety analysis of light water reactors

(Spore et al., 2000; Mesina, 2016). However, there are still some serious shortcomings in these codes for some special applications. For example, the simulation of the transonic two-phase flow needs new modeling capabilities such as throat choking and nucleation condensation. In addition, a robust numerical method has to be used to obtain accurate and stable results. Another consideration is that nearly all current systems-level wetwell models consider the water space to be single, lumped volume, thus assuming the water is thermally mixed. This assumption neglects the possibility that the wetwell can thermally stratify, which would limit its thermal and pressure suppression capacity.

Due to the deficiencies and limitations of current commercial CFD software and advanced system codes, there is a need to develop a specialized two-phase multi-field code with extended models for nozzle transonic flow analysis. In this report, we first present our work on the development of physical models and numerical methods for the two-phase transonic flow with nucleation condensation through a nozzle based on one-dimensional transient nonequilibrium four-fluid models. Then a novel physical-based RCIC system model was developed and implemented into the system-level code.

2. DEVELOPMENT OF FOUR-FLUID NOZZLE ANALYSIS MODEL

2.1 GENERAL DESCRIPTION OF PHYSICAL MODELS

2.1.1 FLUID FIELD CONSERVATION EQUATIONS

The present model employs a set of two-phase, four-fluid conservation equations in one dimension with varying flow area. Four separate fluid fields are considered: vapor, liquid film, entrained droplets and condensed droplets. In the current study, the steam wetness caused by the nucleation condensation is assumed very small. Due to huge density difference between the vapor phase and liquid phase, the volume fraction of the condensed droplets can be neglected. In addition, the diameter of the condensed droplets is very small, and they can be treated as passive scalars with the same speed as the surrounding vapor phase. To simplify the model, the vapor and condensed droplets are combined as a mixture in the continuity equation and momentum equation. Meanwhile, it should be noted that the liquid film and droplet fields are assumed to be in thermal equilibrium so that they share a common energy equation in this model. Eight conservation equations for one-dimensional transient two-phase flow are given as follows:

Mass conservation equations:

$$\frac{\partial\big((\alpha+\alpha_N)\rho_m A\big)}{\partial t}+\frac{\partial\big[(\alpha+\alpha_N)\rho_m A V_g\big]}{\partial x}=A\Gamma \tag{2-1}$$

$$\frac{\partial\big[\alpha_f\rho_f A\big]}{\partial t}+\frac{\partial\big[\alpha_f\rho_f V_f A\big]}{\partial x}=A[-(1-\eta)\Gamma-S] \tag{2-2}$$

$$\frac{\partial\big[\alpha_D\rho_f A\big]}{\partial t}+\frac{\partial\big[\alpha_D\rho_f V_D A\big]}{\partial x}=A[-\eta\Gamma+S] \tag{2-3}$$

Momentum conservation equations:

$$\frac{\partial\left((\alpha+\alpha_N)\rho_m A V_g\right)}{\partial t}+\frac{\partial\big[(\alpha+\alpha_N)\rho_m A V_g^2\big]}{\partial x}=A\left(-(\alpha+\alpha_N)\frac{\partial P}{\partial x}-F_{wg}-F_i-F_{iD}+\Gamma V_i\right) \tag{2-4}$$

$$\frac{\partial\big[\alpha_f\rho_f A V_f\big]}{\partial t}+\frac{\partial\big[\alpha_f\rho_f A V_f^2\big]}{\partial x}=A\left[-\alpha_f\frac{\partial P}{\partial x}-F_{wf}+F_i-(1-\eta)\Gamma V_i-SV_f\right] \tag{2-5}$$

$$\frac{\partial\big(\alpha_D\rho_f A V_D\big)}{\partial t}+\frac{\partial\big[\alpha_D\rho_f A V_D^2\big]}{\partial x}=A\left(-\alpha_D\frac{\partial P}{\partial x}+F_{iD}-\eta\Gamma V_i+SV_f\right) \tag{2-6}$$

Energy conservation equations:

$$\frac{\partial(\alpha\rho_g A h_g)}{\partial t}+\frac{\partial[\alpha\rho_g A h_g V_g]}{\partial x}=A\left(\alpha\frac{\partial P}{\partial t}+\alpha V_g\frac{\partial P}{\partial x}+q_{gi}'''+(\Gamma+\Gamma_N)h_g^*+q_{wg}\right) \tag{2-7}$$

$$\frac{\partial[(1-\alpha)\rho_f A h_f]}{\partial t}+\frac{\partial[(1-\alpha-\alpha_D-\alpha_N)\rho_f A h_f V_f]}{\partial x}+\frac{\partial[\alpha_D\rho_f A h_f V_D]}{\partial x}+\frac{\partial[\alpha_N\rho_f A h_f V_g]}{\partial x}$$

$$=A\left[(1-\alpha)\frac{\partial P}{\partial t}+(1-\alpha-\alpha_D-\alpha_N)V_f\frac{\partial P}{\partial x}+\alpha_D V_D\frac{\partial P}{\partial x}+\alpha_N V_g\frac{\partial P}{\partial x}+q_{fi}'''-(\Gamma+\Gamma_N)h_f^*+q_{wf}\right] \tag{2-8}$$

Note α, α_f, α_D and α_N are the volume fraction of vapor phase, liquid film, entrained droplets and condensed droplets, respectively. They satisfy the volume conservation closure, $\alpha+\alpha_f+\alpha_D+\alpha_N=1$; ρ_m is the mixture density of the vapor and condensed droplets, which is defined as $\rho_g/(1-\beta)$ and also used in the nucleation condensation model; Γ is the total phase-change rate except for nucleation condensation; Γ_N is the phase-change rate of nucleation condensation; S is the entrainment rate which is defined as S_E-S_D; F_i is the interfacial drag force between vapor and continuous liquid; F_{iD} is the interfacial drag force between vapor and droplets; F_{wk} is the wall drag force; V_i is the interphase velocity; q_{ki}''' is the interfacial heat transfer rate between liquid and vapor per unit volume; h_k^* is the saturation enthalpy of the phase change product or the enthalpy of the phase moving to the interface.

The parameter α_N equals to zero when the nucleation condensation is not triggered. Since the condensed droplets are assumed to have the same speed as the surrounding vapor phase, the volume fraction of the condensed droplets has the following relationship with the vapor volume fraction when the nucleation condensation occurs:

$$\alpha_N=\frac{\beta}{1-\beta}\frac{\rho_g}{\rho_f}\alpha \tag{2-9}$$

where β is the volume fraction of the condensed droplets, i.e., steam wetness, which is discussed in section 3.2.

The additional correlations are needed for each phase and coupled terms to close the above-mentioned governing equation system. The interfacial drag F_i, F_{iD} and the wall drag force F_{wk} per unit volume are expressed as

$$F_i=C_i|V_g-V_f|(V_g-V_f) \tag{2-10}$$

$$F_{iD}=C_{iD}|V_g-V_D|(V_g-V_D) \tag{2-11}$$

$$F_{wk}=-C_{wk}|V_k|V_k\ ;\ \ k=g,f \tag{2-12}$$

The phase-change rate Γ per unit volume can be evaluated from the interfacial heat transfer on the vapor and liquid sides, respectively. A thermal energy jump relation is defined by

$$\Gamma = \frac{-\left(q_{fi}''' + q_{gi}'''\right)}{h_g^* - h_f^*} \tag{2-13}$$

$$h_g^* - h_f^* = \begin{cases} h_{g,sat} - h_f, & \Gamma > 0 \\ h_g - h_{f,sat}, & \Gamma < 0 \end{cases} \tag{2-14}$$

$$q_{fi}''' = h_{fi} A_i'''\left(T_{sat} - T_f\right) + h_{flash} A_i'''\left(T_{sat} - T_f\right) \tag{2-15}$$

$$q_{gi}''' = h_{gi} A_i'''\left(T_{sat} - T_g\right) \tag{2-16}$$

The η term represents the fraction of phase change occurring between the vapor phase and liquid phase. To distribute the phase changing fraction of the continuous liquid and entrained droplets, Γ is multiplied by $1-\eta$ and η for the continuous liquid and entrained droplets, respectively. In the present work, the wall heat transfer can be neglected. The definition of η for the case of phase change is expressed as

$$\eta = \frac{\alpha_D}{1 - \alpha - \alpha_N} \tag{2-17}$$

2.1.2 CLOSURE RELATIONS

Figure 2-1 summarizes the interactions between the continuous liquid (F), vapor (V), entrained droplets (D) and condensed droplets (N). The solid lines represent the mass, momentum and energy exchanges due to phase change or entrainment, while the dash lines represent the interfacial drag and heat transfer between fluids. Meanwhile, the wall drag should be considered for the continuous liquid and vapor.

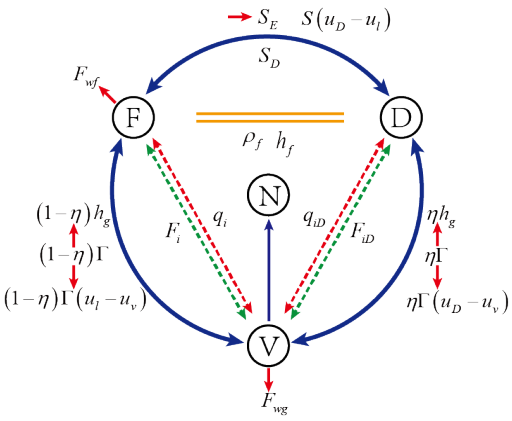

Figure 2-1. Interactions between the fluids.

The general concurrent two-phase flow models usually consider four principal flow regimes, which includes dispersed bubble, slug flow, cap bubble, and annular/mist flow (Cheng et al., 2008). The present work focuses on the annular/mist flow in the convergent-divergent nozzle.

Most of the closure relations are based on the models in the TRACE code (NRC, 2010), and are modified and extended for the four-fluid conservation equation system used in the nozzle model.

As shown in the field equations, the vapor, continuous liquid and droplet field momentum equations include the terms for the interfacial drag force and wall friction force. Therefore, to close the momentum equations, these drag force models should be specified. The interfacial mass transfer rate consists of the phase changing from the interfacial heat transfer and the spontaneous nucleation condensation. The former one is also tightly associated with the energy equations of each phase. Therefore, the interfacial heat transfer model should be specified for the closure of mass and energy conservative equations.

The library function of IAPWS-IF97 was utilized, which provides the state variable data for saturated, super-saturated, and superheated steam as well as saturated and sub-cooled water (Wagner and Kretzschmar, 2008). The density, dynamic viscosity, specific enthalpy, and thermal conductivity are the functions of both temperature and pressure, which are incorporated in the present model. Other properties like isobaric and isochoric specific heat and property derivatives are obtained from numerical differentiation or integration.

a) Interfacial drag

The interfacial drag is not only considered between the vapor and liquid film but also between the vapor and droplets in the TRACE code for the annular/mist flow regime. The difference between the TRACE model and the present nozzle model is the droplet field calculation. In TRACE, the fraction of droplets is obtained by an entrainment model and combined with the continuous liquid fluid. But in present work, the droplet is treated as an individual field and the droplet volume fraction can be obtained from the solution of the conservation equations. The fraction of droplets is determined by both the inlet condition and entrainment phenomena. Therefore, the interfacial drag between the film and vapor and the interfacial drag between the vapor and droplets are calculated separately. Table 2-1 summarizes the interfacial momentum transfer and wall friction used in the present analysis model.

Table 2-1. Summary of the interfacial drag model.

Term	Continuous liquid	Droplets
Interfacial drag coefficient	$C_{i,film} = f_{i,film} A'''_{i,film} \cdot \frac{1}{2}\rho_g$	$C_{i,D} = f_{i,D} A'''_{i,D} \cdot \frac{1}{2}\rho_g$
Area per unit volume	$A'''_{i,film} = \frac{4}{D_h}\sqrt{\alpha + \alpha_d} \approx \frac{4}{D_h}\sqrt{\alpha}$	$A'''_{i,d} = \frac{6}{4}\frac{\alpha_c \alpha_d}{d_d} = \frac{3}{2}\frac{\alpha\ \alpha_d}{(1-\alpha_d)d_d}$
Drag coefficient	$f_{i,film} = 0.005[1 + 75(1-\alpha)]$	$f_{i,D} = \frac{24}{Re_d}\left(1 + 0.1 Re_d^{0.75}\right);$

It should be carefully noted that the interfacial drag model between droplets and vapor in the nozzle analysis is different from that of the "six equations" two-fluid model. On one hand, the nozzle model can obtain the velocity of droplets from the droplet momentum equation while it

is unavailable in the conventional two-fluid model. The two-fluid model usually calculates the droplet drag by the velocity estimated from the entrainment rate correlation. On the other hand, the vapor in the nozzle usually reaches supersonic flow. This leads to a large Reynolds number which exceeds the applicable range of the drag model correlations, especially the following droplet diameter correlation (Kataoka et al., 1983):

$$D_d = 0.028\left(\frac{\sigma}{\rho_g j_g^2}\right) Re_f^{-1/6}\, Re_g^{2/3} \left(\frac{\mu_g}{\mu_l}\right)^{2/3} \left(\frac{\rho_g}{\rho_l}\right)^{-1/3} \tag{2-18}$$

The droplet size is important in the mechanistic modeling of the annular/mist flow. From Eq. 2-18, it is seen that the droplet diameter is sensitive to the vapor velocity. Eq. 2-18 is not applicable for nozzle two-phase flow, and it would predict a unrealistically small droplet size for high-speed nozzle flow. For simplicity it is assumed in this study that the entrained droplets have the same size as the nozzle inlet droplets.

b) Entrainment and Detrainment models

In the steam flow through nozzles, only the concurrent flow case is considered. The mechanism of the entrainment is a relationship between the surface tension and pressure differential. Some studies were done on correlating the air-water entrainment data as a function of interfacial shear stress, and then the correlation was modified by the dimensionless velocity to correlate data for the steam-water mixture. The following correlation (Wurtz, 1978) can be employed for predicting the entrainment rate in the concurrent flow, which is also adopted in the CTF code (Avramova et al., 2016):

$$S_E = \left[\frac{k_s \tau_i V_g \mu_f}{\sigma^2}\right] P_w \Delta x \tag{2-19}$$

where k_s is the roughness parameter, which is a function of the thickness of the liquid film.

The correlation of Cousins (Cousins, 1965), is used to calculate the detrainment rate of droplets in the present model. The detrainment from the droplets to the continuous liquids film is caused by the random turbulent motions.

$$S_D = k_0 C P_w \Delta x \tag{2-20}$$

where C is the droplet concentration, a main parameter in the gradient diffusion model in the above correlation; k_0 is the mass transfer coefficient, which is a function of the surface tension.

c) Interfacial heat transfer

As discussed earlier, the interfacial heat transfer models are required to obtain the energy exchange and phase changing rate, which is essential for the closure of both mass and energy equations. These interfacial heat coefficients and areas are strongly dependent on the specific flow regime. As pointed out previously, this study focuses on the annual/mist regime. The heat transfer from the continuous film and central region droplets to the vapor field are considered

and modeled separately. The interfacial heat transfer coefficients and interfacial areas are calculated together and then combined as

$$\left(h_{fi}A_i'''\right)_{AM} = h_{fi,film}A_{i,film}''' + h_{fi,drops}A_{i,drops}''' \tag{2-21}$$

$$\left(h_{gi}A_i'''\right)_{AM} = h_{gi,film}A_{i,film}''' + h_{gi,drops}A_{i,drops}''' \tag{2-22}$$

Equations 2-21 and 2-22 calculate the interfacial area of the continuous liquid film and droplets. The hydraulic diameter and volume fraction of vapor and droplets are adopted to calculate the continuous liquid interfacial area. In some cases, the channel surface is partially wetted, then a fraction factor is needed to modify the interfacial area. The interfacial area of the droplet field is calculated by the droplet volume fraction and diameter.

$$A_{i,film}''' = \frac{4}{D_h}\sqrt{\alpha + \alpha_d} \cdot f_{wet} \approx \frac{4}{D_h}\sqrt{\alpha} \cdot f_{wet} \tag{2-23}$$

$$A_{i,drops}''' = \frac{6\,\alpha\,\alpha_D}{(1-\alpha_D)D_D} \approx \frac{6\,\alpha_D}{D_D} \tag{2-24}$$

The Nusselt number of the liquid film is determined by the maximum value in the turbulent convection modified Dittus-Boelter correlation and a constant value is used for the laminar flow. The Nusselt number of the vapor side droplets is calculated using the Ryskin correlation (Kronig and Brink, 1950). The droplet velocity calculated from the droplet conservation equation set is used instead of that from the correlation in TRACE.

$$Nu_{gi,film} = max\left[4, 0.023 \cdot Re_c^{0.8} \cdot Pr_g^{0.4}\right] \tag{2-25}$$

$$Nu_{gi,drops} = 2 + 0.92\sqrt{V_{max}^* \cdot Pe} \quad and \quad 0.1 \le Nu_{gi,drops} \le 500 \tag{2-26}$$

For the liquid side interfacial heat transfer, both the laminar and turbulent film flow need to be considered. To make the correlation suitable for a wide range of Re numbers, the power-law weighting is utilized to average the Nu number of the two parts.

$$Nu_{fi,film} = \left[\left(Nu_{fi,lam}\right)^2 + \left(Nu_{fi,turb}\right)^2\right]^{1/2} \tag{2-27}$$

The Kuhn-Schrock-Peterson empirical correlation (Kuhn et al., 1994) is modified for the interfacial heat transfer of laminar films:

$$Nu_{fi,lam} = 2\left(1 + 1.83 \times 10^{-4} Re_{2\Phi,f}\right) \tag{2-28}$$

The Gnielinski correlation (Paleev and Filippovich, 1966) multiplied by 0.7 is adopted for the interfacial heat transfer of turbulent film:

$$Nu_{fi,turb} = 0.7\frac{f \cdot \left[\max\left(Re_{2\Phi,f}, 1000\right) - 1000\right] \cdot \max\left(0.5, Pr_f\right)}{1.0 + 12.7\sqrt{f} \cdot \left(\left[\max\left(0.5, Pr_f\right)\right]^{2/3} - 1\right)} \tag{2-29}$$

2.2 FLOW PROCESS AND SPECIAL MODELS

The two-phase compressible flow through the convergent-divergent nozzle is a challenging field of research for its unique flow phenomena. The first special process is the throat choking flow, which is a vital process in the nozzle transonic flow. The rapid expansion and depressurization of the steam flow lead to the subcooling of the dry vapor. Then the spontaneous nucleation condensation may be triggered due to the supersaturation and the wet steam flow will occur. In some situations, the liquid may be superheated due to the drastically reduced pressure and then the flashing process will occur. The thermodynamics of the steam nozzle flow are illustrated in Fig. 2-2.

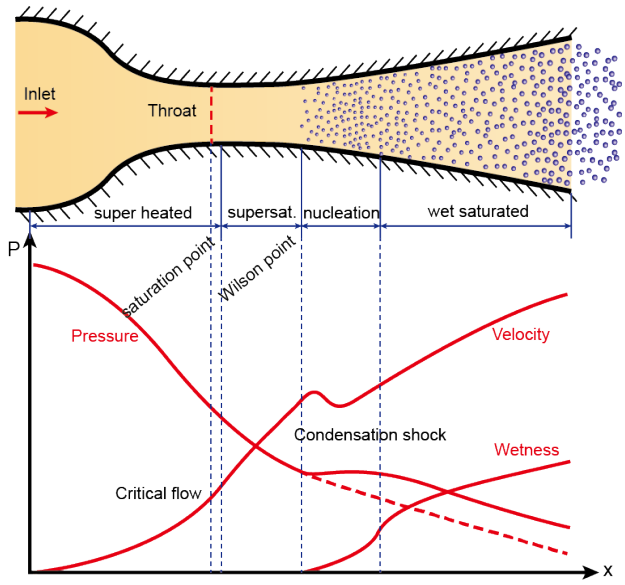

Figure 2-2. Transonic flow in convergence-divergence nozzle.

2.2.1 CRITICAL FLOW MODEL

The critical flow, especially two-phase critical flow, has been investigated by many researchers. A series of two-phase critical models were proposed. In general, two-phase critical models can be classified into two categories: thermodynamic equilibrium models and non-thermodynamic equilibrium models. The first category can be divided into homogeneous and non-homogenous models while the second one can be divided into "frozen" theories and non-homogenous models. The Henry-Fauske model (Henry and Fauske, 1971) and the Ransom-Trapp model (Trapp and Ransom, 1982) are the representative ones in this subcategory, both implemented in RELAP5 and TRACE (Sokolowski and Kozlowski, 2010). Table 2-2 summarized the basic conservation equations in these models.

Table 2-2. Basic conservation equations in Ransom-Trapp and Henry-Fauske models.

	Model	Conservation equations
Ransom-Trapp	Frozen model	Mixture mass eq.
		Vapor momentum eq.
		Liquid momentum eq.
		Mixture energy eq.
	Non-homogeneous model	Vapor mass continuity eq.
		Liquid mass continuity eq.
		Mixture momentum eq.
		Vapor entropy eq.
		Liquid entropy eq.
Henry-Fauske	Frozen model	Mixture mass eq.
		Mixture momentum eq.
	Non-homogeneous model	Vapor continuity eq.
		Liquid continuity eq.
		Mixture momentum eq.

The RELAP5 code uses the Henry-Fauske critical flow model as the default critical flow model (Ransom et al., 2001). The principal assumption in this model is that the phase velocities are equal, i.e., the slip between the phases is ignored. This can lead to an over-prediction of the mass flow rate under critical flow conditions. A characteristic analysis approach of a two-fluid model was proposed by Ransom and Trapp which includes the terms of phasic acceleration and mass transfer. The frozen flow assumption was employed. This two-fluid model includes a mixture mass conservation equation, momentum equations for each phase, and a mixture energy equation. In the current nozzle model, it is postulated that the nucleation condensation is only triggered in the downstream of the throat. Therefore, the condensed droplets are not considered in the critical model. To extend the two-fluid critical flow model to a three-fluid format, a seven-equation set is established, including three mass conservation equations, three momentum equations for each fluid and a mixture energy equation. Since the nondifferential terms are not invoked in the characteristic analysis, the conservation equation set of the three-fluid critical model can be written as

$$\frac{\partial(\alpha\rho_g)}{\partial t}+\frac{\partial(\alpha\rho_g V_g)}{\partial x}=0 \tag{2-30}$$

$$\frac{\partial(\alpha_f\rho_f)}{\partial t}+\frac{\partial(\alpha_f\rho_f V_f)}{\partial x}=0 \tag{2-31}$$

$$\frac{\partial(\alpha_D\rho_f)}{\partial t}+\frac{\partial(\alpha_D\rho_f V_D)}{\partial x}=0 \tag{2-32}$$

$$\alpha\rho_g\left[\frac{\partial V_g}{\partial t}+V_g\frac{\partial V_g}{\partial x}\right]+\alpha\frac{\partial P}{\partial x}+C_{gf}\alpha\alpha_f\rho_{mgf}\left[\frac{\partial V_g}{\partial t}+V_f\frac{\partial V_g}{\partial x}-\frac{\partial V_f}{\partial t}-V_g\frac{\partial V_f}{\partial x}\right]$$
$$+C_{gd}\alpha\alpha_D\rho_{mgd}\left[\frac{\partial V_g}{\partial t}+V_D\frac{\partial V_g}{\partial x}-\frac{\partial V_D}{\partial t}-V_g\frac{\partial V_D}{\partial x}\right]=0 \tag{2-33}$$

$$\alpha_f \rho_f \left[\frac{\partial V_f}{\partial t} + V_f \frac{\partial V_f}{\partial x}\right] + \alpha_f \frac{\partial P}{\partial x} + C_{gf} \alpha \alpha_f \rho_{mgf} \left[\frac{\partial V_f}{\partial t} + V_g \frac{\partial V_f}{\partial x} - \frac{\partial V_g}{\partial t} - V_f \frac{\partial V_g}{\partial x}\right] = 0 \qquad (2\text{-}34)$$

$$\alpha_D \rho_f \left[\frac{\partial V_D}{\partial t} + V_D \frac{\partial V_D}{\partial x}\right] + \alpha_D \frac{\partial P}{\partial x} + C_{gd} \alpha \alpha_D \rho_{mgd} \left[\frac{\partial V_D}{\partial t} + V_g \frac{\partial V_D}{\partial x} - \frac{\partial V_g}{\partial t} - V_D \frac{\partial V_g}{\partial x}\right] = 0 \qquad (2\text{-}35)$$

$$\frac{\partial\left(\alpha \rho_g s_g + (1-\alpha)\rho_f s_f\right)}{\partial t} + \frac{\partial\left[\alpha \rho_g V_g s_g + \alpha_f \rho_f V_f s_f + \alpha_D \rho_f V_D s_f\right]}{\partial x} = 0 \qquad (2\text{-}36)$$

where C is the virtual mass coefficient. s is the specific entropy and the subscript m refer to the total mixture. In the thermal equilibrium case, Eqs. 2-30 to 2-36 can be written in terms of P, α, α_l, α_D, V_g, V_l and V_D, as seven quasi-liner first order partial differential equations:

$$\mathbf{A}(\Phi)\frac{\partial \Phi}{\partial \mathrm{t}} + \mathbf{B}(\Phi)\frac{\partial \Phi}{\partial \mathrm{x}} = 0 \qquad (2\text{-}37)$$

where $\Phi = [P, \alpha, \alpha_f, \alpha_D, V_g, V_f, V_D]^T$, $\boldsymbol{A}(\Phi)$ and $\boldsymbol{B}(\Phi)$ are the 7×7 matrices in terms of Φ.

$$A = \begin{bmatrix} \alpha\rho_g^* & \rho_g & 0 & 0 & 0 & 0 & 0 \\ \alpha_f\rho_f^* & 0 & \rho_f & 0 & 0 & 0 & 0 \\ \alpha_D\rho_f^* & 0 & 0 & \rho_f & 0 & 0 & 0 \\ 0 & 0 & 0 & 0 & \begin{pmatrix}\alpha\rho_g + C_{gf}\alpha\alpha_f\rho_{mgf} \\ +C_{gD}\alpha\alpha_D\rho_{mgD}\end{pmatrix} & -C_{gf}\alpha\alpha_f\rho_{mgf} & -C_{gD}\alpha\alpha_D\rho_{mgD} \\ 0 & 0 & 0 & 0 & -C_{gf}\alpha\alpha_f\rho_{mgf} & \alpha_f\rho_f + C_{gf}\alpha\alpha_f\rho_{mgf} & 0 \\ 0 & 0 & 0 & 0 & -C_{gD}\alpha\alpha_D\rho_{mgD} & 0 & \alpha_D\rho_f + C_{gD}\alpha\alpha_D\rho_{mgD} \\ \alpha B_g^* + (1-\alpha)B_f^* & \rho_g s_g - \rho_f s_f & 0 & 0 & 0 & 0 & 0 \end{bmatrix} \qquad (2\text{-}38)$$

$$B = \begin{bmatrix} \alpha V_g\rho_g^* & \rho_g V_g & 0 & 0 & \alpha\rho_g & 0 & 0 \\ \alpha_f V_f\rho_f^* & 0 & \rho_f V_f & 0 & 0 & \alpha_f\rho_f & 0 \\ \alpha_D V_D\rho_f^* & 0 & 0 & \rho_f V_D & 0 & 0 & \alpha_D\rho_f \\ \alpha & 0 & 0 & 0 & \begin{pmatrix}\alpha\rho_g V_g + C_{gf}\alpha\alpha_f\rho_{mgf}V_f \\ +C_{gD}\alpha\alpha_D\rho_{mgD}V_D\end{pmatrix} & -C_{gf}\alpha\alpha_f\rho_{mgf}V_g & -C_{gD}\alpha\alpha_D\rho_{mgD}V_g \\ \alpha_f & 0 & 0 & 0 & -C_{gf}\alpha\alpha_f\rho_{mgf}V_f & \begin{pmatrix}\alpha_f\rho_f V_f \\ +C_{gf}\alpha\alpha_f\rho_{mgf}V_g\end{pmatrix} & 0 \\ \alpha_D & 0 & 0 & 0 & -C_{gD}\alpha\alpha_D\rho_{mgD}V_D & 0 & \begin{pmatrix}\alpha_D\rho_f V_D \\ +C_{gD}\alpha\alpha_D\rho_{mgD}V_g\end{pmatrix} \\ \begin{pmatrix}\alpha V_g B_g^* + \alpha_f V_f B_f^* \\ +\alpha_D V_D B_f^*\end{pmatrix} & \begin{pmatrix}\rho_g V_g s_g \\ -\rho_f V_f s_f\end{pmatrix} & 0 & \begin{pmatrix}\rho_f V_D s_f \\ -\rho_f V_f s_f\end{pmatrix} & \alpha\rho_g s_g & \alpha_f\rho_f s_f & \alpha_D\rho_f s_f \end{bmatrix} \qquad (2\text{-}39)$$

The variables with the superscript of stars are defined as follows:

Table 2-3. Definitions of abbreviated variables.

Vapor	Liquid
$\rho_g^* = \frac{\partial \rho_g}{\partial P}$	$\rho_f^* = \frac{\partial \rho_f}{\partial P}$
$s_g^* = \frac{1}{T}\left(\frac{\partial e_g}{\partial P} - \frac{p}{\rho_g^2}\frac{\partial \rho_g}{\partial P}\right)$	$s_f^* = \frac{1}{T}\left(\frac{\partial e_f}{\partial P} - \frac{p}{\rho_f^2}\frac{\partial \rho_f}{\partial P}\right)$
$B_g^* = \rho_g s_g^* + s_g \rho_g^*$	$B_f^* = \rho_f s_f^* + s_f \rho_f^*$

The characteristic velocities of the system are the roots of the following characteristic function. The choking velocities of vapor, continuous liquid and droplet phases can be obtained when the minimum value of the real part of all the characteristic roots λ is zero.

$$\det(\mathbf{A}\lambda - \mathbf{B}) = 0 \tag{2-40}$$

$$\min\,[\mathrm{Real}(\lambda)] = 0 \tag{2-41}$$

It is infeasible to solve Eq. 2-40 analytically, only except for very simple cases. Instead, the characteristic roots are obtained numerically. The detailed calculation sequence of the proposed critical model is described in Section 2.3.

2.2.2 NUCLEATION CONDENSATION MODEL IN FLOWING STEAM

When the steam undergoes a significant depressurization, it could become supersaturated during rapid expansion, resulting in homogeneous nucleation condensation. The homogenous nucleation process can be assumed to be instantaneous when the vapor thermal condition reaches the Wilson line and the nucleation delay time can be negligibly small as compared to the usual duration of the expansion process. For the non-equilibrium condensing steam flow through nozzles, numerical studies have also been carried out for the Laval nozzle and transonic steam turbine blades.

A project named as "International Wet Steam Modeling Project" was focused on reviewing the ability of numerical methods to calculate steam flows with condensation (Starzmann et al., 2018). Zori and Kelecy (2005) implemented a two-phase wet-steam model in a general-purpose CFD solver and a phase-change model based on the classical nucleation theory was developed to define the homogeneous non-equilibrium condensation process. Yang et al. (2017) developed a mathematical model to predict the condensation phenomenon in the supersonic flow. The steam condensation characteristics were described in detail. Kim et al. (2017) carried out a numerical analysis of steam condensation flows in various nozzles using their in-house code T-Flow, which has a non-equilibrium wet-steam model implemented. Yousefi Rad and Mahpeykar (2017) developed a novel hybrid approach for the simulation of the Laval nozzle and steam turbine blades, taking advantage of both difference scheme (scalar) and upstream scheme (convective upstream pressure splitting). Pandey (2014) developed a completely Eulerian model with equations of nucleation and droplet growth to solve the supersonic wet steam flow. Some other experimental and numerical studies can also be found in the references (Chen et al., 2019, 2020; Wróblewski et al., 2009).

In the present work, the classic nucleation condensation model was adopted and coupled with the general flow calculation. A one-dimensional wet steam theory in the Eulerian framework to predict non-equilibrium condensation effects in the divergent part of the nozzle was developed. In this model, the two-phase flow with condensation was considered as the condensing steam flowing along with the growth of liquid phase.

a) Steam flow model with nucleation condensation

In the present work, two additional scalar equations to model the nucleation condensation phenomenon in the steam flow are added to the three-fluid conservation equation system, representing droplet generation and interfacial mass transfer. This method is also adopted in the FLUENT software (Ansys Inc., 2015). The conservation equations of the steam flow are solved first to obtain the main flow parameters, then the condensation model is calculated sequentially to predict the condensation rate and wetness of the steam.

The condensed droplet phase is calculated by the mass fraction conservation equation. The droplet mass fraction (β), i.e. steam wetness, is utilized as the calculated variable.

$$\frac{\partial(\rho_m A\beta)}{\partial t} + \frac{\partial\left(\rho_m A V_g \beta\right)}{\partial x} = A\Gamma_N \tag{2-42}$$

where Γ_N is the mass generation rate due to spontaneous nucleation condensation, which is different from the main conservation equation set of the nozzle.

Both FLUENT and SolidWorks suggest that these two-phase treatments should be limited to problems where the liquid mass fraction remains below 20% (Ross et al., 2015). Above 20% mass fraction, the wet steam approximation (i.e. liquid particles passively advect in steam) starts to become invalid.

The droplet number density (only considering the ones formed by spontaneous nucleation), η, is calculated by the second scalar equation as following:

$$\frac{\partial(\rho_m A\eta)}{\partial t} + \frac{\partial\left(\rho_m A V_g \eta\right)}{\partial x} = A\rho_m I \tag{2-43}$$

where I is the nucleation rate, which means the number of droplets generated per unit volume per second.

b) Homogeneous nucleation model and droplet growth model

The classical homogenous nucleation theory is based on the Gibbs free enthalpy change during reversible formation of droplets and equilibrium number of clusters (McDonald, 1962, 1963). A particular nonequilibrium distribution of clusters is assumed to exist and a net flux of clusters growing to and beyond the critical size. The corresponding net flux of growth yields the nucleation rate. The correlation of the nucleation rate from the reference (Young, 1992) is adopted in the current implementation, and is modified for non-isothermal effects as

$$I = \frac{q_c}{1+\theta}\frac{\rho_g^2}{\rho_l}\sqrt{\frac{2\sigma}{M_m^3\pi}}\,e^{-\left(\frac{4\pi r_*^2\sigma}{3k_B T}\right)} \tag{2-44}$$

where qc is the evaporation coefficient, kB is the Boltzmann constant, Mm is the real mass of one water molecule. Considering the non-isothermal effects in the steam flow, the non-isothermal correction factor can be defined as

$$\theta = \frac{2(\gamma - 1)}{\gamma + 1}\frac{h_{lv}}{RT}\left(\frac{h_{lv}}{RT} - 0.5\right) \tag{2-45}$$

where h_{lv} is latent heat, γ is the ratio of the specific heats and R is the ideal gas constant.

The critical droplet radius is the criteria of the growth and evaporation of the droplet, which is defined as

$$r_* = \frac{2\sigma}{\rho_l RTlnS} \tag{2-46}$$

The supersaturation ratio, S, plays an important role in the spontaneous nucleation condensation phenomenon. It is the ratio of the real static pressure to the saturation pressure:

$$S = \frac{P}{P_{sat}(T)} \tag{2-47}$$

There are two mechanisms of the mass generate rate, Γ. One is the generation of nucleation and the other one is the droplet growth/demise. The total mass generation rate in the steam flow can be defined as

$$\Gamma = \frac{4}{3}\pi\rho_l I r_*^3 + 4\pi\rho_l \eta \bar{r}^2 \frac{\partial \bar{r}}{\partial t} \tag{2-48}$$

The formed droplet will further grow by condensation of vapor on their surface. The rate of condensation on the droplet is governed by the latent heat release rate carried away from the surface into the subcooling vapor, which is driven by the temperature difference. The correlation of the droplet growth rate from FLUENT is adopted in the present study.

$$\frac{\partial \bar{r}}{\partial t} = \frac{P}{h_{lv}\rho_l\sqrt{2\pi RT}}\frac{\gamma + 1}{2\gamma}C_p(T_s - T) \tag{2-49}$$

The two scalar equations describing the nucleation condensation phenomenon and the main conservation equation set are solved separately. Figure 2-3 presents the implementation strategy of the condensation model.

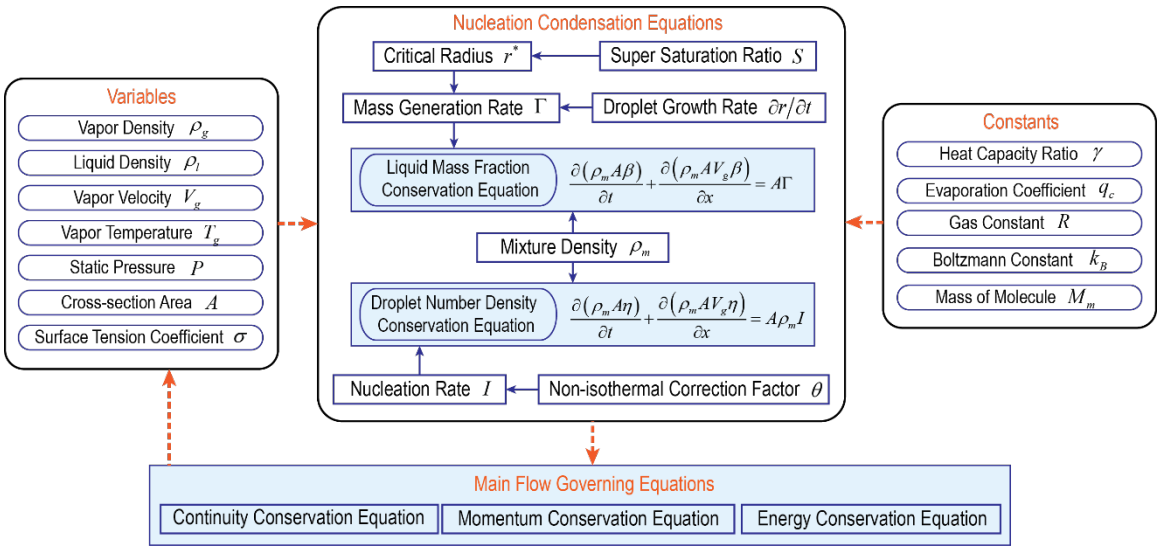

Figure 2-3. Implementation strategy for the condensation model.

The minimum supercooling temperature for the occurrence of condensation is calculated by the interpolation and extrapolation of the values in Fig. 2-4 (Moore and Sieverding, 1976). The curves of I for various pressures reveal that the nucleation rate rises from negligibly small values at low and moderate supercooling to significant values within a relatively slight change of ΔT. Indeed the observed sudden occurrence of spontaneous nucleation can be explained by this fast rise of the nucleation rate. The supercooling temperature values, at which a certain value of nucleation rate is reached, is a function of pressure.

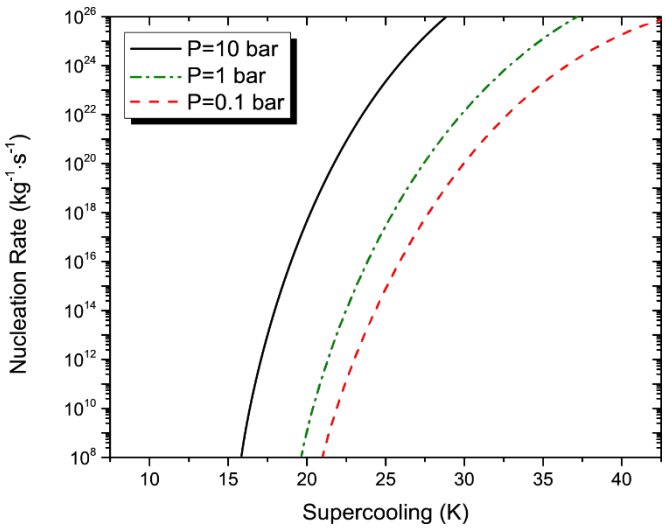

Figure 2-4. Nucleation rate as a function of supercooling and pressure.

2.2.3 FLASHING MODEL

Flash evaporation occurs when a saturated liquid stream has a depressurization by passing through a throttling device. It is an important phenomenon in the nozzle steam flow. The rapid evaporation of the liquid phase can keep it from becoming highly superheated. The following

equations is extracted from the TRACE flashing model (NRC, 2010), which is independent of the flow regime.

$$h_{flash}A_i''' = 1 \times 10^7 \cdot Max\{1, Min[20, 20(T_f - T_{sat})]\} \tag{2-50}$$

The sensitivity analysis of the flashing model was carried out by modifying the TRACE flashing model as shown in Table 2-4.

Table 2-4. Modifications of TRACE flashing model.

Flashing model	Correlations
TRACE	$h_{flash}A_i''' = 1 \times 10^7 Max\{1, Min[20, 20(T_f - T_{sat})]\}$
Fix 1 (20)	$h_{flash}A_i''' = 1 \times 10^7 \cdot Max\{1, \mathbf{20}(T_f - T_{sat})\}$
Fix 2 (200)	$h_{flash}A_i''' = 1 \times 10^7 \cdot Max\{1, \mathbf{200}(T_f - T_{sat})\}$
Fix 2 (400)	$h_{flash}A_i''' = 1 \times 10^7 \cdot Max\{1, \mathbf{400}(T_f - T_{sat})\}$
Fix 4 (800)	$h_{flash}A_i''' = 1 \times 10^7 \cdot Max\{1, \mathbf{800}(T_f - T_{sat})\}$

The nozzle analyzed in the Sandia report (Ross et al., 2015) was simulated using the different flashing models. The nozzle inlet condition was two-phase flow with the vapor volume fraction of 0.7 at 7MPa. Figure 2-5 shows the profiles of liquid and vapor temperatures for the different flashing models. It can be observed that the current TRACE flashing model leads to highly unphysical superheated liquid temperatures because there is not sufficient flashing heat transfer to suppress the superheated liquid near the saturation condition. Therefore, it is necessary to choose an appropriate flashing model to have a reasonable prediction of the liquid temperature.

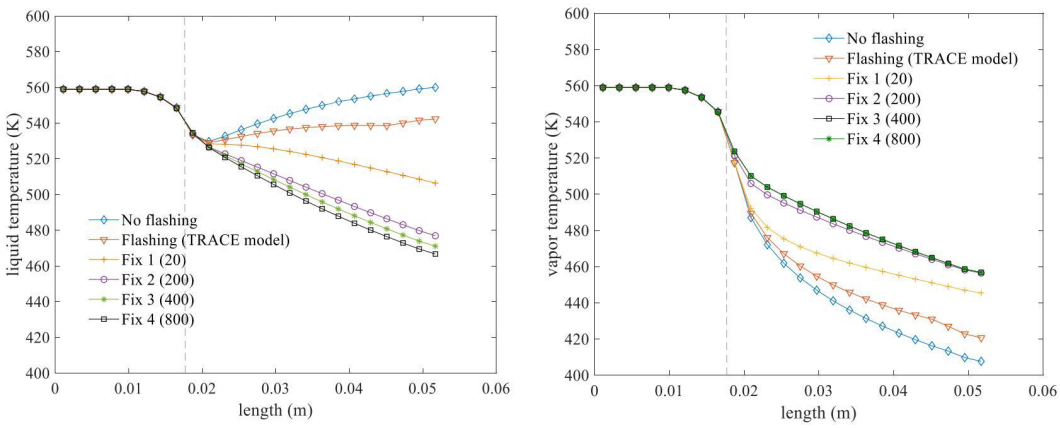

Figure 2-5. Liquid temperature and vapor temperature profiles.

2.3 NUMERICAL METHOD

It is a challenge to solve the thermal-hydraulic behavior of the fluids including the critical flow and nucleation condensation processes. In our implementation, the governing equations are

discretized on the staggered mesh using the second-order Lax-Wendroff scheme. The SIMPLE algorithm is employed to solve the two-phase four-fluid flow model.

2.3.1 DISCRETIZATION OF CONSERVATION EQUATIONS

The nozzle flow governing system of equations is discretized on a staggered-grid, in which the scalar variables (volume fractions, pressure, temperature and densities) are located at the node center, while the velocities are located at the node edge, as shown in Fig. 2-6.

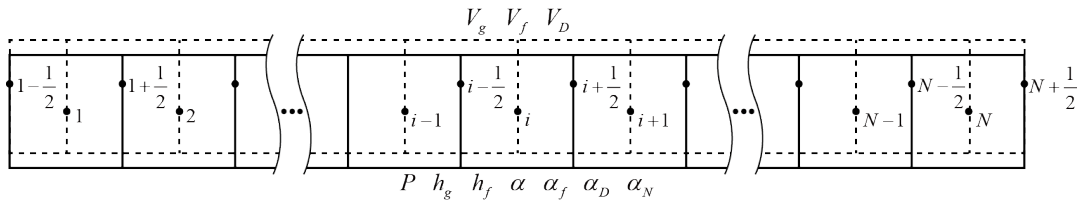

Figure 2-6. Schematic of staggered grid.

The second-order Lax-Wendroff scheme (Lax and Wendroff, 1960; Wang et al., 2013, 2015) with the Van Albada flux limiter is adopted to discretize the mass and energy equations in this report. The mass and energy conservation equations are discretized as.

$$\frac{(f_k\bar{A})_j^{n+1} - (f_k\bar{A})_j^n}{\Delta t} + \frac{\left(\langle f_k\rangle^n A^n {V_k}^{n+1}\right)_{j+\frac{1}{2}} - \left(\langle f_k\rangle^n A^n {V_k}^{n+1}\right)_{j-\frac{1}{2}}}{\Delta x_j} = {R_k}_j^{n+1} \qquad (2\text{-}51)$$

where $\bar{A}$ is the average area in the control volume. $k = g, f, D$. $f_k = \alpha_k \rho_k \psi_k$. $\psi_k = 1$ for the mass equation and $\psi_k = h_k$ for the energy equation. Δt and Δx_j are the time step size and mesh cell size, respectively. ${R_k}_j^{n+1}$ represents the source terms. The Lax-Wendroff scheme (Moore et al., 1973) with the Van Albada flux limiter for the convection term is given by the following equations:

$$\langle f_k\rangle_{j+\frac{1}{2}}^n = \begin{cases} {f_k}_j^n + \phi\left(r_{j+\frac{1}{2}}^n\right)\left(1 - \nu_{j+\frac{1}{2}}\right)\dfrac{{f_k}_{j+1}^n - {f_k}_j^n}{2}, & if\ {V_k}_{j+\frac{1}{2}}^{n+1} \geq 0 \\ {f_k}_j^n - \phi\left(r_{j+\frac{1}{2}}^n\right)\left(1 - \nu_{j+\frac{1}{2}}\right)\dfrac{{f_k}_{j+1}^n - {f_k}_j^n}{2}, & if {V_k}_{j+\frac{1}{2}}^{n+1} < 0 \end{cases}, \quad k = g, f, D \qquad (2\text{-}52)$$

where

$$r_{j+\frac{1}{2}}^n = \begin{cases} \dfrac{{f_k}_j^n - {f_k}_{j-1}^n}{{f_k}_{j+1}^n - {f_k}_j^n}, & if\ {V_k}_{j+\frac{1}{2}}^{n+1} \geq 0 \\ \dfrac{{f_k}_{j+2}^n - {f_k}_{j+1}^n}{{f_k}_{j+1}^n - {f_k}_j^n}, & if {V_k}_{j+\frac{1}{2}}^{n+1} < 0 \end{cases}, \quad k = g, f, D \qquad (2\text{-}53)$$

$$\nu_{j+\frac{1}{2}} = \frac{V_{k_{j+\frac{1}{2}}}^{n+1}\Delta t}{\Delta x_{j+\frac{1}{2}}} = \frac{V_{k_{j+\frac{1}{2}}}^{n+1}\Delta t}{(\Delta x_j + \Delta x_{j+1})/2} \tag{2-54}$$

$$\phi\left(r_{j+\frac{1}{2}}^{n}\right) = \frac{\left(r_{j+\frac{1}{2}}^{n}\right)^2 + r_{j+\frac{1}{2}}^{n}}{\left(r_{j+\frac{1}{2}}^{n}\right)^2 + 1} \tag{2-55}$$

For the momentum equations, the nonconservative forms are firstly obtained by combining continuity equations and conservation momentum equations.

$$(\alpha + \alpha_N)\rho_m\left(\frac{\partial V_g}{\partial t} + V_g\frac{\partial V_g}{\partial x}\right) + \Gamma V_g = -(\alpha + \alpha_N)\frac{\partial P}{\partial x} - F_{wg} - F_i - F_{iD} + \Gamma V_i \tag{2-56}$$

$$(1 - \alpha - \alpha_D - \alpha_N)\rho_f\left(\frac{\partial V_f}{\partial t} + V_f\frac{\partial V_f}{\partial x}\right) - (1-\eta)\Gamma V_f$$

$$= -(1 - \alpha - \alpha_D - \alpha_N)\frac{\partial P}{\partial x} - F_{wf} + F_i - (1-\eta)\Gamma V_i - SV_f \tag{2-57}$$

$$\alpha_D\rho_f\left(\frac{\partial V_D}{\partial t} + V_D\frac{\partial V_D}{\partial x}\right) - \Gamma V_D = -\alpha_D\frac{\partial P}{\partial x} + F_{iD} - \eta\Gamma V_i + SV_f \tag{2-58}$$

The velocity terms of the mass equations, the pressure terms and interphase exchanges of the momentum equations and energy equations, the interfacial drag terms and phase change terms are evaluated at the new time level $n+1$. Then the momentum equations at $j+1/2$ can be discretized as

$$(\alpha_k\rho_k A)_{j+\frac{1}{2}}^{n}\frac{V_{k_{j+\frac{1}{2}}}^{n+1} - V_{k_{j+\frac{1}{2}}}^{n}}{\Delta t} + (\alpha_k\rho_k V_k A)_{j+\frac{1}{2}}^{n}\frac{\langle V_{k_{j+1}}^{n} - V_{k_j}^{n}\rangle}{(\Delta x_j + \Delta x_{j+1})/2} \pm A\Gamma_{j+\frac{1}{2}}^{n+1}V_{k_{j+\frac{1}{2}}}^{n+1}$$

$$= -\alpha_{k_{j+\frac{1}{2}}}^{n}A\frac{P_{j+1}^{n+1} - P_j^{n+1}}{\Delta x_{j+\frac{1}{2}}} - A[F_{wk}]_{j+\frac{1}{2}}^{n+1} \mp A[F_i]_{j+\frac{1}{2}}^{n+1} \pm A\Gamma_{j+\frac{1}{2}}^{n+1}V_{i_{j+\frac{1}{2}}}^{n+1} \tag{2-59}$$

Finally, the discretization of the nonconservative momentum equations can be written as

$$\boldsymbol{MV} = \boldsymbol{NP} + \boldsymbol{B} \tag{2-60}$$

The variable vectors V and P are defined as $\left[V_{g,j+\frac{1}{2}}^{n+1}, V_{f,j+\frac{1}{2}}^{n+1}, V_{D,j+\frac{1}{2}}^{n+1}\right]^T$ and $\left[P_{j+1}^{n+1}, P_j^{n+1}\right]^T$, respectively. The matrix N is given by

$$\boldsymbol{N} = \begin{bmatrix} -\dfrac{\left(\alpha^n_{j+\frac{1}{2}} + \alpha_N{}^n_{j+\frac{1}{2}}\right)}{\Delta x} & \dfrac{\left(\alpha^n_{j+\frac{1}{2}} + \alpha_N{}^n_{j+\frac{1}{2}}\right)}{\Delta x} \\ -\dfrac{(1-\alpha-\alpha_D-\alpha_N)^n_{j+\frac{1}{2}}}{\Delta x} & \dfrac{(1-\alpha-\alpha_D-\alpha_N)^n_{j+\frac{1}{2}}}{\Delta x} \\ -\dfrac{\alpha_D{}^n_{j+\frac{1}{2}}}{\Delta x} & \dfrac{\alpha_D{}^n_{j+\frac{1}{2}}}{\Delta x} \end{bmatrix} \tag{2-61}$$

And matrix M and source term vector B are summarized in Table 2-5.

Table 2-5. The velocity coefficient matrix and source term vector.

Coefficient	Equations
M(1,1)	$\dfrac{((\alpha+\alpha_N)\rho_m)^{n+1}_{j+\frac{1}{2}}}{\Delta t} + 2\left[C_i\lvert V_g - V_f\rvert\right]^n_{j+\frac{1}{2}} + 2\left[C_{wg}\lvert V_g\rvert\right]^n_{j+\frac{1}{2}} + 2\left[C_{iD}\lvert V_g - V_D\rvert\right]^n_{j+\frac{1}{2}} + [max(\Gamma,0)]^{n+1}_{j+\frac{1}{2}}$
M(1,2)	$-2\left[C_i\lvert V_g - V_f\rvert\right]^n_{j+\frac{1}{2}} - (1-\eta)[max(\Gamma,0)]^{n+1}_{j+\frac{1}{2}}$
M(1,3)	$-2\left[C_{iD}\lvert V_g - V_D\rvert\right]^n_{j+\frac{1}{2}} - \eta[max(\Gamma,0)]^{n+1}_{j+\frac{1}{2}}$
M(2,1)	$-2\left[C_i\lvert V_g - V_f\rvert\right]^n_{j+\frac{1}{2}} + (1-\eta)[min(\Gamma,0)]^{n+1}_{j+\frac{1}{2}}$
M(2,2)	$\dfrac{\left[(1-\alpha-\alpha_D-\alpha_N)\rho_f\right]^{n+1}_{j+1/2}}{\Delta t} + 2\left[C_i\lvert V_g - V_f\rvert\right]^n_{j+\frac{1}{2}} + 2\left[C_{wf}\lvert V_f\rvert\right]^n_{j+\frac{1}{2}} - (1-\eta)[min(\Gamma,0)]^{n+1}_{j+\frac{1}{2}}$
M(2,3)	0
M(3,1)	$-2\left[C_{iD}\lvert V_g - V_D\rvert\right]^n_{j+\frac{1}{2}} + \eta[min(\Gamma,0)]^{n+1}_{j+\frac{1}{2}}$
M(3,2)	$-(S_E - S_D)$
M(3,3)	$\dfrac{\left[(\alpha_D)\rho_f\right]^{n+1}_{j+1/2}}{\Delta t} + 2\left[C_{iD}\lvert V_g - V_D\rvert\right]^n_{j+\frac{1}{2}} - \eta[min(\Gamma,0)]^{n+1}_{j+\frac{1}{2}} + (S_E - S_D)$
B(1)	$-\left((\alpha+\alpha_N)\rho_m V_g\right)^n_{j+\frac{1}{2}} \dfrac{\langle (V_g)^n_{j+\frac{1}{2}} - (V_g)^n_{j-\frac{1}{2}}\rangle}{\Delta x} + \dfrac{\left((\alpha+\alpha_N)\rho_m V_g\right)^n_{j+\frac{1}{2}}}{\Delta t} + \left[C_i\lvert V_g - V_f\rvert\right]^n_{j+\frac{1}{2}}\left(V^n_{g,j+\frac{1}{2}} - V^n_{f,j+\frac{1}{2}}\right) + (C_{iD})^n_{j+\frac{1}{2}}\left\lvert V_{g}{}^n_{j+\frac{1}{2}} - V_{D}{}^n_{j+\frac{1}{2}}\right\rvert\left(V_{g}{}^n_{j+\frac{1}{2}} - V_{D}{}^n_{j+\frac{1}{2}}\right) - \left[C_{wg}\lvert V_g\rvert\right]^n_{j+\frac{1}{2}} V^n_{g,j+\frac{1}{2}}$
B(2)	$-\left[(1-\alpha-\alpha_D-\alpha_N)\rho_f V_f\right]^n_{j+\frac{1}{2}} \dfrac{\langle (V_f)^n_{j+\frac{1}{2}} - (V_f)^n_{j-\frac{1}{2}}\rangle}{\Delta x} + \dfrac{\left[(1-\alpha-\alpha_D-\alpha_N)\rho_f V_f\right]^n_{j+\frac{1}{2}}}{\Delta t} + \left[C_i\lvert V_g - V_f\rvert\right]^n_{j+\frac{1}{2}}\left(V^n_{f,j+\frac{1}{2}} - V^n_{g,j+\frac{1}{2}}\right) - \left[C_{wf}\lvert V_f\rvert\right]^n_{j+\frac{1}{2}} V^n_{f,j+\frac{1}{2}}$
B(3)	$-\left[\alpha_D\rho_f V_D\right]^n_{j+1/2} \dfrac{\langle (V_D)^n_{j+1/2} - (V_D)^n_{j-1/2}\rangle}{\Delta x} + \dfrac{\left[\alpha_D\rho_f V_D\right]^n_{j+1/2}}{\Delta t} + \left[C_{iD}\lvert V_g - V_D\rvert\right]^n_{j+\frac{1}{2}}\left(V^n_{D,j+\frac{1}{2}} - V^n_{g,j+\frac{1}{2}}\right)$

The mass conservation equations are discretized in a semi-implicit format as

$$\frac{(\alpha_k\rho_k\bar{A})^{n+1}_j - (\alpha_k\rho_k\bar{A})^n_j}{\Delta t} + \frac{\left(\langle f_k\rangle^n A^n V_k{}^{n+1}\right)_{j+\frac{1}{2}} - \left(\langle f_k\rangle^n A^n V_k{}^{n+1}\right)_{j-\frac{1}{2}}}{\Delta x_j} = \bar{A}_j R_{k_j}{}^{n+1} \tag{2-62}$$

The energy conservation equations are also discretized in a semi-implicit format. It should be noted that the continuous liquid and droplet fluid are considered in a single common energy equation.

The source terms $R_{k_j}{}^{n+1}$ are summarized in Table 2-6.

Table 2-6. Source terms in the mass and energy equations.

Fluid	Mass conservation equation	Energy conservation equation
Vapor	Γ_j^{n+1}	$q_{gi}'''^{n}_{j} + \max(\Gamma_j^n, 0)\, h_{gs}{}_j^{n+1} - \max(\Gamma_j^n, 0)\, h_g{}_j^{n+1}$
Liquid	$-\eta\Gamma_j^{n+1} - S$	$q_{fi}'''^{n}_{j} + \min(\Gamma_j^n, 0)\, h_f{}_j^{n+1} - \min(\Gamma_j^n, 0)\, h_{fs}{}_j^{n+1}$
Droplets	$-(1-\eta)\Gamma_j^{n+1} + S$	—

The scalar equations of the condensed droplet phase mass-fraction and the number density of the droplets can be discretized as

$$\frac{(\rho_m \bar{A}\beta)_j^{n+1} - (\rho_m \bar{A}\beta)_j^n}{\partial t} + \frac{\left(\langle f_\beta \rangle^n A V_g{}^{n+1}\right)_{j+\frac{1}{2}} - \left(\langle f_\beta \rangle^n A V_g{}^{n+1}\right)_{j-\frac{1}{2}}}{\Delta x_j} = \bar{A}_j \Gamma_N{}_j^n \tag{2-63}$$

$$\frac{(\rho_m \bar{A}\eta)_j^{n+1} - (\rho_m \bar{A}\eta)_j^n}{\partial t} + \frac{\left(\langle f_\eta \rangle^n A V_g{}^{n+1}\right)_{j+\frac{1}{2}} - \left(\langle f_\eta \rangle^n A V_g{}^{n+1}\right)_{j-\frac{1}{2}}}{\Delta x_j} = \bar{A}_j \rho_m I_j^n \tag{2-64}$$

2.3.2 NUMERICAL SOLUTION

The SIMPLE algorithm is employed to solve the compressible two-phase four-fluid flow through a nozzle at all speeds from subsonic to supersonic flow. The pressure, velocity, and density at the new iteration step can be expressed as the value at the previous iterative step plus an increment.

$$P_j^{n+1,l} = P_j^{n+1,l-1} + \delta P_j^{n+1} \tag{2-65}$$

$$V_{k_{j+\frac{1}{2}}}^{n+1,l} = V_{k_{j+\frac{1}{2}}}^{n+1,l-1} + \delta V_{k_{j+\frac{1}{2}}}^{n+1} \tag{2-66}$$

$$\rho_k{}_j^{n+1,l} = \rho_k{}_j^{n+1,l-1} + \left.\frac{\partial \rho_k}{\partial P}\right|_j \cdot \delta P_j^{n+1} \tag{2-67}$$

Because of strong coupling between the fluids, it requires the simultaneous solution of the vapor (condensed droplets may be included), liquid film and droplet momentum equations at each face. The algebra is simplified by writing the momentum equation in terms of the velocity change in each new time step from its previous estimate. Based on Eq. 2-59, the relationship between $\delta V_{k_{j+\frac{1}{2}}}^{n+1}$ and $\delta P_{j+\frac{1}{2}}^{n+1}$ can be obtained by

$$\begin{pmatrix} \delta V_{g_{j+\frac{1}{2}}}^{n+1} \\ \delta V_{f_{j+\frac{1}{2}}}^{n+1} \\ \delta V_{D_{j+\frac{1}{2}}}^{n+1} \end{pmatrix} = [\boldsymbol{M}^{-1}\boldsymbol{N}]_{j+1/2} \cdot \begin{pmatrix} \delta P_{j+1}^{n+1} \\ \delta P_j^{n+1} \end{pmatrix} \tag{2-68}$$

To calculate the pressure increment δP_j^{n+1}, a mixed mass continuity equation can be obtained by combining the three mass conservation equations of vapor, liquid film and droplets.

The semi-implicit approximation is applied in the discretizing of the conservation equations in the present nozzle model. The physical properties, parameters in the closure relations are evaluated first. Then the SIMPLE algorithm is utilized to solve the continuity and momentum equations. Finally, the other conservation equations are solved and the variables required for the next time step are updated. Table 2-7 shows the procedure of the SIMPLE algorithm in detail.

Table 2-7. SIMPLE algorithm for two-phase four-fluid flow.

For n=0,1,…., do (time steps)

Initialize all the fields using the values at the previous time step

For l=1,2,…, do (iteration procedure between the different fields)

Solve the velocity $V_{k_{j+\frac{1}{2}}}^{n+1,l-1}$ $(k = g, f, D)$ using the pressure$P_j^{n+1,l-1}$, volume fraction $\alpha_{k_{j+\frac{1}{2}}}^{n+1,l-1}(k = g, f, D)$ and density $\rho_{k_j}^{n+1,l-1}(k = g, f, D)$ at the previous iteration step.

Calculate the pressure correction equation based on the mass conservation equation.

Correct the velocity, pressure and density using Eqs. 2-65 to 2-67

Obtain the void fraction $\alpha_k(k = g, f, D)$ by solving Eq. 2-62

Obtain the enthalpy $h_k(k = g, l)$ by solving energy equations and update the density fields

Solve the nucleation condensation equations if it is turned on, and obtain α_N from Eq. 2-69 and Eq. 2-9

Iterate until all the variables satisfy the convergence criteria

end

end

For two-phase critical flow through a nozzle, two-phase subsonic flow is present in the converging region, sonic or choking flow is present in the throat region and supersonic flow is present in the diverging region. The three different regions are coupled together to describe the entire model and they have different mathematical features. Before the critical flow occurs, the whole nozzle is simulated with the nozzle inlet boundary and outlet pressure boundary, which is a typical flow simulation of a pipe with variable cross-sectional area. When the critical flow occurs, the nozzle calculation is divided into the two sub-domains, converging section and diverging section. Each section has its own boundary conditions. The inlet boundary conditions for the diverging section use the critical flow conditions calculated from the converging section. In this study, we assume the choking point is at the throat, which is located right at the cell interface. The time step size is determined by the CFL condition. Since the choking flow determines the transition from subsonic to supersonic conditions, we need to obtain the choking velocities of the fluids. It is discussed in Section 3.1 that the choking model requires the thermal conditions at the upstream cell or cell-edge where the choking flow may occur. The choking logic has to determine which cell edges are choked and which are unchoked. Therefore, the iteration is needed between the subsonic flow for the converging region and choking flow for

the throat region until convergence. Then the obtained critical conditions at the throat are utilized as the boundary conditions for the supersonic flow in the diverging region. Due to the hyperbolicity of the governing equations, the outlet boundary conditions of the nozzle are not necessary for calculating the supersonic flow. The variables at the nozzle outlet can be determined by extrapolation from the interior region. The numerical methodology implemented in the present work is shown in Fig. 2-7.

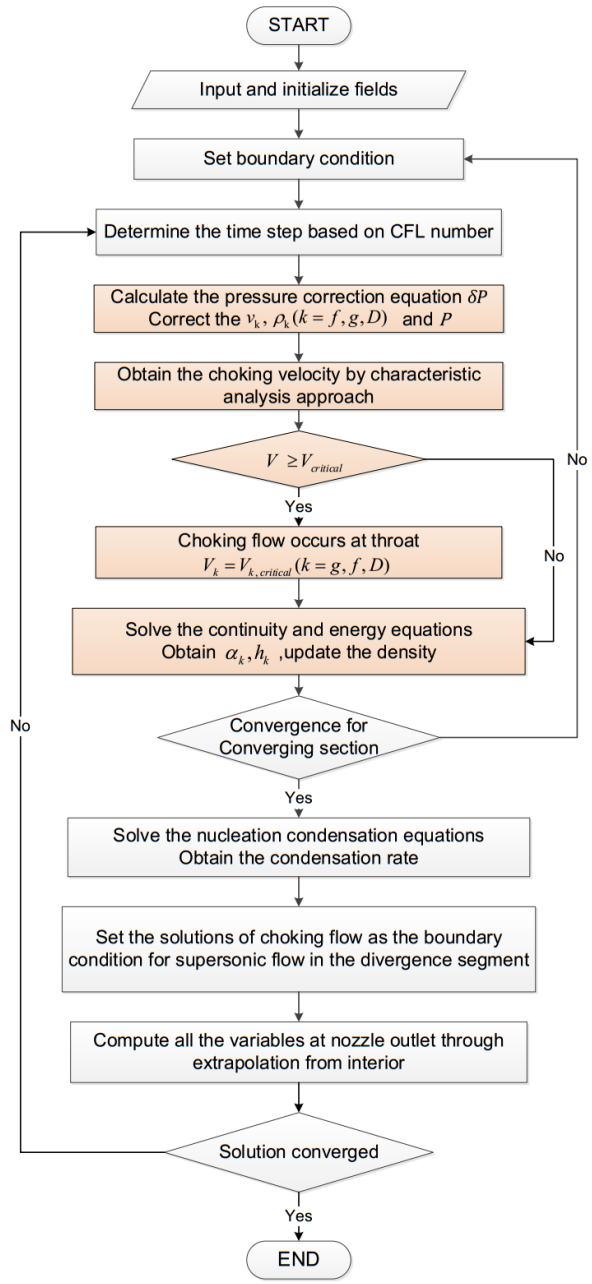

Figure 2-7. Flowchart for the two-phase critical flow with condensation through a nozzle.

2.4 SUMMARY

In this chapter, we have presented our newly developed on the one-dimensional non-equilibrium four-fluid flow model developed for two-phase transonic flow through a convergent-divergent nozzle. The vapor, liquid film and entrained droplet fields are calculated separately, and the condensed droplet field are merged into the vapor fields if condensation occurs. The flow governing equations, critical flow model, nucleation condensation model, flashing model and the numerical techniques were presented and discussed in detail. Compared with the two-fluid scheme, the closure models are modified for high-speed nozzle flow. The mechanistic nozzle model developed in this report has provided a much-needed capability for

modeling and simulation of complex two-phase flow processes and phenomena through a convergent-divergent nozzle, which is largely missing in current thermal-hydraulic system analysis codes and CFD software. The work is of significant importance for the understanding and analysis of dynamic responses of the RCIC system under BDBA conditions, in which Terry turbine nozzle flow plays a vital role.

3. Assessment of the Nozzle Model and Table Generation

The nozzle model consists of the two-phase flow model and special models such as the critical flow model and the nucleation condensation model. For the spontaneous nucleation condensation phenomena in the nozzle, many experiments have been carried out and the data is well documented. In order to demonstrate the predictability of the nozzle model implemented, the experimental data of two supersonic nozzle tests, Moore nozzle (Moore et al., 1973) and Barschdorff nozzle (Barschdorff et al., 1972), are compared with the numerical predictions obtained by the nozzle model. Another nozzle case with higher working pressure, Kneass nozzle, is simulated by both the developed nozzle model and FLUENT under different inlet steam pressures.

3.1 Benchmark with Steam Nozzle Tests

3.1.1 Analysis of Moore nozzle

Moore et al. (1973) tested a series of nozzle designs with various expansion rates. The Type B nozzle in Moore's test was selected for the simulation. The geometry of the Moore nozzle is shown in Fig. 3-1. The length of the convergent segment is 0.2m and the divergent segment is 0.5m. In the test, the inlet pressure is 25kPa and the inlet total temperature is 356.6K. The stagnation boundary conditions in the simulation are the same as those of the experiment. The velocity of the convergent section becomes supersonic.

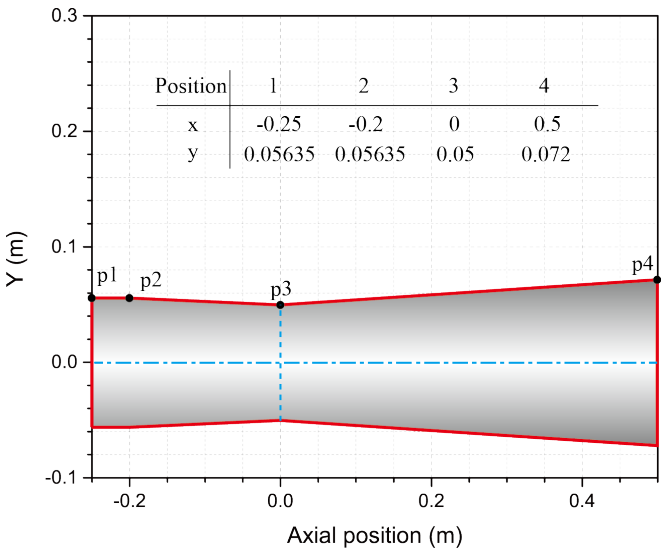

Figure 3-1. Geometry of Moore nozzle Type B.

Figures 3-2 present flow variables of the Moore's nozzle simulation. The static pressure profiles through the nozzle are shown in Fig. 3-2(a). In the process of nucleation condensation,

the latent heat releases and the vapor temperature increases rapidly, as shown in Fig. 3-2(b), which leads to a pressure increase. The numerical temperature results are compared with those of the condensation model implemented by Yang et al. (2017). The condensation shock can be observed in the downstream of throat, at the position of approximately 0.1m. The trigger of the spontaneous nucleation condensation can also be explained by the change of supersaturation ratio S. It is well below one in the nozzle inlet for the superheated vapor inlet conditions. Then S increases in the direction of flow and crosses the saturation line. When the value becomes high enough, the condensation occurs.

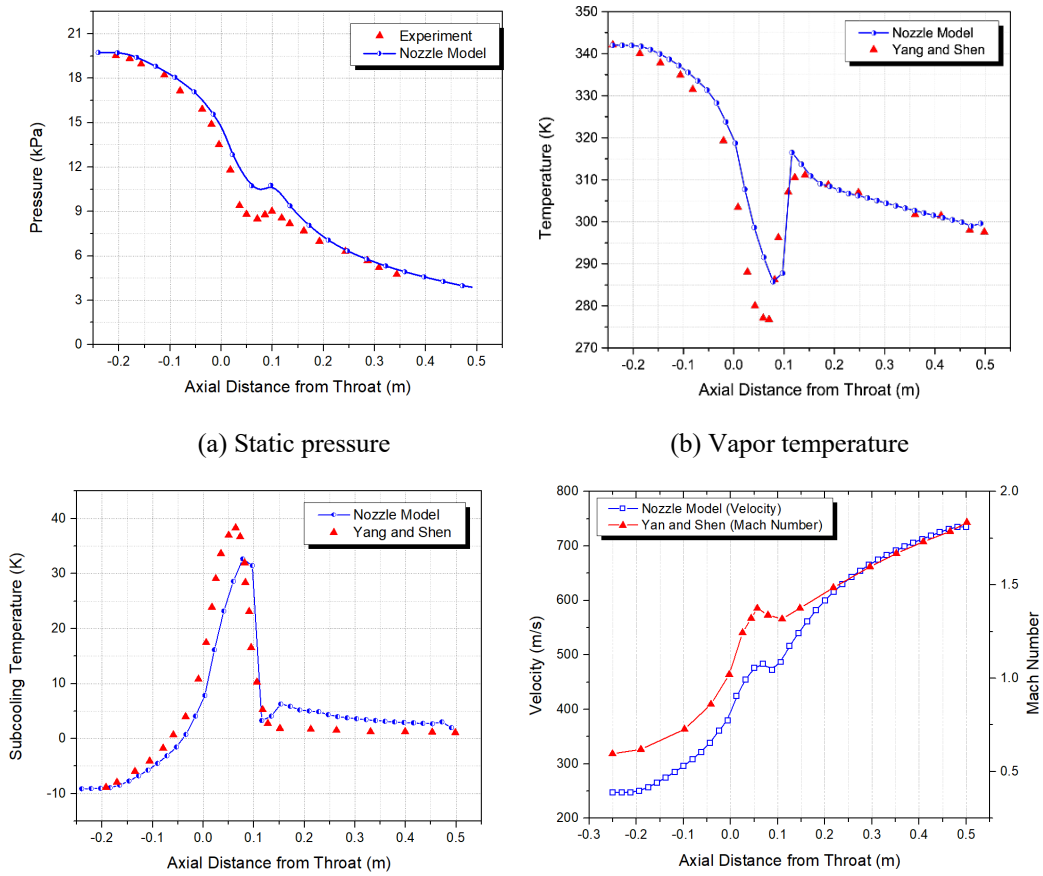

(a) Static pressure

(b) Vapor temperature

(c) Super cooling level

(d) Velocity

Figure 3-2. Distributions of flow variables along the axis of Moore nozzle.

Figures 3-3 depict the nucleation condensation parameters which are of interest in the nozzle transonic flow with spontaneous condensation. Figure 3-3(a) shows the droplet radius change and the radius growth rate, which are sensitive to the supersaturation rate as shown in Fig. 3-3(b). Due to the nucleation condensation, the latent heat released would cause the supersaturation rate to decrease and then the nucleation rate drops, correspondingly. Further subcooling of the vapor also stops due to the condensation process, as shown in Fig. 3-3(c). The nucleation process occurs in a short range, but the steam wetness keeps increasing in the downstream of the trigger point, as shown in Fig. 3-3(d). The reason is the growth of the condensation droplets after the nucleation process. The droplet mass fraction increases due to the increasing droplet size. In other words, the droplet number rises as a result of the nucleation

process and the wetness increases due to the droplet growth. The outlet wetness in this case reaches to about 5.3%.

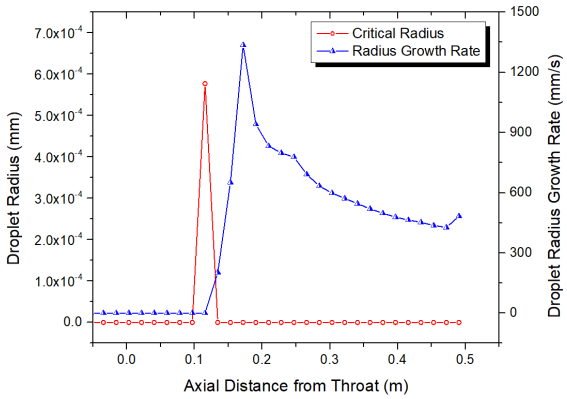

(a) Critical radius and average radius of droplets

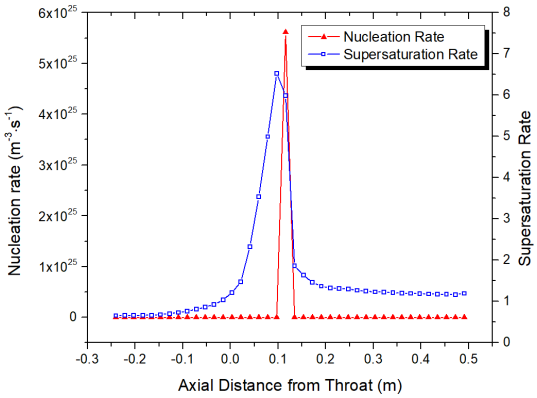

(b) Nucleation rate and number of droplets

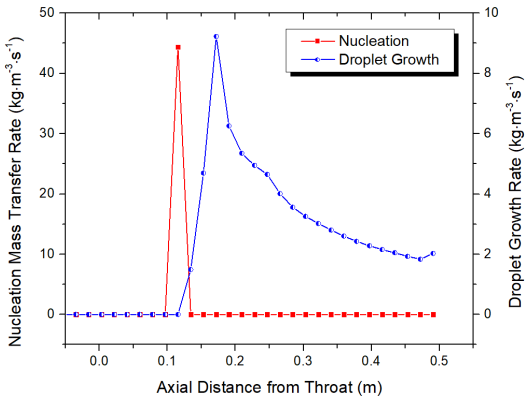

(c) Nucleation mass transfer rate and droplet growth rate

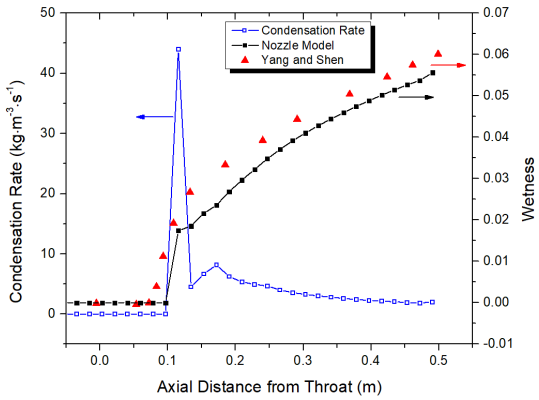

(d) Condensation rate and wetness

Figure 3-3. Distributions of condensation variables along the axis of Moore nozzle.

3.1.2 ANALYSIS OF BARSCHDORFF NOZZLE

The Barschdorff experiment selected an arc convergent-divergent nozzle. The geometry of this nozzle is shown in Fig. 3-4. It has much smaller dimensions than the Moore nozzle. The convergent segment and divergent segment have the same length and symmetric shape. The total length of the nozzle part is 0.24m. The critical throat diameter is 0.06m and the nozzle inlet diameter is 0.085m. The case with a total inlet pressure of 78.39kPa was selected for the simulation. The outlet of the nozzle is supersonic for the test case.

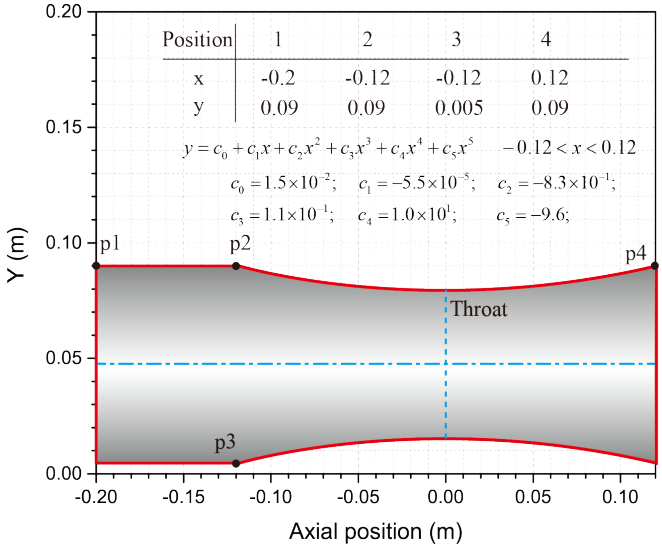

Figure 3-4. Geometry of Barschdorff nozzle.

Figures 3-5 show the numerical results of the nozzle model and comparison with the test data and numerical predictions from the reference (Pandey, 2014). Compared with the Moore nozzle, the Barschdorff nozzle has higher pressure and temperature. Therefore, the onset of nucleation condensation is located further downstream of the Barschdorff nozzle, at approximately 0.05m. From Fig. 3-5(a) and Fig. 3-5(b), it can be observed that the present numerical model can predict thermal-hydraulic characteristics of the transonic nozzle with reasonable accuracy. The condensation shock can also be captured in this case. Despite the slowing down effect of condensation, the outlet of the nozzle flow is still supersonic. As discussed earlier, the latent heat released in the condensation process is also subcritical.

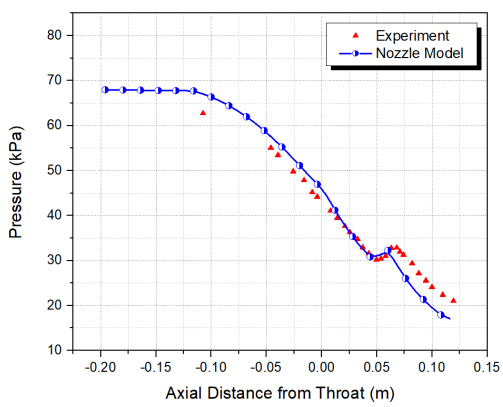

(a) Static pressure

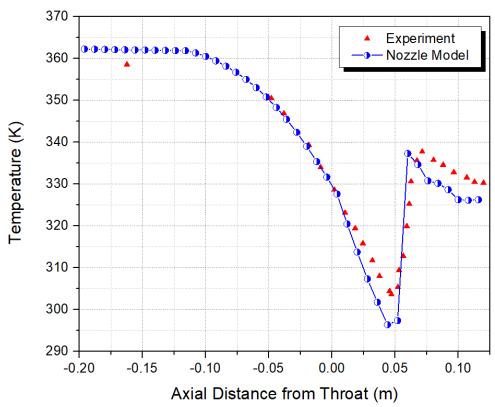

(b) Vapor temperature

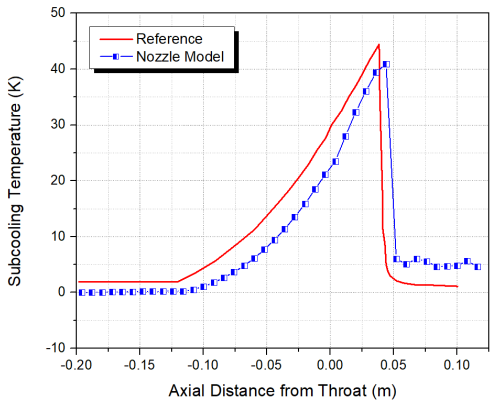

(c) Subcooling level

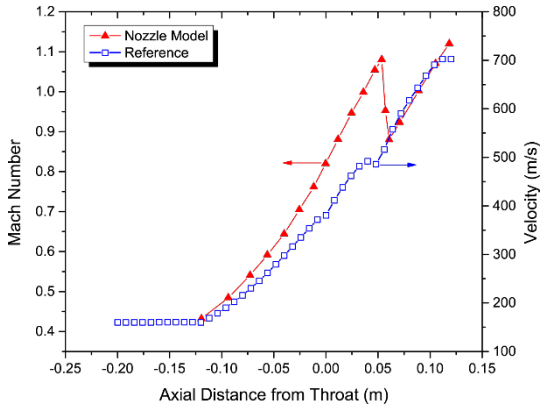

(d) Velocity

Figure 3-5. Distributions of main flow parameters along the axis of Barschdorff nozzle.

The numerical results of condensation variables of the Barschdorff nozzle are shown in Fig. 3-6. Due to the higher working pressure and steam temperature of the Barschdorff nozzle, the peak value of the droplet critical radius is lower, and the nucleation rate is much higher than that of the Moore nozzle. The droplet also has a larger radius growth rate. Therefore, the mass transfer rates due to both the droplet generation and droplet growth are larger than those of the Moore nozzle. The steam wetness cannot be directly benchmarked because the experimental data is unavailable. The numerical prediction from Dykas's work (Wróblewski et al., 2009) is used for assessment. Dykas used a single-phase model to calculate the steam flow in the same case. Figure 3-6(d) illustrates the wetness profile from the present simulation and Dykas's results. It indicates that our condensation model can predict the wetness in good agreement with the results of Dykas.

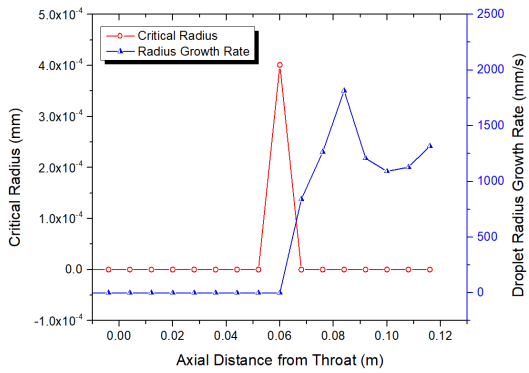

(a) Critical radius and average radius of droplets

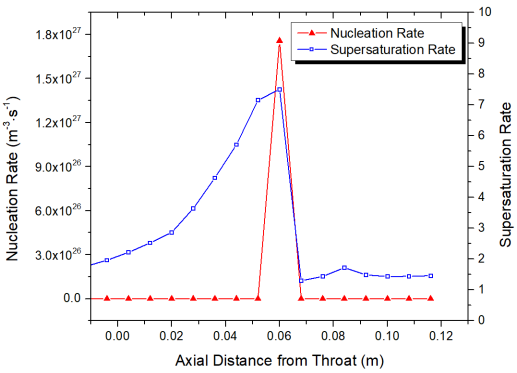

(b) Nucleation rate and number of droplets

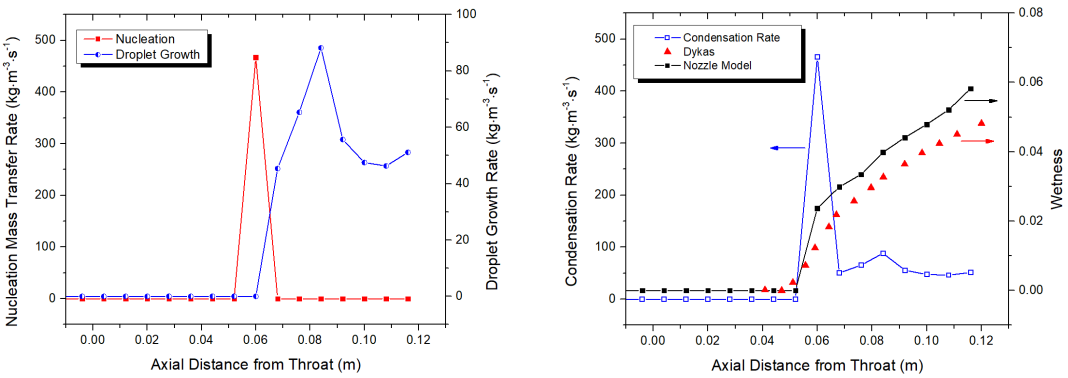

(c) Nucleation mass transfer rate and droplet growth rate (d) Condensation rate and wetness

Figure 3-6. Distributions of condensation variable along the axis of Barschdorff nozzle.

3.2 ANALYSIS OF KNEASS NOZZLE

Both the Moore nozzle and the Barschdorff nozzle have much different geometry and dimensions compared to the nozzles of the Terry turbine. A nozzle that is roughly comparable to the nozzles of the Terry turbine is selected from the nozzle experiment of Kneass (French, 1907). The same nozzle was also adopted for benchmark analysis in the Sandia RCIC analysis report (Ross et al., 2015). The inlet pressures of the Kneass nozzle tests are much lower than those of the Terry turbine in the RCIC system under accident conditions. However, only the pressure data is available. As the modern steam nozzle is usually designed to work with superheated steam, the contemporary test data for the saturated steam flow through the convergent-divergent nozzle are not readily available. Due to lack of relevant experimental data, a simple benchmark study of the static pressure was carried out. The additional CFD simulation by FLUENT was performed to compare with the predictions by the present nozzle code.

Figure 3-7 shows the geometry of the selected nozzle. It has the length of 4.4 cm and the throat diameter of 0.8 cm. The throat is located near 20% of the nozzle length. The divergent segment is 3.52cm long with a 1 in 6 taper, i.e., the nozzle expands 1 unit radially for every 6 units axial length. Unfortunately, the inlet section and convergent section of this nozzle is not well defined in the reference. Therefore the geometry presented in the Sandia report was selected for this study. The nozzle inlet section has the diameter of 2.54cm and gradually contours to the throat, as shown in Fig. 3-7.

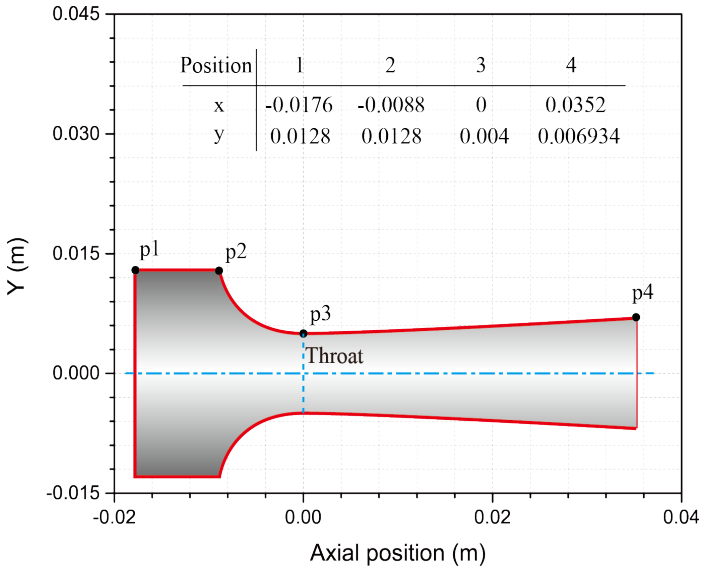

Figure 3-7. Geometry of Kneass nozzle.

The mesh of the nozzle used for the ANSYS FLUENT model is shown in Fig. 3-8. A long inlet plenum and the nozzle discharge region were also modeled. Only half of the nozzle was modeled in the CFD calculation for symmetry. The compressible 2-D turbulent flow solver was adopted in the simulation. The k-□ turbulence model with the default parameters was applied. It should be noted that there are alternative two-phase model options in FLUENT, such as mixture and Eulerian models. To simplify the calculation, the wet-steam model which can provide the most stable and fast-running solutions to the nozzle problem was utilized. The standard wall function models were used for the simple benchmark study. The walls were treated as adiabatic. The inlet surface is specified to be dry saturated steam at various pressures in accordance with the inlet pressures of the experiment. The outlet surface is assumed to be at atmospheric pressure.

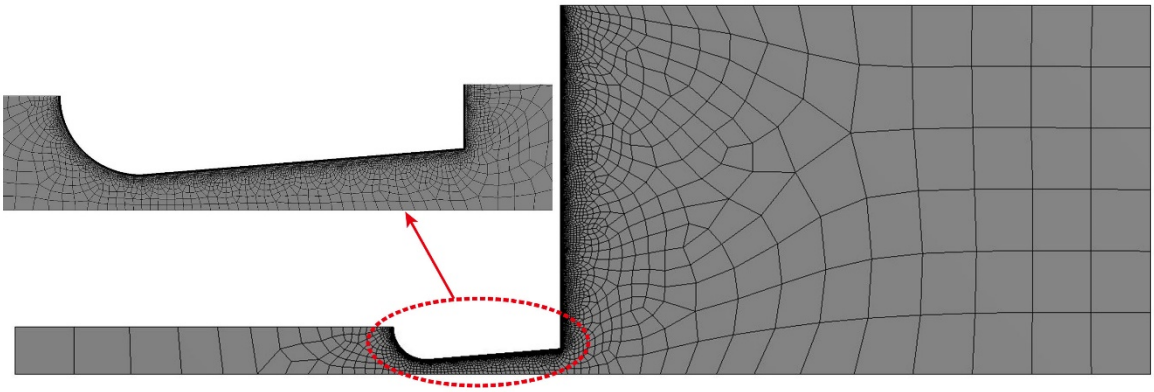

Figure 3-8. Computational mesh for Kneass nozzle.

3.2.1 VALIDATION WITH THE TEST DATA

Figures 3-9 depict the static pressure profiles along the length of the nozzle at various inlet pressures. The throat is near 0.2 normalized length. The numerical results of the nozzle model

were compared with the test data, FLUENT CFD results, and Solidworks results from the reference (Ross et al., 2015). It is noted that both the results of our nozzle model and the CFD-calculated pressures are in excellent agreement with the test data near the throat and in the downstream of the throat. However, it shows that the numerically calculated pressure profiles before the throat are considerably higher than the test data. This is probably due to the geometry of this section which is not clearly defined in the reference and estimated dimensions are adopted in the modeling. In addition, the measurement uncertainty might lead to a considerable error. For the lower pressure cases, specifically 30psi, both the CFD results and the test data show a shock developing in the diverging section of the nozzle, which leads to an obvious pressure increase in the shock region.

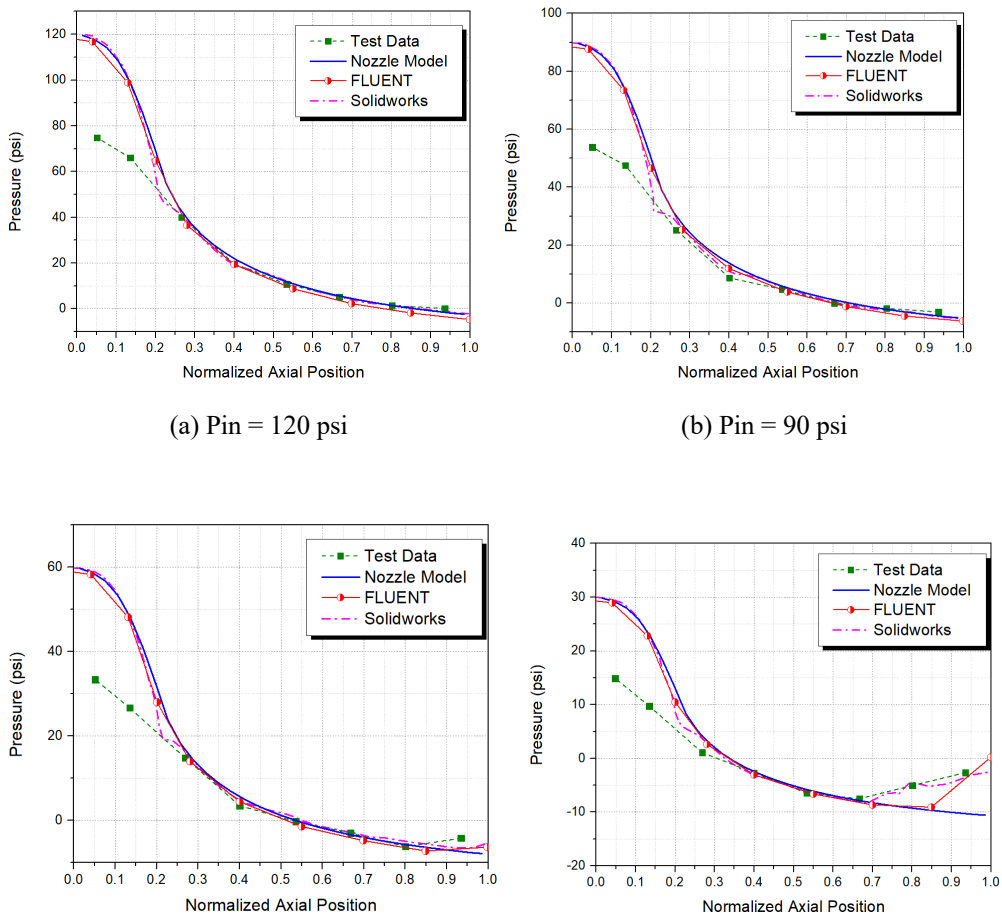

(a) Pin = 120 psi

(b) Pin = 90 psi

(c) Pin = 60 psi

(d) Pin = 30 psi

Figure 3-9. Comparison of static pressure distributions.

Table 3-1 shows the exit velocity comparison between the numerical solutions and test data. The velocity results of the nozzle model have good agreement with the CFD results of SolidWorks and FLUENT. But these numerical values are generally within 5-10% of the measurement values. The reason is probably due to the high measurement uncertainty in the experimental data, particularly with respect to the available technology when these tests were performed. In addition, it should be mentioned that the 30psi case was not included in Table 3-1. In the 30psi case, the data exhibits a strong shock after 70% of the nozzle length, which is well predicted by the SolidWorks calculations from the reference (Ross et al., 2015). In the

present model, the supersonic compression shock is not modeled and therefore the shock phenomenon cannot be simulated.

Table 3-1. Comparison of velocities near nozzle exit

Inlet Pressure (Psig)	Nozzle exit velocity (m/s)			
	Test data	SolidWorks	FLUENT	Numerical values
120	871	926	916	913
90	874	917	906	905
60	808	896	894	893

3.2.2 COMPARISON WITH FLUENT

In this section, the cases with the inlet pressures of 60 psi, 90 psi, 120 psi and 150 psi were simulated by both the developed nozzle model and FLUENT, respectively. Both the nozzle model and FLUENT predicted considerable condensation as the steam expands and exits the nozzle. Unfortunately, there is no direct measured data for the wetness (i.e., liquid mass fraction) profile along the nozzle flow. Therefore, the comparison between the nozzle model and FLUENT results was performed as a simple benchmark study of the nucleation condensation in this case.

Figures 3-10 through 3-13 depict the pressure, velocity, temperature and wetness contours of the Kneass nozzle at different inlet pressures, respectively. It can be observed that the two-dimensional effects on the pressure and velocity fields are not significant in these cases, i.e., the isolines of the flow fields are much smoother than the temperature fields in Fig. 3-12. The pressure contours in Fig. 3-10 show that the shock development in the 60psi case can also be captured near the outlet of the nozzle, in which the steam expands too quickly through the nozzle and the pressure drops below the outlet pressure. It is evident in the 60psi case that an increase in the pressure caused by the supersonic compression shock is observed in the transition region between the diverging section and discharge region. A slight shock wave can also be captured in the nozzle discharge region in the 90psi case but the nozzle part is not affected. For higher pressure cases, the pressure transits much smoother from the diverging section to discharge region. A condensation shock can be observed in temperature contours near the nozzle throat and it is more obvious in the lower pressure cases than the higher pressure cases, as shown in Fig. 3-12. There is an obvious temperature increase when the steam flow from the diverging section to the discharge region which is also evident in the lower pressure cases.

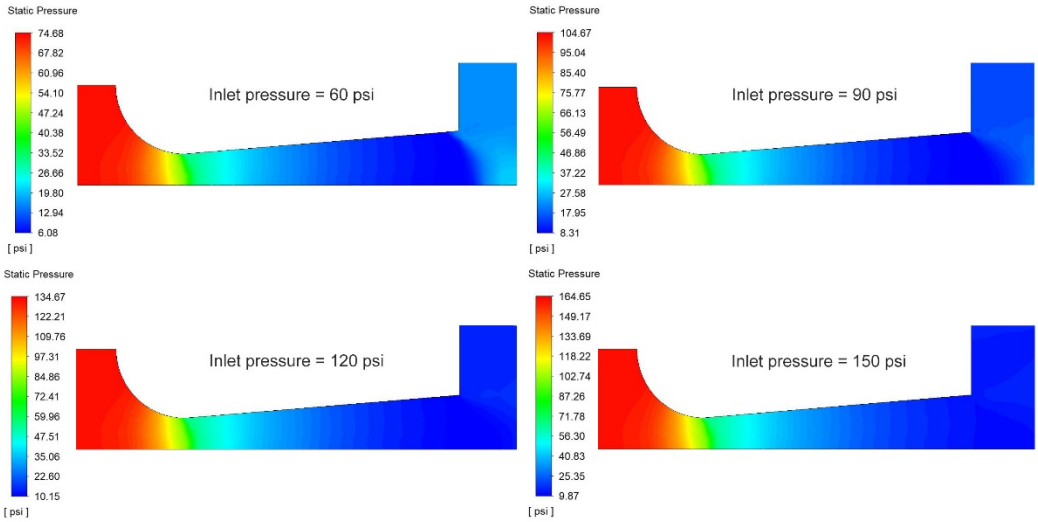

Figure 3-10. Pressure contours at cross-section plane of the calculated nozzle.

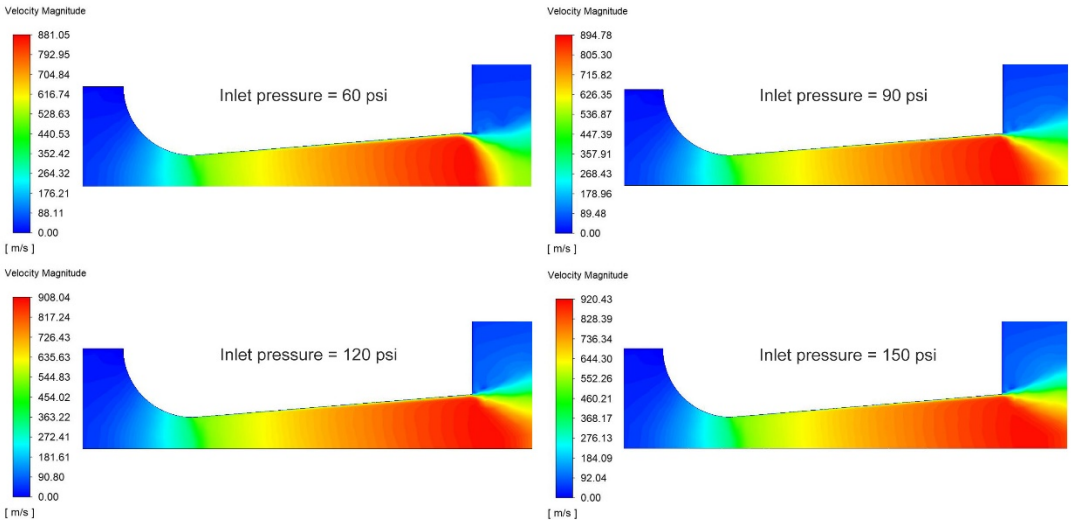

Figure 3-11. Velocity contours at cross-section plane of the calculated nozzle.

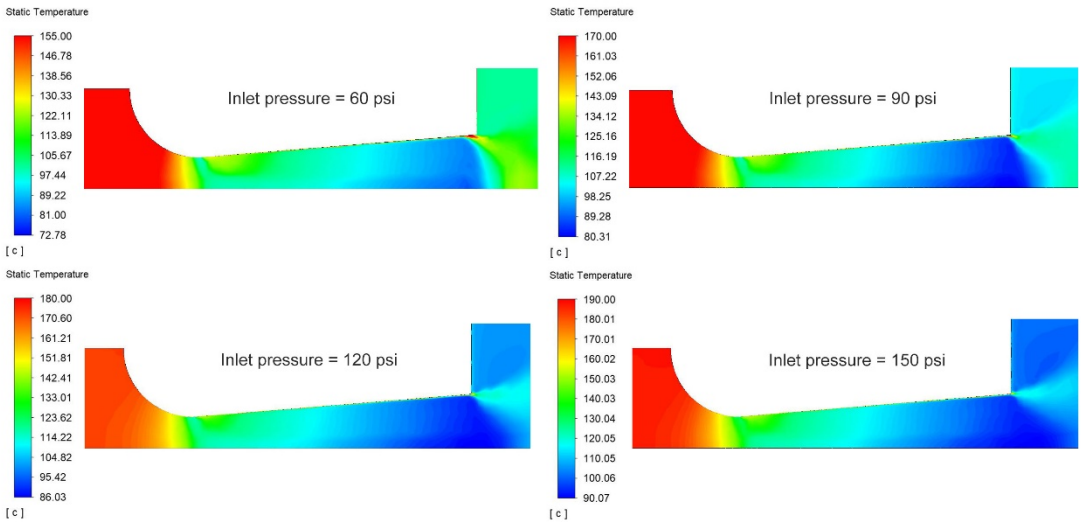

Figure 3-12. Temperature contours at cross-section plane of the calculated nozzle.

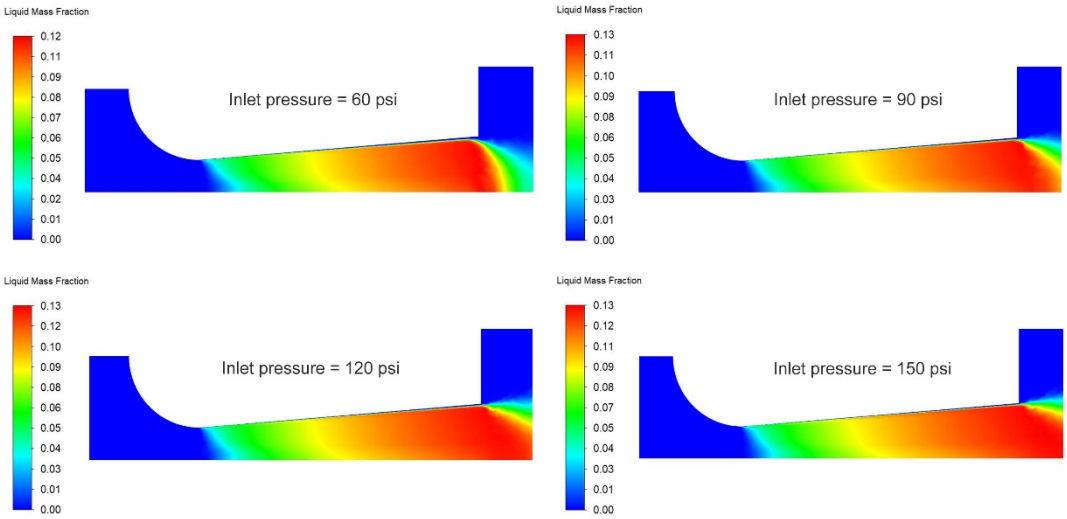

Figure 3-13. Wetness contours at cross-section plane of the calculated nozzle.

The comparison between the 1D nozzle model and FLUENT results were firstly carried out for the 120psi case, with the inlet pressure of 92.87kPa and the inlet temperature of 449.85K at saturation. Figures 3-14 show the main variable distributions in the flow direction. The variable values from FLUENT are the cross-section averaged values. The temperature jumps during condensation were captured with good accuracy in this case. In the downstream section of the nucleation condensation, the temperature result predicted by the nozzle model is slightly lower than the FLUENT prediction. The vapor temperature at the outlet is 360K in the 1D nozzle model solution and 366K in the FLUENT result. It can be observed that the vapor velocity from the nozzle model calculation also has good agreement with that from the FLUENT calculation. The condensation shock has a much smaller effect on the pressure and velocity, as demonstrated by Fig. 3-14(a) and 3-14(c). The 1D nozzle model predictions of the steam wetness also compare reasonably well with the FLUENT results in Fig. 3-14(d). Together with the pressure verification of 120psi case in the former section, the developed nozzle model has demonstrated its reasonable accuracy and capability for high pressure steam flow cases.

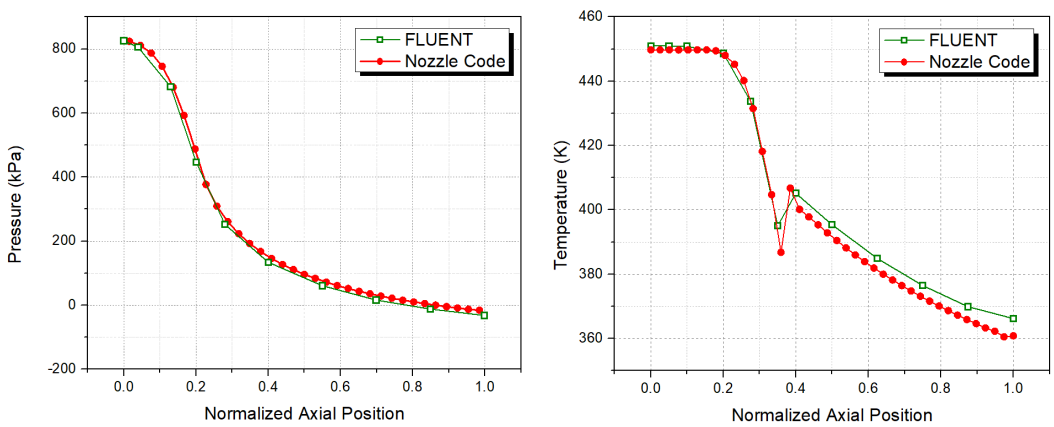

(a) Static pressure (b) Vapor temperature

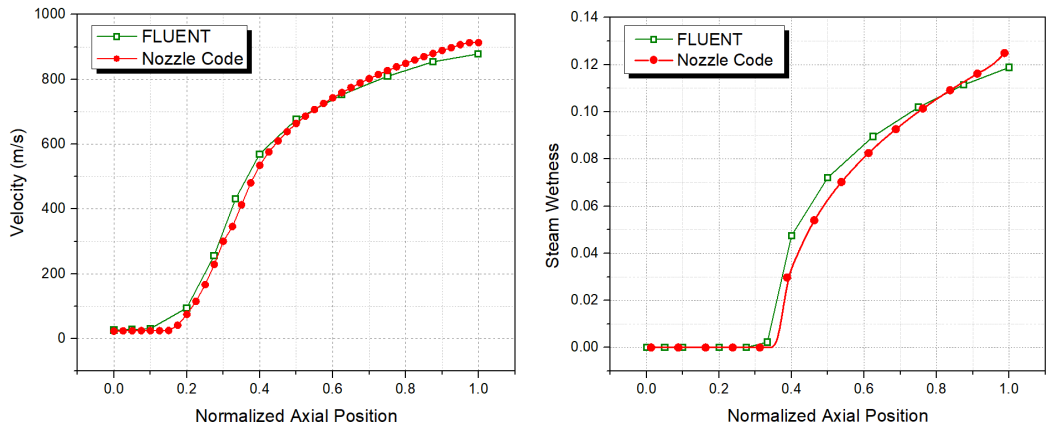

(c) Vapor velocity (d) Steam wetness

Figure 3-14. Comparison with FLUENT results (p_in=120psi).

Figures 3-15 present the comparisons of flow parameters under different inlet pressures (60psi, 90psi, 120psi, and 150psi). The static pressure plots in Fig. 3-15(a) indicates that the pressure difference is larger in the converging section than that of the diverging section. The condensation shock in the nucleation condensation zone is more obvious in the temperature than that in the pressure and velocity curves. Compared with the pressure and temperature results, the subcooling temperature and liquid mass fraction are less sensitive to the inlet pressure value. In these cases, the critical flow occurs and the flow in the whole diverging section is supersonic. The inlet pressure difference is not large enough to give appreciable change in the vapor velocity. It is interesting to note that these cases almost have the same subcooling temperature profiles but significantly different temperature profiles. It is probably due to the rapid expansion near the throat and the corresponding depressurization. Therefore, the nucleation condensation is almost triggered at the same position.

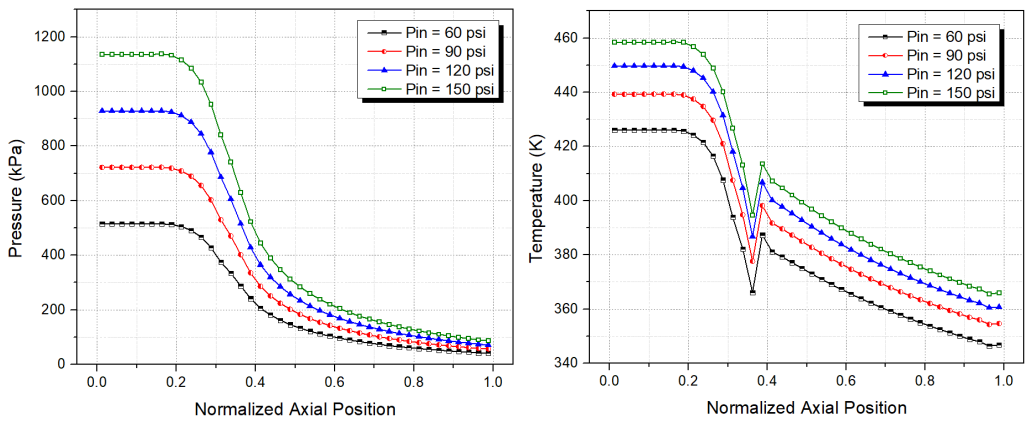

(a) Static pressure (b) Vapor temperature

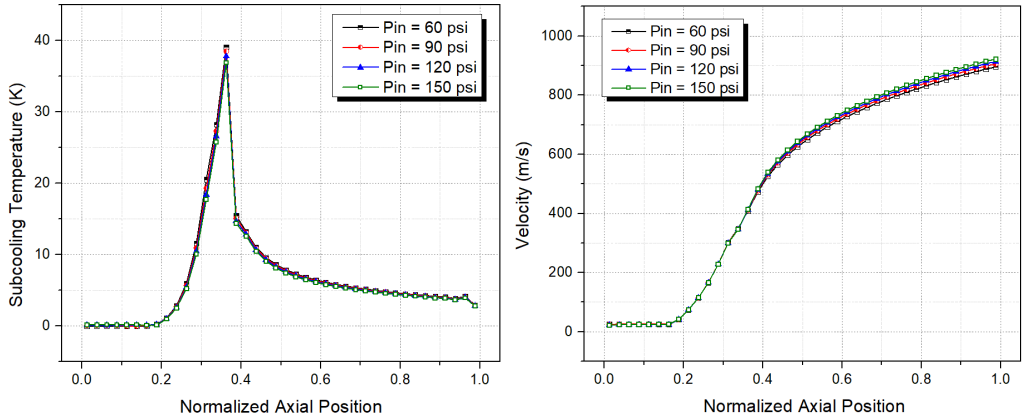

(c) Super cooling level (d) Vapor velocity

Figure 3-15. Distributions of main variables along the nozzle axis.

The nucleation condensation rate profiles and steam wetness profiles are shown in Fig. 3-16(a)-(b), respectively. The nucleation rate in these cases is much larger than the results of the Barschdorff nozzle and Moore nozzle. From Fig. 3-16(a), it can be observed that the condensation rate reaches to the peak of $50000\,\mathrm{kg/m^{-3}s}$. The dramatic increase of the nucleation rate is caused by the droplet generation, while the following gradual decline is due to the droplet growth effect. The total inlet pressure and temperature level are much higher than that of the Moore nozzle and Barschdorff nozzle. As discussed earlier, the onset of condensation is located further upstream in this case. The liquid mass fraction highly depends on the supersaturation rate and the pressure of vapor. These parameters are not much different in the diverging section; hence the outlet wetness of these cases is 11.5% to 13%.

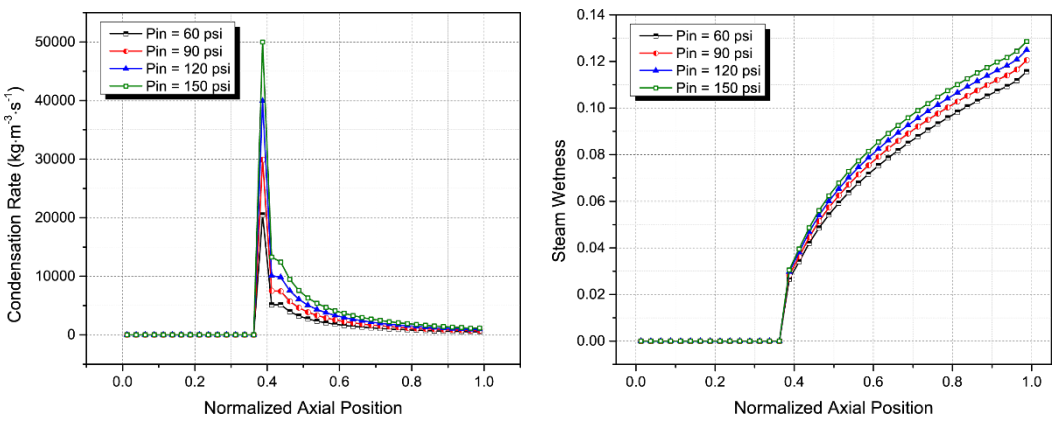

(a) Nucleation condensation rate (b) Steam wetness

Figure 3-16. Distributions of nucleation condensation along the nozzle axis.

3.2.3 SIMULATION OF THE FLOW WITH INLET DROPLETS AND HIGH LIQUID FRACTION

Due to the fact that the nozzle flow in traditional applications usually has a superheated vapor inlet condition, the experimental and the numerical studies have been focusing on the dry steam

flow with nucleation condensation process. However, there is a lack of experimental data in nozzle two-phase flow. Although extensive efforts have been made in computational multi-fluid dynamics (CMFD), nozzle flow under two-phase conditions is still very challenging to model and simulate, given complex processes and phenomena involved, especially for high pressure and high liquid fraction cases. The present nozzle model employs a two-phase four-fluid framework, which has the potential to simulate various two-phase flow regimes. To demonstrate its predictability for the two-phase mixture inlet conditions, cases with the inlet pressure of 2MPa–8MPa and inlet droplet volume fraction of 0%-5% were simulated. The flashing evaporation and nucleation condensation phenomena were also considered in the calculations.

Figures 3-17 present simulation results of the pressure, phase volume fraction, velocity, temperature and steam wetness through the Kneass nozzle. Compared with the case of the single-phase vapor inlet conditions, the vapor is slowed down due to the interfacial drag between the vapor and droplets. The velocity drop increases with the rising droplet volume fraction. The droplet outlet velocity is less than 150m/s, which is much slower than that of the dry steam case. In the convergent part of the nozzle, the vapor phase has a larger acceleration rate than the liquid phase. In general, the vapor volume fraction decreases in the convergent section, and increases again in the divergent section while expanding through the nozzle. Fig. 3-17(c) and 3-17(d) present the results of the cases with different inlet pressures. Figure 3-17(c) shows that the droplet outlet velocity increases significantly with the rising pressure, due to the increasing interfacial drag between the vapor and droplets. As shown in Fig. 3-17(d), the outlet wetness also increases significantly with the rising pressure, e.g., from about 11% to 16.7% when the pressure increases from 2MPa to 8MPa. The condensed droplet volume fraction has the same trend. But for each case, the condensed droplet volume fraction decreases after the initial rise due to the expansion of the vapor phase.

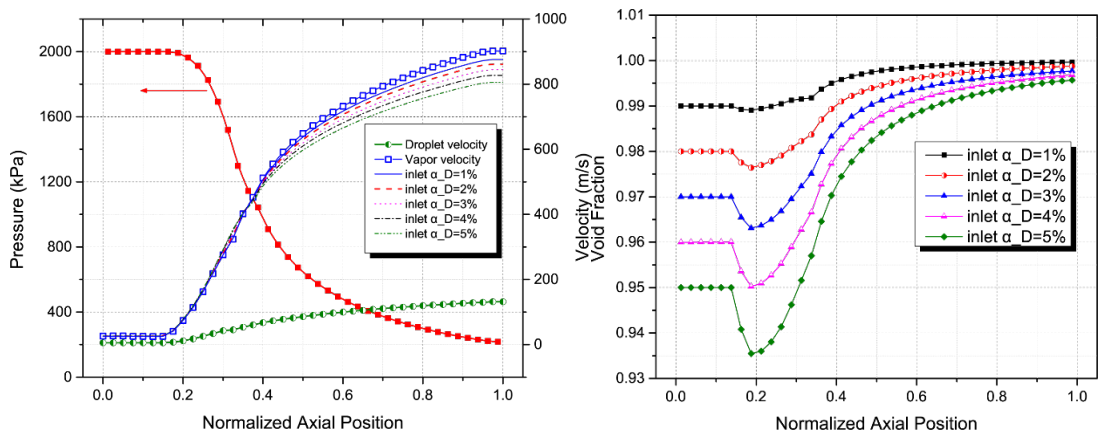

(a) Static pressure and velocity profiles of 2MPa condition (b) Void fraction of 2MPa condition

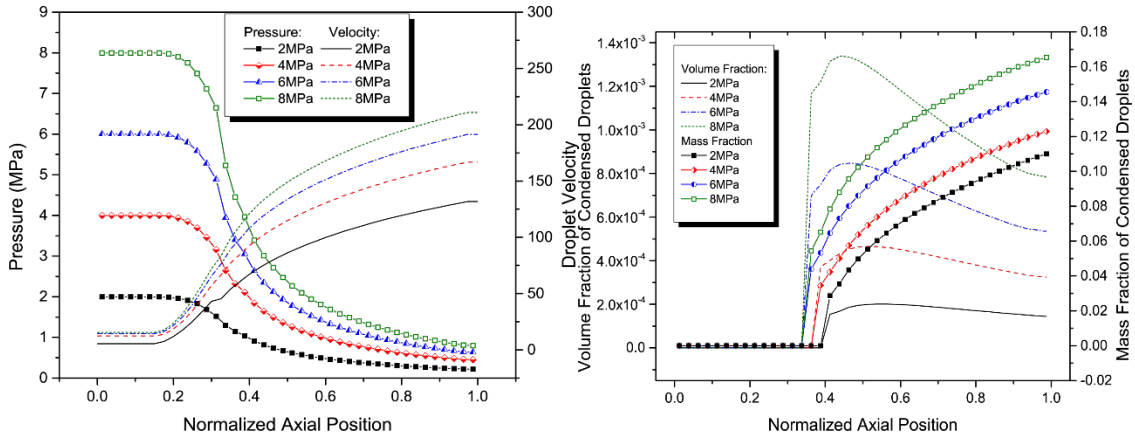

(c) Pressure and velocity profiles

(d) Fraction of condensed droplets

Figure 3-17. Results of mixture inlet conditions.

Another case was also simulated to demonstrate the capability of the current model to handle inlet high liquid volume fraction conditions, which is of interest for simulation of the nozzle flow under "off-design" conditions. The inlet pressure varies from 2MPa to 8MPa, and the constant inlet liquid volume fraction of 75% (i.e., 25% vapor volume fraction) is used for all pressure cases. Figures 3-18 show the vapor volume fractions, and vapor and liquid velocities, respectively. As compared with the case of lower liquid fraction above, the vapor velocity decreases more significantly. The void fraction decreases in the convergent section and then increases through the divergent section due to vapor expansion and liquid evaporation.

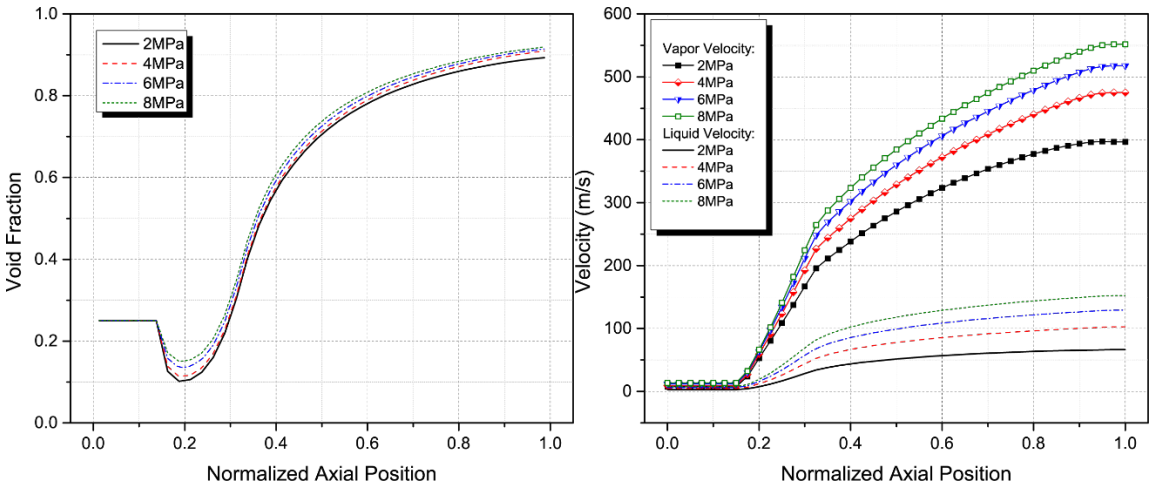

(a) Void fraction profiles

(b) Vapor and liquid velocity profiles

Figure 3-18. High liquid fraction results.

3.3 GENERATION OF NOZZLE FLOW TABLES

The Terry turbine nozzle from the reference (Beeny, 2017) was selected to obtain the nozzle flow tables using the 1D nozzle model developed. The geometry of this nozzle is scaled and shown in the Fig. 3-19. Unlike the nozzles in the previous sections, the Terry turbine nozzles

have two convergent segments. The length of the first convergent segment at the inlet is 1.97mm and the second one is 1.51mm. The divergent segment is 9.59mm. The throat diameter is 5.59mm and the nozzle inlet diameter is 7.16mm. In the test, the inlet pressure is varied from 2MPa to 8MPa to cover the operation pressure range of the RCIC system.

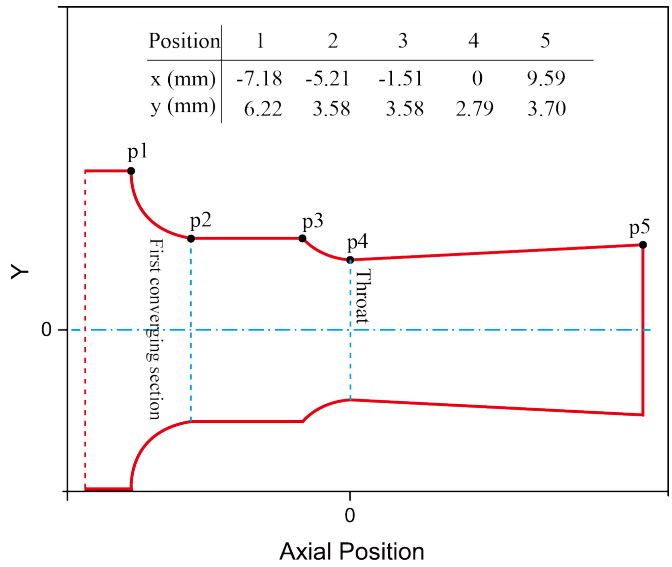

Figure 3-19. Geometry of Terry turbine nozzle.

The nozzle steam flow tables generated are given in Appendix B. Figures 3-20 depict the main flow parameters and nucleation condensation parameters of the Terry turbine nozzle with inlet pressure of 7MPa, including static pressure, phase volume fraction, velocity, temperature and steam wetness. It can be observed that the geometry of two convergent segments leads to a unique distribution of parameters compared with the previous nozzles. The pressure and temperature decrease dramatically in the second convergent part.

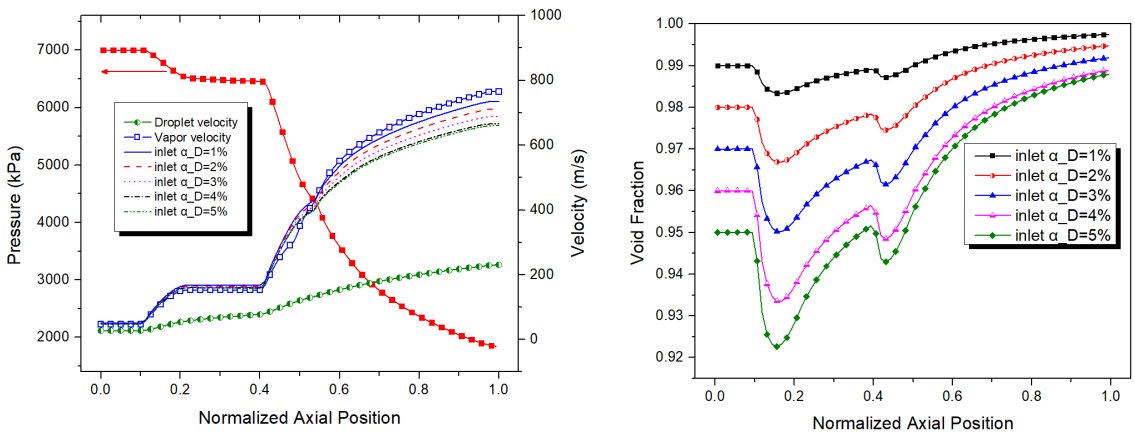

(a) Static pressure and velocity

(b) Volume fraction

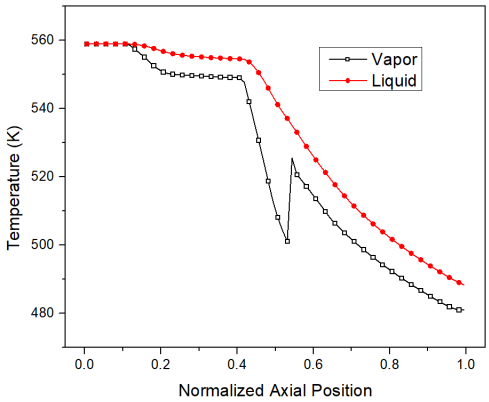

(c) Temperature

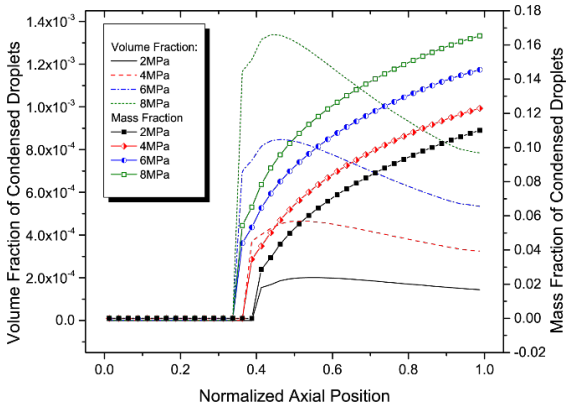

(d) Nucleation condensation

Figure 3-20. Distributions of main flow parameters along the axis of Terry nozzle.

3.4 SUMMARY

In this chapter, the accuracy of the nozzle model was evaluated by comparing with the available test data and the CFD simulation results. The presented simplified four-fluid nozzle model has the capability to model and predict the transonic steam flow with condensation in the nozzle for a wide range of inlet pressure conditions. The numerical results of the nozzle model show reasonable accuracy compared with the Moore nozzle test and Barschdorff nozzle test, which are both low pressure nozzle steam flow tests. The applicability of the nucleation condensation model, three-fluid critical model, and solution method have been verified. The results of the nozzle model for higher pressure condensing steam flow of the Kneass nozzle tests also show good agreement with the test data and CFD results. The demonstration simulations of the nozzle flow with inlet droplets and high liquid content have been presented. Then, the 1D nozzle model was employed to obtain nozzle flow tables of the Terry turbine nozzle for different working pressures which can cover the operation pressure range of the RCIC system.

4. RCIC SYSTEM-LEVEL MODEL DEVELOPMENT AND IMPLEMENTATION

Since the accident at the Fukushima-Daiichi nuclear power plant, the RCIC system has drawn special attention from industry and regulators for its apparent role in removing residual decay heat without AC and DC powers. The RCIC system is a more robust and capable safety system against core damage than previously thought, especially in the contest of BDBA like short-term station blackout events or long-term station blackout events (Beeny, 2017). The performance of key critical components such as the RCIC steam-driven turbine pump and SRVs under accident conditions is poorly known and largely based on conservative assumptions

The Terry turbine used in the RCIC system is quite different from the power turbine in nuclear systems. Thermal-hydraulic system analysis codes, such as RELAP5 and TRACE, have no available internal models developed to simulate the RCIC system. In this section, the RCIC model, especially the Terry turbine model, is developed.

4.1 RCIC SYSTEM DESCRIPTION

The RCIC system found in certain BWR power plants consists of safety-related equipment intended to provide feed coolant to the RPV when the reactor system is isolated from the power-producing steam turbine and condenser (Beeny, 2017). The RCIC system can operate independently of alternating current, service air, or external cooling water systems, making it able to play an important role in a SBO accident. The logic circuits on the controlling of governor valves in the RCIC systems can be powered by the external battery in order to control the RPV water level to avoid overfilling of the RPV, which may lead to the flooding of the steam line to the RCIC turbine.

Figure 4-1 shows the typical configuration of the RCIC system. The main functional components of the RCIC system are a steam-driven Terry turbine and a centrifugal multistage pump with a common shaft connected to each other. It also has several lines of piping and valves. The turbine is driven by high-temperature and high-pressure steam and can rapidly accelerate from standby to the full load condition within a pre-prescribed time period. The steam supply line splits off the main steam line upstream of the isolation valve. Expanded steam and water from the Terry turbine exhausts to the containment suppression pool. The turbine-driven pump delivers makeup water from the condensate storage tank (CST) or containment suppression pool. The suppression pool also condenses steam from the turbine exhaust or from SRVs. The SRVs are designed to release high-temperature steam into the containment suppression pool to depressurize the primary system and located on a steam header attached to the main steam lines leaving the reactor vessel, as shown in Fig. 4-1. The first set of SRVs are set to open at 7.72 MPa and close at 7.30 MPa in this model.

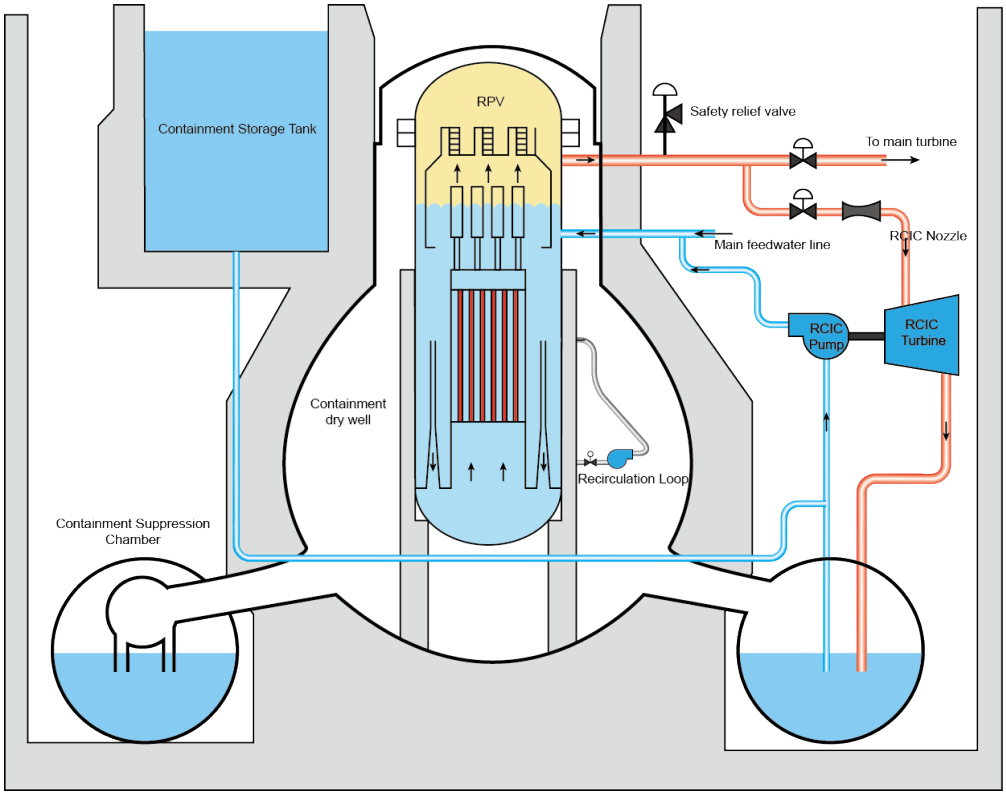

Figure 4-1. Configuration of typical BWR RCIC system

The Terry turbine is a small, single-stage, compound-velocity impulse turbine, which is quite different from the multi-stage high efficiency turbines designed for electrical power generation. Different from the reaction turbines with steam expanding through long blades, the Terry turbine operates on an impulse principle where steam with high velocity drives the rotating buckets. The Newton's Laws for a rotational system are applied to model and simulate this type of turbine. The forces applied on the turbine consists of the driving force of steam flow, shock losses in the buckets, friction losses, and torque from the shaft between the turbine and pump (Ross et al., 2015). The unique and simple design of the Terry turbine makes it satisfy the requirements for its intended applications, such as fast start up, reliable, low maintenance.

Figure 4-2 presents the schematic configuration of a typical Terry turbine. Steam enters the semi-circular buckets after expanding through the nozzles that are fixed around the wheel and reverses direction (turning through 180°) before exiting at the opposite end. Paired with each nozzle is a series of reversing chambers affixed to the inside of the casing. Reversing chambers constitute the velocity stages of the turbine because they return some portion of the steam flow to the rotor for the following impulse delivery. Each reversing chamber has a semi-circular or crescent-shaped hole in its top lateral surface that permits part of the expanded steam to vent. Since the steam is completely expanded after exiting the nozzles, the expansion process itself imparts no energy on the Terry turbine. For this reason, the pressure drop and the enthalpy change over the Terry turbine can be treated as zero, especially if no phase change occurs after steam enters the turbine (Ross et al., 2015).

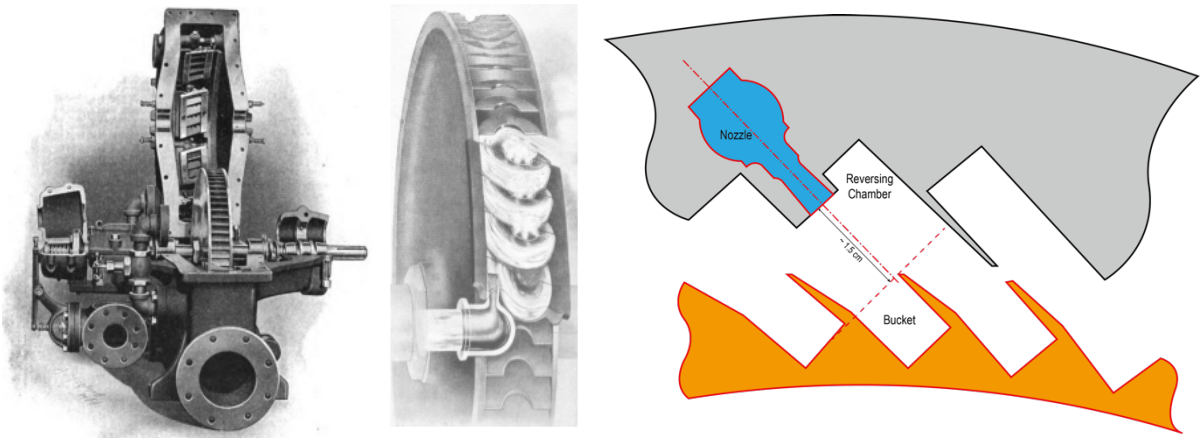

Figure 4-2. Terry turbine drawing and configuration.

4.2 TERRY TURBINE AND PUMP MODEL

Since there is no built-in model in system thermal-hydraulics codes such as TRACE and RELAP, a mechanistic model is developed to simulate the RCIC system with the nozzle injection data obtained from the 1D nozzle model developed. The governing equations for the RCIC model, pump curve models are presented in the following subsections.

4.2.1 TERRY TURBINE MODEL

The RCIC governing equation is based on a control volume formulation of the angular momentum balance approach originally proposed for Pelton turbine analysis, which was also adopted in the Sandia report (Ross et al., 2015) and TAMU research work (Beeny, 2017). The control volume is an enclosure surrounding the turbine buckets and the nozzles are outside the control volume, as shown in Fig. 4-3. The turbine responds principally to the injection of vapor and liquid water that exit the nozzles. The momentum due to the fluid delivered to the turbine buckets plays an important role in the turbine operation while the momentum flux of the fluid recirculated by the reversing chambers is only significant during system startup.

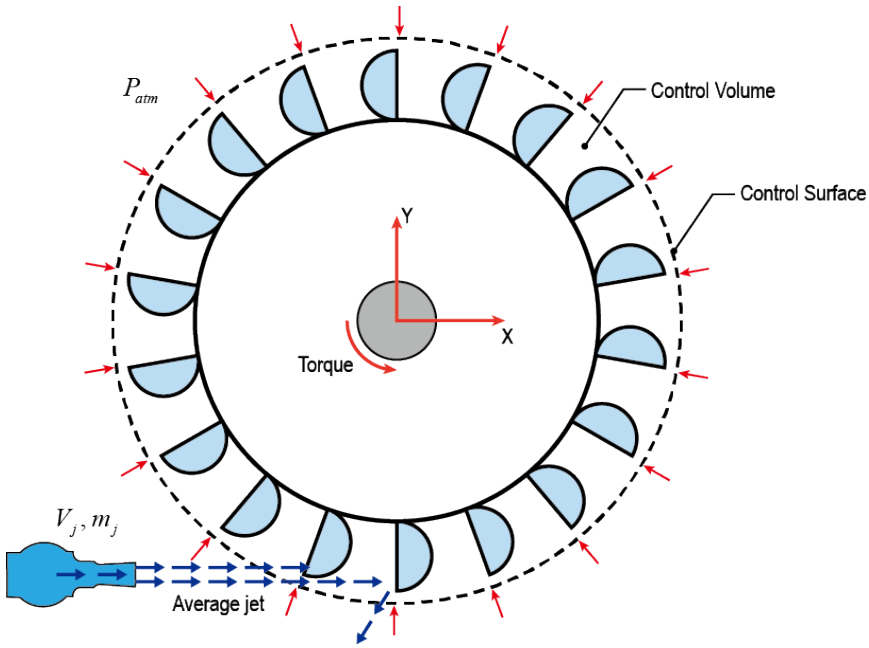

Figure 4-3. Control volume for angular momentum equation of Terry turbine.

A lumped-parameter approach is used to derive governing equations for RCIC turbine. The turbine is assumed to be adiabatic and only spin in one direction along a stationary axis. The pertinent scalar component of the angular momentum relationship for a control volume can be provided as:

$$\oiint rT_\theta \, dA + \iiint rB_\theta dV = \oiint ru_\theta \, (\rho \boldsymbol{u} \cdot dA) + \frac{\partial}{\partial t} \iiint ru_\theta \rho dV \tag{4-1}$$

where r is the radius of the turbine wheel, T_θ is the force function over the surface of the control volume A, is the area, V is the volume. B_θ is a body force such as gravity, which can be ignored for high-speed flow. ρ is the liquid density. The first term on the left-hand side of Eq. 4-1 is the shaft torque and the first term on the right-hand side represents the driving moment of the fluid flow in the buckets.

The first term in the left side of Eq. 4-1 accounts for any torques crossing the control surface. In this case, only the shaft crosses the boundary. The second term accounts for body forces and may be neglected because this analysis neglects gravity. The third term accounts for net moment of momentum flux delivered by any fluid flow crossing the control surface. This term may be expanded so that compound velocity stages (multiple entries/exits of a fluid stream across the control surface) may be taken into account. The fourth term is a transient term that contains the moment of inertia and time derivative of rotor angular speed. $\boldsymbol{u}$ is the velocity vector and u_θ is the tangential component of the outlet velocity of the fluid leaving the bucket, which can be resolved using velocity triangles.

$$u_\theta = r\omega - (V_j - r\omega) cos\beta \tag{4-2}$$

where ω is the turbine speed, V_j is the nozzle jet velocity, and β is th inlet/outlet angle between the fluid velocity vectors and the horizontal/tangential direction of the turbine motion. The shaft torque should be equal and opposite to pump torque according to Newton's Third Law:

$$\oiint rT_\theta \, dA = -T_{pump} \tag{4-3}$$

where T_{pump} is the pump torque.

For one-dimensional inlets and outlets, the first term on the right-hand side for RCIC model can be evaluation as

$$\oiint ru_\theta \, (\rho \boldsymbol{u} \cdot dA) = r^2 \sum_i \dot{m}_\iota \, \omega(1 + cos\beta) - 2r \sum_i (\dot{m}_i V_i) \, cos\beta \tag{4-4}$$

It should be noted that the $\sum_i \dot{m}_\iota$ and $\sum_i (\dot{m}_i V_i)$ represent the sum of the four individual fluids, i.e. vapor, continuous liquid, entrained droplets and nucleation condensed droplets. The mass flow rate and momentum flux terms have been expanded to include distinct terms for the liquid (subscript l) and vapor (subscript v) phases,

$$\sum_i \dot{m}_\iota = \dot{m}_g + \dot{m}_f + \dot{m}_D + \dot{m}_N \tag{4-5}$$

$$\sum_i (\dot{m}_i V_i) = \dot{m}_g V_g + \dot{m}_f V_f + \dot{m}_D V_D + \dot{m}_N V_N \tag{4-6}$$

Based on Eqs. 4-2 to 4-4, Eq. 4-1 can be rewritten as

$$-T_{pump} = r^2 \sum_i \dot{m}_\iota \, \omega(1 + cos\beta) - 2r \sum_i (\dot{m}_i V_i) \, cos\beta + \frac{\partial}{\partial t} \iiint r\left[r\omega - \left(V_j - r\omega\right) cos\beta\right] \rho dV \tag{4-7}$$

The variables, $\dot{m}_\iota$, V_i and η can be treated as pseudo-constants over each integration step and are updated each time step by TRACE for the test calculations. Two schemes are developed by SNL for the evaluation of turbine rotation speed, including quasi-steady scheme and time-dependent differential equation scheme.

Due to rather slowly evolving severe accident transients for BWR with respect to time, import variables such as RPV pressure also change slowly. Hence it is reasonable to presume that a quasi-steady scheme of the RCIC equation may be used in the transient system calculation. The turbine-pump inertia is neglected, and it is assumed the RCIC has instantaneous changes between quasi-equilibrium conditions. The time-dependent term in Eq. 4-1 is set to zero and the angular momentum equation reduces to:

$$-T_{pump} = r^2 \sum_i \dot{m}_\iota \, \omega(1 + cos\beta) - 2r \sum_i (\dot{m}_i V_i) \, cos\beta \tag{4-8}$$

4.2.2 HOMOLOGOUS PUMP MODEL

The pump model in TRACE is based on the standard homologous-curves approach. These curves represent the performance of the pump in a normalized format, giving the normalized pump head as a function of the normalized volumetric flow and normalized pump speed. Homologous curves are used because of their simplicity. These curves describe, in a compact manner, all operating states of the pump obtained by combining positive or negative pump-impeller angular velocities with positive or negative fluid volumetric flows (NRC, 2010).

Empirical homologous curves are one way of summarizing pump performance in response to given conditions. To allow one set of curves to be used for a variety of pumps, the following normalized quantities are adopted:

$$v = Q/Q_R \tag{4-9}$$

$$\alpha = \omega/\omega_R \tag{4-10}$$

$$h = H/H_R \tag{4-11}$$

where H, Q and ω are the pump head, volumetric flow and rotational speed, respectively. H_R, Q_R and ω_R are the rated variables, correspondingly.

The development of homologous torque curves parallels the above development of homologous curves. The dimensionless pump torque is defined by:

$$t = T/T_R \tag{4-12}$$

where T nd T_R are the pump hydraulic torque and rated torque, respectively.

Based on the value, q/ω or ω/q is utilized as the independent variable of head curves, as shown in Eqs. 4-13 to 4-16. The homologous torque curve segments are correlated in the same manner as the head-curve segments shown in Table

$$h/\omega^2 = f_1(q/\omega) \quad for\ 0 \leq |q/\omega| \leq 1\ and\ \omega > 0 \tag{4-13}$$

$$h/\omega^2 = f_2(q/\omega) \quad for\ 0 \leq |q/\omega| \leq 1\ and\ \omega < 0 \tag{4-14}$$

$$h/q^2 = g_1(\omega/q) \quad for\ 0 \leq |\omega/q| \leq 1\ and\ q > 0 \tag{4-15}$$

$$h/q^2 = g_2(\omega/q) \quad for\ 0 \leq |\omega/q| \leq 1\ and\ q < 0 \tag{4-16}$$

Table 4-1 summarizes the pump ratings and turbine geometry data, which are derived from information made available under the OECD-NEA's benchmark study of Accident (NEA, 2015).

Table 4-1. Input values for TRACE pump ratings and turbine data

Input variable	Values
Rated RCIC speed	4300 rpm
Rated pump heat	7.52 MPa
Rated pump torque	449 N·m
Pump injection flow area	0.0168 m^2
Homologous pump curve set	Bingham
Turbine radius	0.3 m
Nozzle inlet/outlet angle	Pi/4
Turbine moment of inertia	10kg·m^2

4.3 TRACE MODEL OF RCIC SYSTEM

The new set of RCIC models can be implemented into systems analysis codes such as TRACE to provide fast running and accurate simulations of the RCIC system. A GE BWR4 plant with the Mark I containment is employed to perform this study. The TRACE model has a reasonably detailed nodalization of the primary reactor coolant system, all of the major flow paths and system components to perform SBO accident. Figure 4-4 depicts the modified nodalization of the BWR TRACE model. The RPV is modeled using the TRACE VESSEL component with axial levels, radial rings, and azimuthal sectors representing the downcomer, lower plenum, core, upper plenum, and upper heat regions. The fuel bundles are modeled using TRACE CHAN components, including average channel and hot channel. Also modeled are the drywell and suppression chamber components with a CONTAN component. The steam lines are modeled out to the turbine control valve. The feed water system is modeled with a FILL component set up to control the feed water flow rate and obtain the steady state initial values. The original high-pressure coolant injection (HPCI), low-pressure coolant injection (LPCI) and low-pressure core spray (LPCS) injection systems are removed for the implementation of the new RCIC hydraulic elements and associated control variables. The drywell, suppression pool and containment water storage tank are kept in this model.

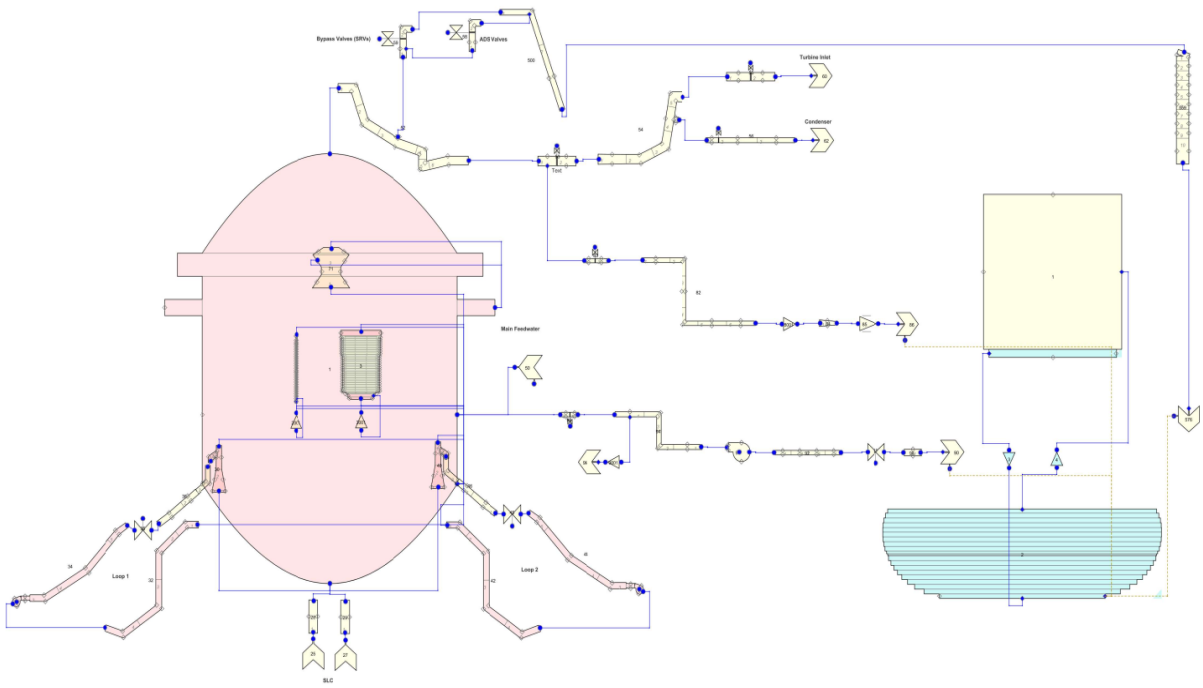

Figure 4-4. TRACE SNAP model of BWR with the RCIC system.

In this model the turbine discharge flow to the wetwell is also modeled. The pressure and water temperature of the suppression pool are important for the makeup operation. To simplify the simulation, it is assumed that the RCIC only takes suction from the suppression pool during the accident and the switchover of the suction from the CST to the suppression pool is not considered. The RCIC piping length and diameter are inferred from the SNL report (Ross et al., 2015). The RCIC governor valve, RCIC steam pipe, steam chest and a flow control component are modeled. Based on the thermal-hydraulic conditions of the steam chamber, the nozzle outlet steam flow parameters can be interpolated from the nozzle flow table in Appendix B, which is generated by the 1D nozzle calculations.

The RCIC injection component consists of the pump, pump upstream pipe, down steam pipe, governor valve and check valve. The check valve can prevent back flow through the injection piping. A minimum flow bypass line is also modeled to prevent unpredicted calculation failure of the pump to improve the stability of the TRACE model.

\

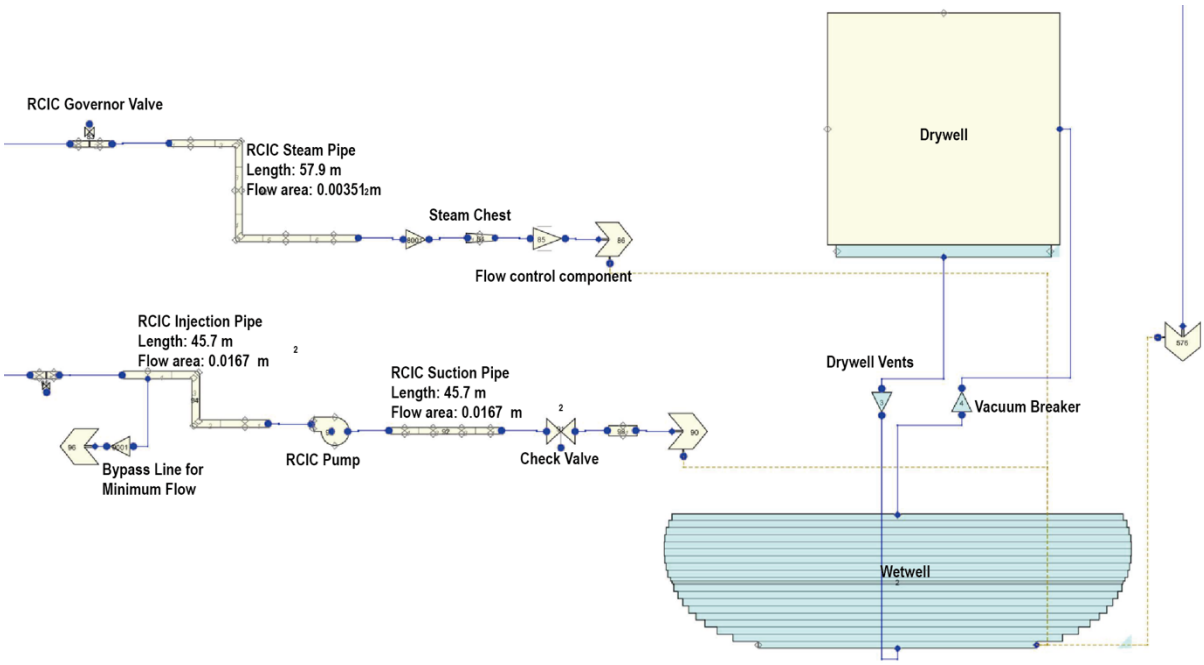

Figure 4-5. TRACE nodalization of steam piping to RCIC and injection components.

The previous correlations in Section 4.2 for the turbine drive torque are employed and implemented in the TRACE model using the control system components (signal variables, control blocks, and tables). Control blocks are mathematical functions that operate on input parameters defined by signal variables and control blocks. A SNAP schematic of the control systems for calculating the driven torque based on the steam parameters and nozzle flow tables from 1D nozzle model is shown in Fig. 4-6. The jet momentum rate for each phase in Eq. 4-4 is calculated by the nozzle two phase flow model in the previous section, including vapor, continuous liquid, entrained droplets and condensed droplets. The pressure (signal variable 149) and void fraction (signal variable 150) in the steam chest volume just before the nozzles are employed to get the interpolated values. Then these variables are utilized in the torque correlation to obtain the drive torque. The turbine drive torque is subsequently connected to the pump component. Because the RCIC-specific pump information is currently unavailable, the homologous curves for a Bingham pump is used in the current pump component.

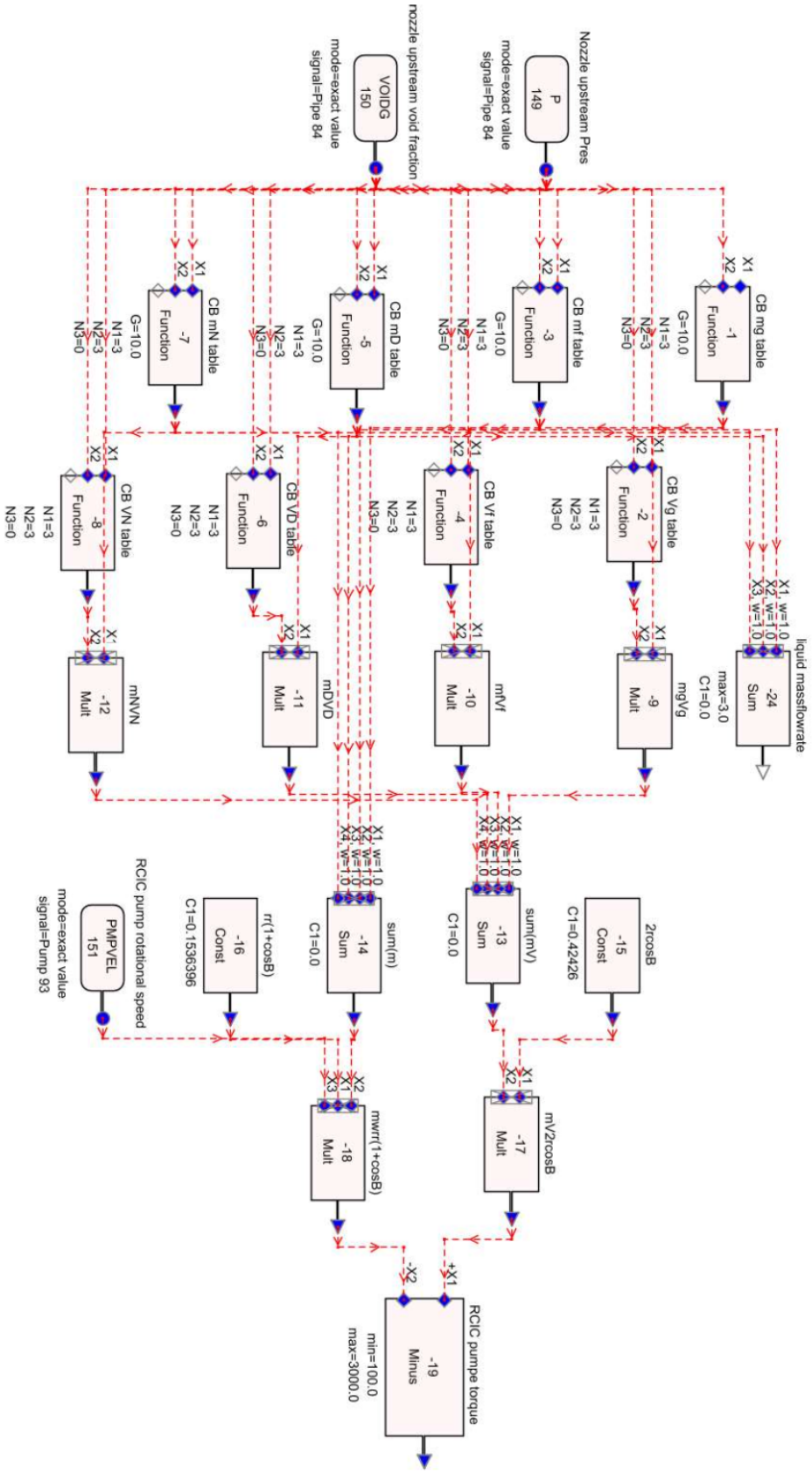

Figure 4-6. Control system for RCIC pump-turbine calculation.

4.4 RCIC SYSTEM MODEL DEMONSTRATION

Based on the TAMU's work (Beeny, 2017) on the RCIC system analysis, the SBO test problem is selected to test the new TRACE RCIC system model. The main features of this pseudo-Fukushima input have been introduced in the previous section. The overarching goal of this problem is to replicate key features of the SBO accident sequence with the operation of the RCIC system. The TRACE model can capture the feedback effect between the RPV and the RCIC system. The reactor scram is assumed to occur at time of 200s. The decay heat curve of a typical BWR is employed for the transient simulated, as shown in Fig. 4-7. The only safety systems available are the RCIC system and the SRVs. The RCIC system runs uncontrolled after the loss of electric power. It should be noted that the RCIC pump takes suction from the containment wetwell.

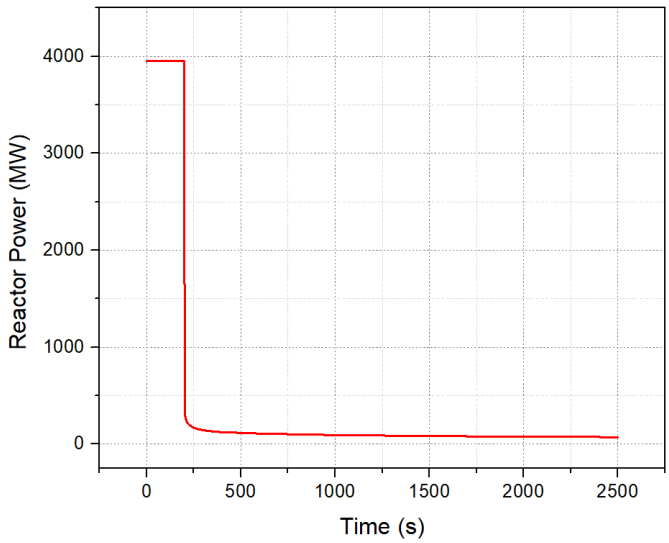

Figure 4-7. TRACE calculations of RPV pressure compared to Fukushima data.

To illustrate the functionality of the new RCIC model, various thermodynamic responses are presented and compared. For the SBO accident, the reactor downcomer water level, the RPV pressure, steam nozzle characteristics, the turbine-pump characteristics (especially the injection and rejection mass flow rates) and the suppression pool characteristics are the main parameters of interest.

Due to frequent opening and closing of with SRVs, the RPV pressure oscillates near 7.5 MPa, as shown in Fig. 4-8. During the transient, the decay heat is boiling off the liquid inventory in the RPV. The SRV cycling maintains the RPV pressure near the set-point. Figure 4-9 shows the RPV downcomer water level. Right after the reactor scram, the downcomer water level has a sharp drop. After the operation of the RCIC system starts, the makeup water from the RCIC injection loop gradually increases the water inventory and level. The simulation is stopped art 2500s. For long-term transients, the RPV over-fills may occur and the MSL could be flooded if the RCIC does not stop. The liquid could cause the failure of the RCIC turbine, stopping the pump injection.

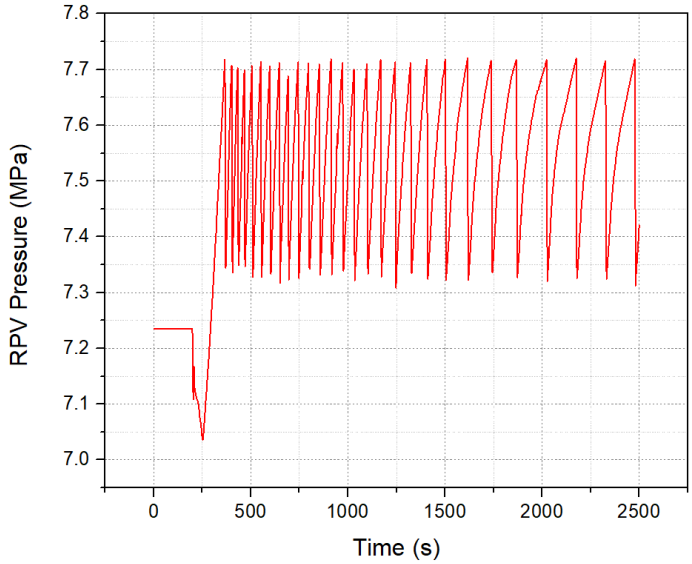

Figure 4-8. TRACE evaluation of RPV pressure.

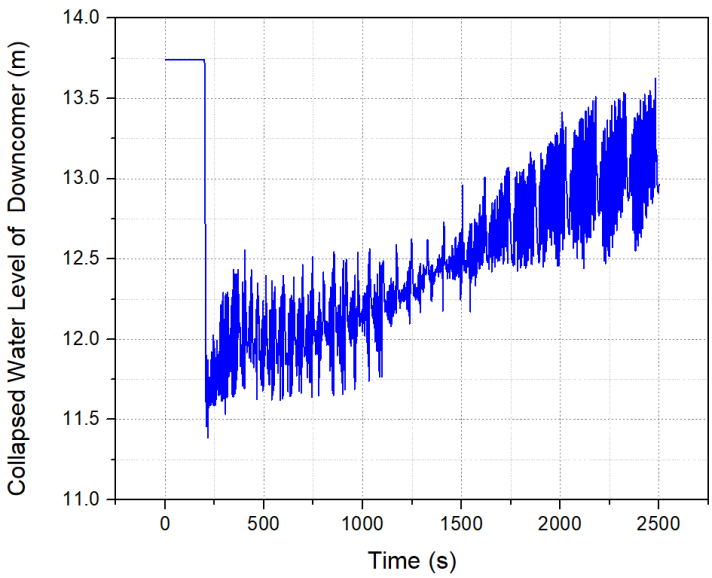

Figure 4-9. TRACE evaluation of reactor downcomer water level.

Figure 4-10 presents the void fraction change in the fuel channels and the nozzle chamber. The outlet of the fuel channels has an average void fraction of about 0.2 during the transients. The void fraction of the steam chamber before the nozzle is near 1.0 at the beginning and decreases slowly. The operation of SRVs also cause small oscillations to the void fraction of these components. Based on the void fraction and pressure of the steam chamber, the mass flow rates of each fluid phases can be obtained from the nozzle table in Appendix B. Figure 4-11 shows the mass flow rates of each phase in the RCIC turbine flow path.

In the first 1000s of the transient simulated, almost no liquid water enters the MSL. As such, the void fraction is nearly one and the liquid content can be neglected. With the decreasing inlet void fraction, the liquid mass flow rate of the turbine flow path increases accordingly. The vapor mass flow rate is relatively stable with a value of about 4 kg/s.

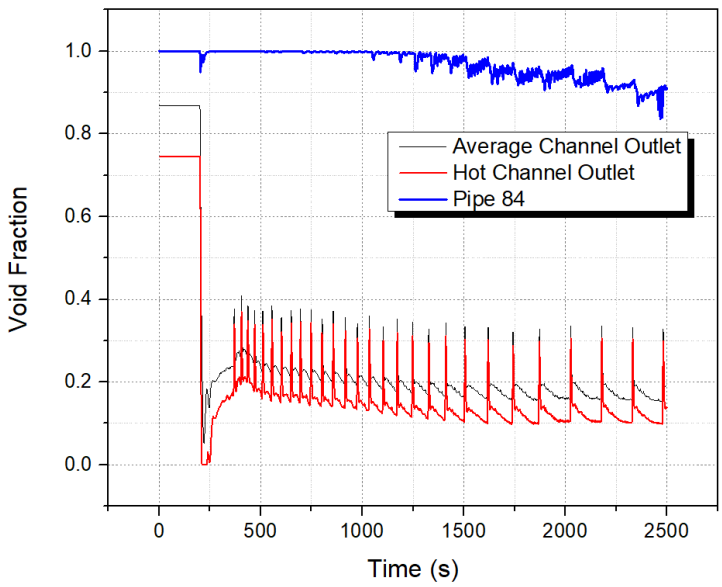

Figure 4-10. Calculated void fraction of channels and nozzle chamber.

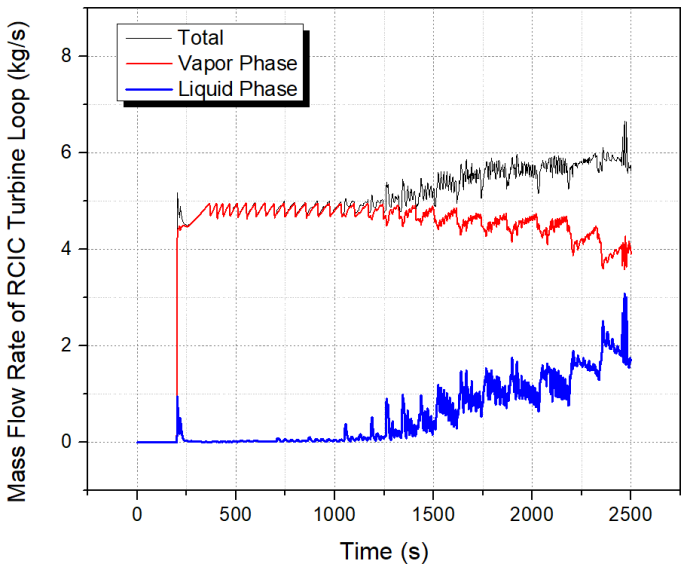

Figure 4-11. TRACE calculations of Terry turbine exhaust discharge flow rates.

The parameters of interest for the RCIC pump loop are the pump hydraulic torque, pump speed and makeup water flow rate, which are shown in Figs. 4-12 to 4-14, respectively. When the turbine governor goes full-open at about 200s, the turbine torque increases drastically. Then with the continuous operation of the RCIC system, the drive torque becomes stabilized with a value of about 1000 N·m, which gives the pump makeup rate of 44 kg/s to the RPV.

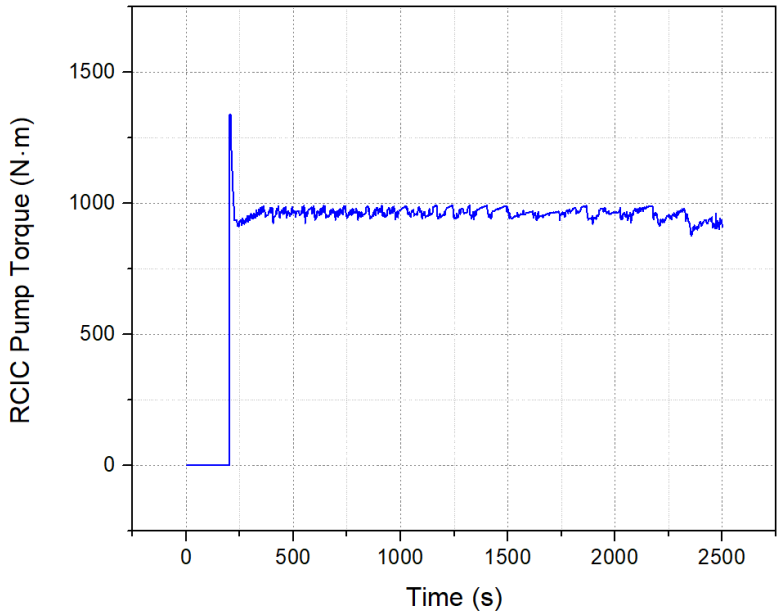

Figure 4-12. Calculated RCIC pump torque.

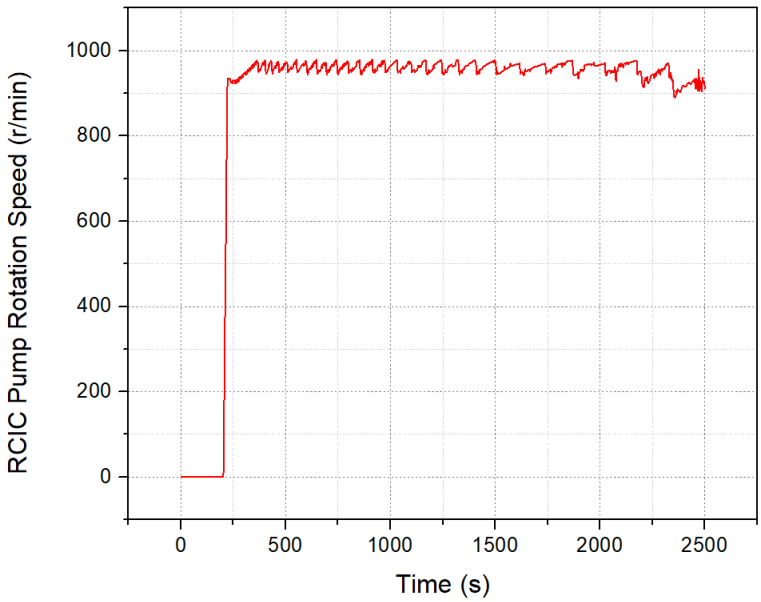

Figure 4-13. Calculated RCIC pump rotation speed.

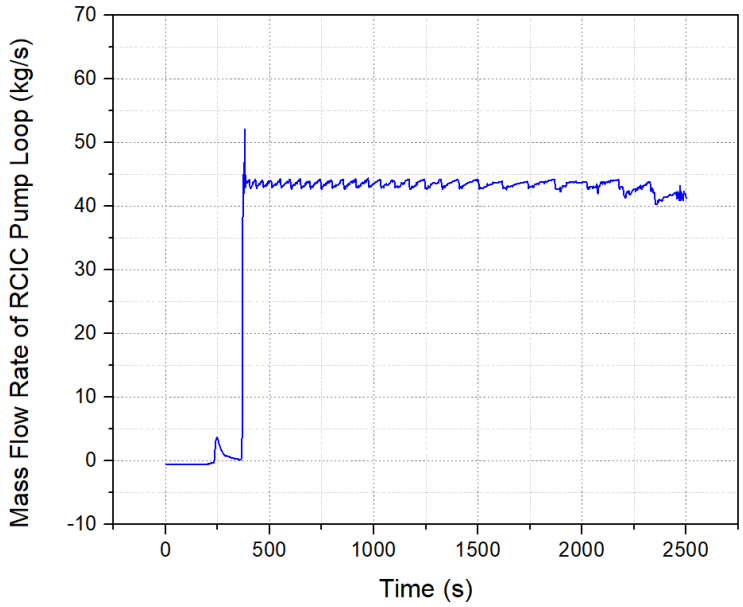

Figure 4-14. Calculated RCIC pump loop mass flow rate.

Both the RCIC turbine exhaust line and SRVs exhaust are directed to the suppression pool below the normal water level, as described in the previous section. Therefore, the suppression pool is the source of water from RCIC pump and it condenses steam from the turbine exhaust and from SRV. The steam condensation in the suppression pool leads to the increase of the pool temperature and pressure. Figure 4-15 shows the SRV mass flow rate. The containment suppression pool consists of the liquid space and the gas space above it. The liquid temperature and gas space pressure are depicted, respectively. Compared with the mass flow rate of the RCIC turbine loop, the SRVs have a much larger injection to the suppression pool. The liquid temperature of the wetwell increases from 305K to 316K during this transient. Figure 4-18 provides the liquid water mass change of the wetwell reservoir.

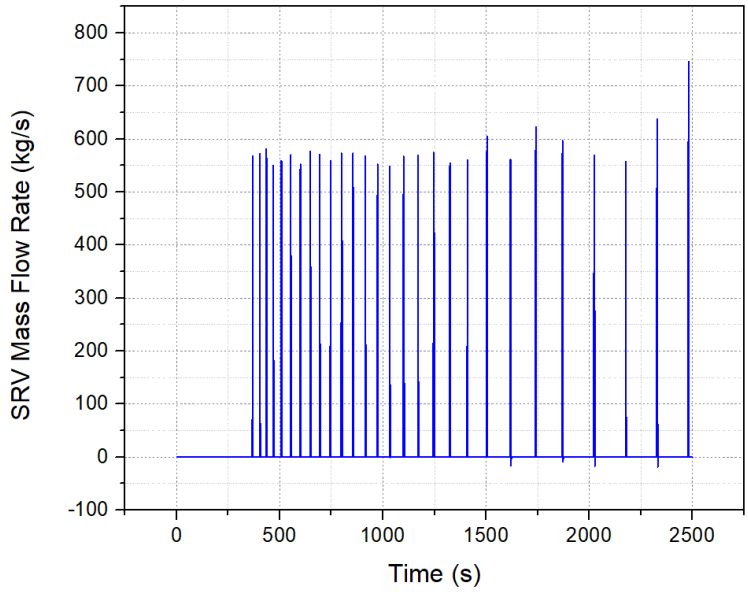

Figure 4-15. Calculated mass flow rate of SRV.

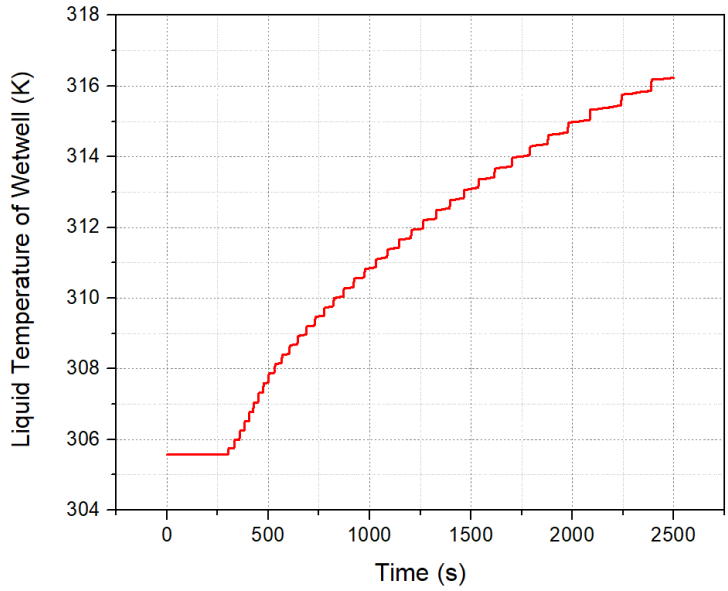

Figure 4-16. Calculated liquid temperature of wetwell.

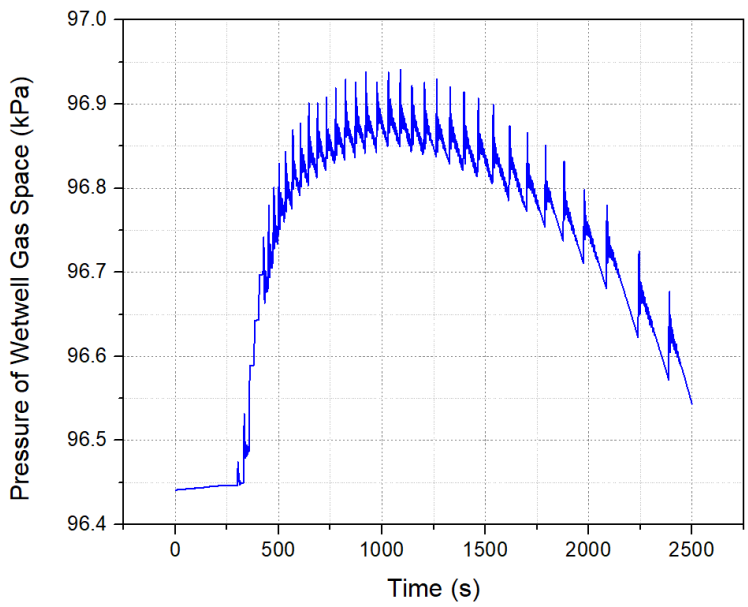

Figure 4-17. Calculated pressure of wetwell gas space.

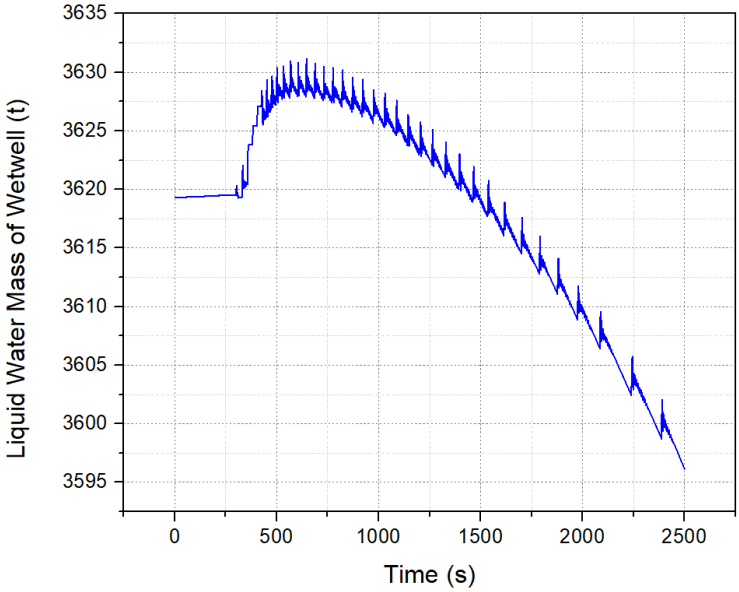

Figure 4-18. Calculated liquid water mass of wetwell reservoir.

4.5 ATF DEMONSTRATION

Accident tolerant fuels (ATFs) are fuel/cladding that, in comparison with the standard UO_2/Zircaloy system, can tolerate loss of active cooling in the core for a considerably longer time period while maintaining or improving the fuel performance during normal operations (Ott et al., 2014). The purpose of this section is to illustrate the impact of these new candidate fuel/cladding materials on the fuel performance at accident conditions.

The short-term SBO simulations were performed for two cladding materials: Zircaloy and FeCrAl. The first one is the reference case in which the fuel and cladding materials are conventional UO_2 and Zircaloy. In the second case only the fuel cladding is changed to FeCrAl. Note that the replacement of the fuel and cladding materials is only made to the hottest fuel bundle. It means that all other fuel bundles still use the same UO_2 fuel and the same Zircaloy cladding. And the new cladding was assumed to have the same geometry, dimensions and flow characteristics as the nominal UO_2-Zr based core. Hence, these changes have no impact on overall core thermal-hydraulic conditions during the SBO accident.

The fuel assembly used in the TRACE model is composed of 78 full-length fuel rods, 14 part-length rods, and two large central water rods in a 10×10 lattice array, as shown in Fig. 4-19. Design parameters of the GE14 fuel are summarized in Table 4-2. In the axial direction, the fuel rods are divided into 25 nodes.

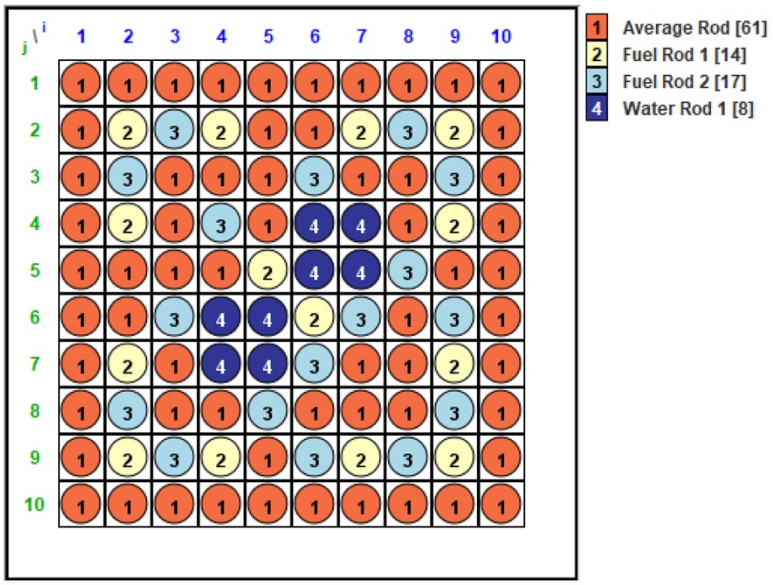

Figure 4-19. Bundle configuration 10×10 fuel assembly.

Table 4-2. Fuel and cladding dimensional design parameters.

Parameters	Values
Fuel pellet diameter / mm	8.7633
Fuel rod pitch / mm	1.2954
Gap thickness / mm	0.0889
Cladding thickness /mm	0.6604
Active fuel length /m	3.81
Active fuel length (part-length rods) / m	2.4384

The cladding materials to be examined are Zircaloy and FeCrAl. FeCrAl consists of ⩾69.52%, 20.5-23.5% Cr, 5.8% Al, ⩽0.08% C, ⩽0.4% Mn, and ⩽0.7% Si (Ott et al., 2014). The FeCrAl properties were defined in TRACE code with the user defined material. The thermal properties are presented in Figs. 4-20 to 4-22 for these two cladding materials. Zircaloy has a sharp spike in specific heat capacity because it undergoes a phase change (alpha to beta) from 1090 K to 1248 K. FeCrAl also demonstrates a peak in the specific heat capacity due to a magnetic phase transition. Note that volumetric heat capacity and thermal conductivity play a key role in the heat-up of the fuel and cladding (i.e., slower transient thermal response). The lower the thermal conductivity, the higher the initial component temperatures and thus the higher the initial stored energy.

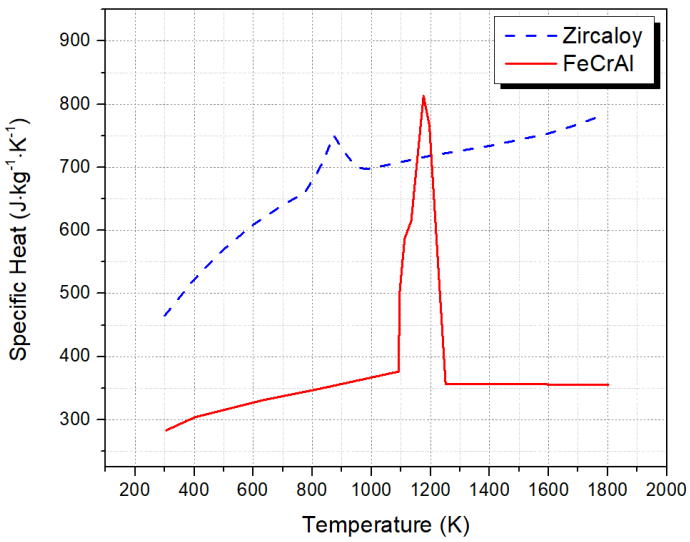

Figure 4-20. Specific heat of two cladding materials.

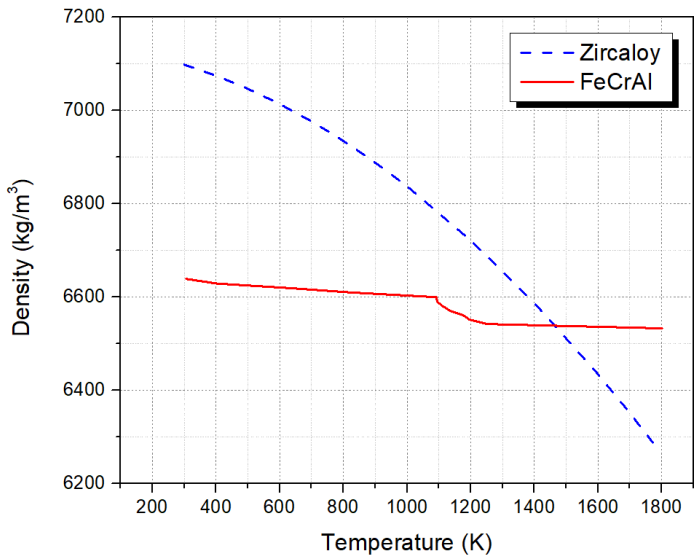

Figure 4-21. Density of two cladding materials.

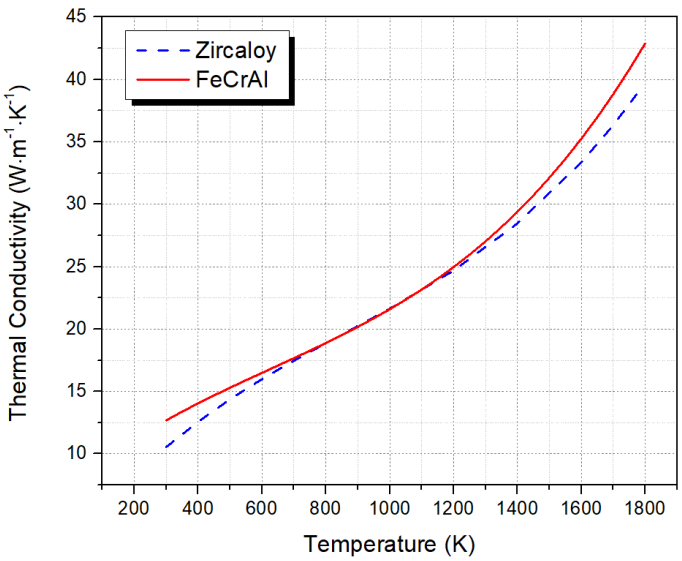

Figure 4-22. Thermal conductivity of two cladding materials.

The short-term SBO assumes the reactor shunts down (SCRAM) and all injections are lost at time zero of the transient. Two scenarios were investigated. The RCIC system was still available in the first scenario while unavailable in the second scenario. As in section 4.4, the reactor operates in the nominal power in the first 200s. The SCRAM occurs at 200s.

Figure 4-23 compares the water level change in the two scenarios. With the RCIC operation, the RPV water level can be maintained and the core would not uncover. If the RCIC system fails during the short-term SBO, then this scenario will develop into the BDBA. The downcomer water level starts to drop at the very beginning of the transient. The maximum peak cladding temperature reaches 1541K for the UO_2-FeCrAl case and 1639 K for the conventional UO_2-Zircaloy case, as shown in Fig. 4-24. This scenario demonstrates that the FeCrAl cladding has the superior performance in terms of heat-up as compared with the Zircaloy cladding. It should be noted that FeCrAl also has better performance in the metal-water oxidation kinetics than Zircaloy.

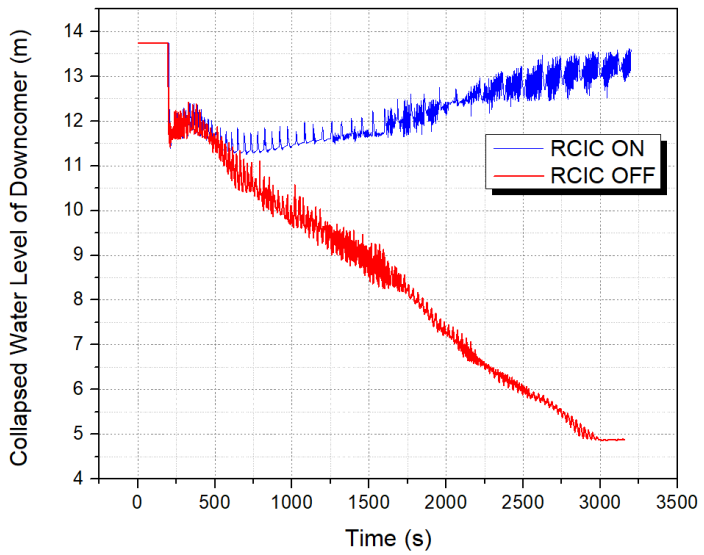

Figure 4-23. Collapsed water level of Downcomer.

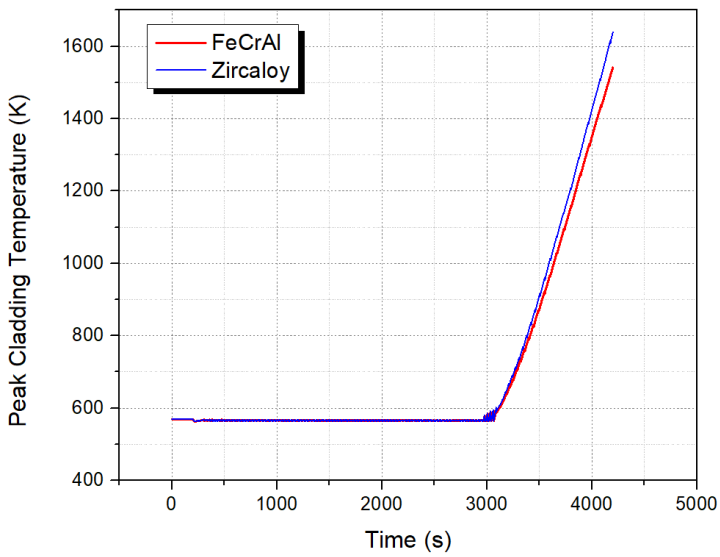

Figure 4-24. Peak cladding temperatures (without RCIC operation).

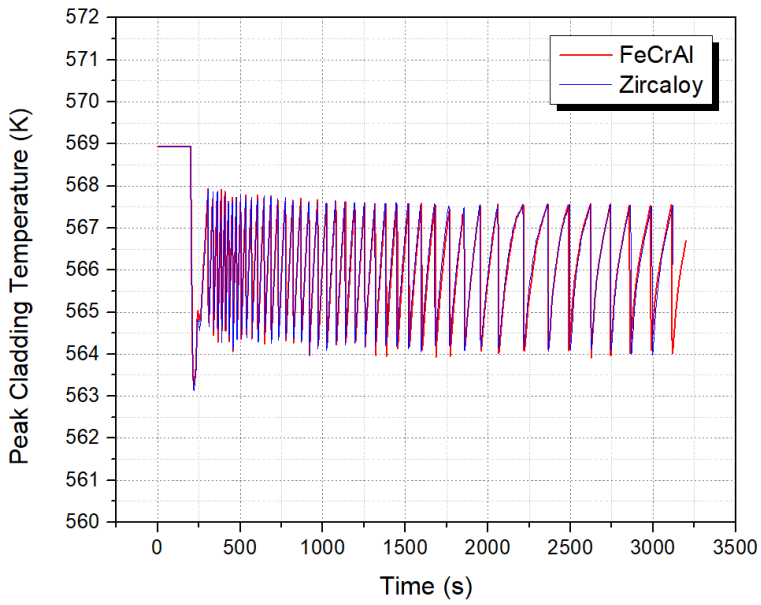

Figure 4-25. Peak cladding temperature (with RCIC operation).

4.6 SUMMARY

This section presents the development and implementation of a mechanistic RCIC model. The governing equation is based on the control volume formulation of the angular momentum balance approach. The TRCE model of a typical BWR is employed to perform this study. Based on the turbine inlet steam conditions, the nozzle injection flow can be obtained from 1D nozzle model. The correlations for the turbine drive torque are employed and implemented in the TRACE model using the TARCE control system variables. A SBO test problem was selected to test the new TRACE RCIC model. The operation of the RCIC system, SRVs cycling, the RPV pressure and water level, and the containment responses were simulated. The short-term SBO simulations were also performed for two cladding materials: Zircaloy and FeCrAl. Analyses are presented that illustrate the impact of the FeCrAl cladding material on the fuel performance under BDBA conditions.

5. DEVELOPMENT AND IMPLEMENTATION OF STRATIFIED WETWELL MODEL

Due to recent progress at Sandia National Laboratories in RCIC turbine and pump model development for MELCOR, it was decided that the wetwell component had the most room for model improvement. The suppression pool temperature distribution has a very large impact on both RPV and containment pressure. Thus, the project novel contributions come mainly from an improved, systems-level wetwell model which can capture buoyancy-induced thermal stratification effects due to steam injection and condensation. The main quantities of interest for this system study are the wetwell pressure and temperature profiles.

5.1 POOL THERMAL STRATIFICATION

Thermal stratification refers to the phenomena of a temperature gradient forming in a fluid, often due to fluid density differences. There is evidence that thermal stratification may occur in the wetwell, as seen in various experimental investigations (Laine and Puustinen, 2005; Pellegrini et al., 2016; Patterson, 1979). Thermal stratification does not refer to local hot or cold spots in the pool, instead it is the longer term presence of considerable temperature gradients over large regions of the pool. Thermal stratification may be seen vertically, horizontally, or in any irregular shape, however, due to temperature-induced density differences of water, thermal stratification expressed vertically is expected to be more stable (Solom, 2016).

Thermal stratification in the wetwell could be a safety issue for a few reasons. If the RCIC pump were to draw water from a warmer region, then the pump could potentially exceed its inlet temperature limit before a thermally mixed pool would (Solom, 2016). If the opposite were true and the pump drew water from a colder region, it would instead increase the pool's thermal capacity and pump operation time. While this would be beneficial from a pump operation standpoint, it limits the thermal and pressure suppression capacity of the pool. For instance, if heat is injected into an upper, warmer portion of the pool only, the lower colder portion of the pool does not contribute to the thermal loading. The pool surface temperature determines the containment gas space steam partial pressure. For two pools with the same average temperature, a stratified pool would have a higher surface temperature and thus higher containment pressure as compared to a well-mixed pool. Additionally, the warmer portion of the pool may reach saturation and fail to condense the injected steam. In such cases, uncondensed steam could escape from the pool surface which would lead to even higher containment pressurization.

A typical thermal stratification arrangement in suppression pools occurs when steam is injected at some middle pool elevation. The injected steam creates a buoyant thermal plume which transports heat and mass upwards towards the pool surface. This creates an upper, hot layer of water that grows, slowly moves down, and eventually a temperature gradient forms due to buoyancy. When there are no momentum mixing effects from steam injection, a pure buoyancy-induced thermal stratification case will result. A clear example of this is can be seen

in the pool heater experiment presented by Peterson (Christensen and Peterson, 2001) and simulated in Section 5.2.1. In this experiment, a heater with a constant heat flux is placed in a large tank of water. A buoyant thermal plume forms directly above the heater location. This hot plume entrains some cold ambient water with it as it moves upward and then spreads out across the pool ceiling. This process can be seen in Fig. 5-1 with the heat source denoted as F_0.

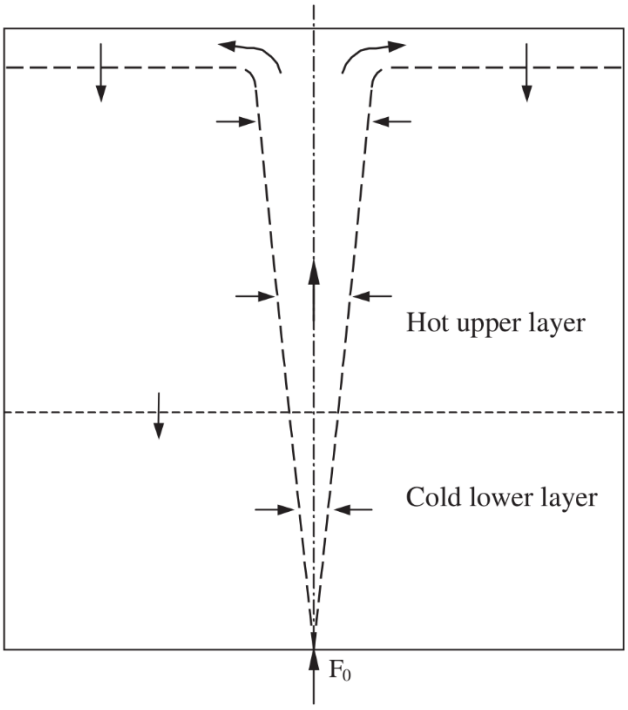

Figure 5-1. Sketch of development of a stratified environment due to a heat source, showing the motions in the plume and environment (Zhao, 2003).

In actual suppression pool operation, injected steam provides a large momentum flux which causes some amount of mixing in the pool. This momentum mixing effect creates very complicated flow patterns which require detailed and expensive 3D CFD simulations to fully resolve. Modeling this level of detail is beyond the capability for systems-level safety analysis codes, due to both the time (and thus expense) of studied transients and the amount of uncertainty in the needed input parameters. For example, the steam condensation process alone depends on many variables such as pool geometry, injection pipe or sparger geometry, injection point and pool subcooling. If any of these model inputs are uncertain, the exact flow pattern solution may be very different. However, the overall pool behavior may be able to be characterized without a fully resolved, expensive, 3D model.

5.1.1 STABLY STRATIFIED CRITERION

Steam injection into a water pool (and subsequent condensation) is a source of both heat and momentum. Competition between these two sources determines to what degree the pool is

thermally stratified or mixed (Li et al., 2014). When steam is injected downward into the suppression pool, the inertial force of the injected steam is at odds with the steam (or condensed water) buoyancy. "Buoyancy induced by hot condensate contributes to upward flow, but steam bubble interface creates upward and downward flow (Song et al., 2014)." "The complicated action created by buoyancy from hot condensate and momentum from oscillating steam interface determines whether or not the thermal stratification occurs and how the stratification process takes place (Song et al., 2014)." If this inertial force is not stronger than the buoyancy force, then only the upper regions of the suppression pool will be heated by natural convection (Song et al., 2014). For low momentum steam injection, latent heat is deposited in the water layer above the injection pipe while water below this pipe remains cold. However, steam injections with a higher momentum source can lead to large scale pool circulation which can degrade the stratified layer.

A scaling analysis by Peterson (Peterson, 1994) has shown that, depending on the mixing source strength and aspect ratio of the enclosure, the ambient fluid "tends to organize into either a homogeneously mixed condition or a vertically stratified condition (Zhao et al., 2014)" and "stratified mixing processes in large complex enclosures can be described by using 1D differential equations, with transport in free and wall jets modeled using 1D integral models" (Zhao et al., 2014). In this case, the detailed geometry of the enclosure is not important, instead "only the horizontal cross-sectional area and perimeter must be specified as a function of elevation".

Peterson (Peterson, 1994) used a scaling analysis to develop a general criterion to determine whether a pool with fluid injected into it would reach stable thermal stratification or not. His criterion can be seen in the following inequality.

$$\left(\frac{H_{sf}}{d_{bjo}}\right) Ri_{d_{bjo}}^{1/3} \left(1 + \frac{d_{bjo}}{4\sqrt{2}\alpha_T H_{sf}}\right)^{2/3} > 1, \tag{5-1}$$

where the jet Richardson number is given by

$$Ri_{d_{bjo}} = \frac{(\rho_a - \rho_o) g d_{bjo}}{\rho_a U_o^2}. \tag{5-2}$$

The subscript sf indicates stratified ambient fluid, bj indicates buoyant jet, and o indicates source of jet; d_{bjo} is the source diameter of buoyant jet, α_T is the jet entrainment coefficient, and H_{sf} is height of the stratified ambient fluid; U_o is the source velocity of buoyant jet.

"The Richardson number Ri represents the relative importance of natural convection, driven by the density difference, and forced convection, driven by the source momentum flux" (Hunt and van den Bremer, 2010).

5.1.2 BUOYANT JETS

The following section concerning buoyant jet flow structures and their quantification parameters relates to this research because the RCIC turbine steam exhaust into the wetwell creates a buoyant jet. The initial downward momentum flux promotes mixing in the pool and is at odds with the density difference-induced buoyancy flux which promotes thermal stratification in the pool.

a) Jets and plumes

Steam injection into the wetwell results in a flow structure in the ambient volume with dominant flow direction and length scale much less than the volume scale. In this project, "we will call a fluid motion a jet if its primary source of kinetic energy and momentum flux is a pressure drop through an orifice. A fluid motion whose main source of kinetic energy and momentum flux is body forces we call a plume. Flows whose motion is in transition from a jet to a plume we call a forced plume or buoyant jet" (List, 1982). Typically, jets with a different fluid density from the ambient do transition to plumes.

Steam injection (and subsequent condensation) into the wetwell results in a buoyant jet. This buoyant jet entrains water from the ambient volume as it flows upward and finally discharges towards the top of the pool.

Jets and plumes can be quantified by several different parameters. For pure jets, the case with no buoyancy, the major parameters are volume flux, Q, and kinematic momentum flux, M. For round jets with top-hat profiles, these quantities (at the injection point) are defined as (Hunt and van den Bremer, 2010)

$$Q = \pi u b^2, \; and \tag{5-3}$$

$$M = \pi \eta u^2 b^2, \tag{5-4}$$

where b is the jet radius, u is the mean vertical jet velocity, and $\eta = \rho/\rho_{amb}$ is a means to scale the momentum flux on the ambient density.

For plumes with negligible initial momentum, a more meaningful quantity is the kinematic buoyancy flux, B. For heat-driven, thermal plumes,

$$B = \frac{g\beta\dot{q}}{\rho_a c_p}, \tag{5-5}$$

where gravitational acceleration is g, constant of thermal expansion coefficient is β, heating rate is $\dot{q}$, ambient fluid density is ρ_a, and specific heat at constant pressure is c_p (List, 1982).

For discharge situations, it is more common for buoyancy flux to be determined by a difference in density,

$$B = \frac{g\Delta\rho_o Q}{\rho_a}, \tag{5-6}$$

where $\Delta\rho_o$ is the difference in density between the two fluids being considered (List, 1982).

The densimetric Froude number is a quantitative measure of relative jet momentum since it compares the momentum effect in the numerator to the buoyancy effect in the denominator (Gebhart et al., 1988).

$$Fr = \frac{u}{\{gd_{bjo}[(\rho_{amb} - \rho)/\rho]\}^{1/2}} \tag{5-7}$$

The momentum level is described with the discharge velocity u. The buoyancy effect, $(\rho_{amb} - \rho)/\rho$, is a measure of velocity generated by the buoyancy force. Thus, the densimetric Froude number tends toward 0 for pure plumes and toward infinity for pure jets (Gebhart et al., 1988).

b) Vertical buoyant jet integral model

An integral model for axisymmetric vertical buoyant jets from (Zhao, 2003; Gebhart et al., 1988; Morton, 1959) is presented here. The coordinate system for the buoyant jet can be seen in Fig. 5-2.

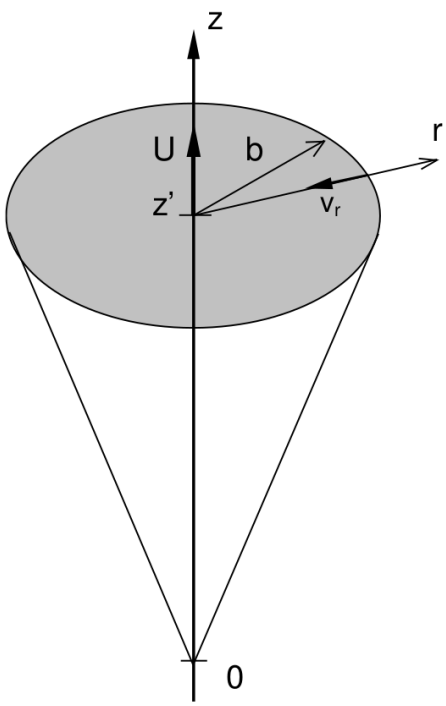

Figure 5-2. Axisymmetric buoyant jet (Zhao, 2003).

The general governing equations for flow throughout the discharge field (conservation of mass, momentum, energy, and species) are written as (Gebhart et al., 1988):

$$\frac{D\rho}{D\tau} = -\rho\nabla \cdot \vec{V} \tag{5-8}$$

$$\rho \frac{D\vec{V}}{D\tau} = \rho\vec{g} - \nabla p + \mu\nabla^2\vec{V}, \tag{5-9}$$

$$\rho c_p \frac{Dt}{D\tau} = \nabla \cdot k\nabla t + \beta T \frac{Dp}{D\tau} + \mu\Phi + q''', \textit{and} \tag{5-10}$$

$$\frac{DC}{D\tau} = \nabla \cdot D\nabla C + c'''. \tag{5-11}$$

These are in terms of local instantaneous values of velocity vector $\vec{V}$, density ρ, pressure p, temperature t, and concentration C. The terms on the left side are the transient and convective terms (Gebhart et al., 1988). The terms on the right side include the molecular diffusion and other terms such as sources. $\vec{g}$ is the gravity vector, μ is dynamic viscosity, c_p is specific heat at constant pressure, k is thermal conductivity, β is the thermal expansion coefficient, T is the reference temperature, Φ is viscous dissipation, q''' is volumetric energy generation rate, and c''' is volumetric production of species C (Zhao, 2003).

The main assumptions used in this integral model are:

1. Fully turbulent flow
2. Streamwise turbulent transport is negligible compared to convective transport
3. The variation of density throughout the flow field is small compared to the density level. The density variation is included only in buoyancy, with the Boussinesq approximation.
4. Other fluid properties are treated as constant
5. Pressure is hydrostatic throughout
6. The flow remains axisymmetric throughout the region of analysis

For a steady vertical circular buoyant jet in a quiescent ambient medium, the general governing conservation equations reduce to:

$$\frac{\partial \bar{u}}{\partial z} + \frac{1}{r}\frac{\partial}{\partial r}(r\bar{v}) = 0, \tag{5-12}$$

$$\frac{\partial}{\partial z}(\rho\bar{u}^2) + \frac{1}{r}\frac{\partial}{\partial r}(r\bar{u}\bar{v}) = -\frac{1}{r}\frac{\partial}{\partial r}(\rho\overline{u'v'}) - g(\rho - \rho_\infty), \tag{5-13}$$

$$\frac{\partial}{\partial z}(\rho\bar{u}\bar{t}) + \frac{1}{r}\frac{\partial}{\partial r}(\rho\bar{v}\bar{t}) = -\frac{\partial}{\partial z}(\overline{\rho v't'}), \tag{5-14}$$

$$\frac{\partial}{\partial z}(\rho\bar{u}\bar{C}) + \frac{1}{r}\frac{\partial}{\partial r}(\rho\bar{v}\bar{C}) = -\frac{\partial}{\partial z}(\overline{\rho v'C'}), \tag{5-15}$$

where $\bar{u}$ and $\bar{v}$ are the time-averaged velocities in the z (vertical upward) and r (radial) directions, respectively, u' and v' the fluctuating values, $\bar{t}$ and $\bar{C}$ the time-averaged temperature and species concentration values, and $\bar{t}$ and $\bar{C}$ the fluctuations in temperature and species concentration (Zhao, 2003).

The integral model method assumes velocity, temperature, and concentration profiles based on experimental observations. The above partial differential governing equations are integrated over the flow cross section to obtain ordinary differential equations. The integral model is completed by assuming an ambient fluid entrainment rate model, usually as a function of the local centerline velocity (Gebhart et al., 1988). The integral equations are (Zhao, 2003):

$$\frac{d}{dz}\int_0^\infty \bar{u} r dr = E, \tag{5-16}$$

$$\frac{d}{dz}\int_0^\infty \rho \bar{u}^2 r dr = g\int_0^\infty (\rho_\infty - \rho) r dr\,, \tag{5-17}$$

$$\frac{d}{dz}\int_0^\infty \rho \bar{u}(\bar{t} - t_\infty) r dr = -\frac{dt_\infty}{dz}\int_0^\infty \rho \bar{u} r dr\,, \textit{and} \tag{5-18}$$

$$\frac{d}{dz}\int_0^\infty \rho \bar{u}(\bar{C} - C_\infty) r dr = -\frac{dC_\infty}{dz}\int_0^\infty \rho \bar{u} r dr\,. \tag{5-19}$$

For free circular jets, the entrainment E (which represents the volume rate of the ambient fluid being entrained into the jet due to turbulence per unit jet streamwise length per unit radial angle) is defined by

$$E(s) = -\frac{1}{2\pi}\int_C v_r(b) dC = -v_r(b) b, \tag{5-20}$$

where v_r is the velocity in the r direction and b is the nominal jet radius (Zhao, 2003). A dimensionless entrainment coefficient can be defined as

$$\varepsilon = \frac{E}{bU}, \tag{5-21}$$

Where U is the plume centerline velocity in the jet advance direction (Zhao, 2003).

Continuing from the previously derived integral equations, the Morton plume model is presented here. Morton (Morton, 1959) used the fundamental assumption by G.I. Taylor that the entrainment velocity v_r is a fraction, α, of the buoyant jet centerline velocity U" (Zhao, 2003). The Morton plume model is valid for vertical buoyant jets generated by both thermal expansion and vertically injected fluid (Zhao, 2003) (the sign of the buoyancy and the injection direction must match). Gaussian profiles are assumed for the plume mean vertical velocity

$$\bar{u}(z,r) = U(z)\, exp\left(-\frac{r^2}{b^2}\right), \tag{5-22}$$

and mean buoyancy

$$g(\rho_a - \rho)(z,r) = \rho_{a,0} g'(z)\, exp\left(-\frac{r^2}{\lambda^2 b^2}\right), \tag{5-23}$$

where $\rho_{a,0} = \rho_a(0)$ is the reference density and g' the reduced gravitational acceleration defined as

$$g' = g\frac{\rho_a - \rho_0}{\rho_{a,0}}, \tag{5-24}$$

where ρ_0 is the centerline density of the jet.

The concepts of average velocity w and radius R for a buoyant jet are useful. They are defined by integrating the mass and momentum fluxes across the plume:

$$wR^2 = 2\int_0^\infty u(r) r dr\,, and \tag{5-25}$$

$$w^2R^2 = 2\int_0^\infty u^2(r) r dr\,. \tag{5-26}$$

For the Gaussian velocity profile, the following two relations can be made.

$$R = \sqrt{2}b \tag{5-27}$$

$$w = \frac{U}{2} \tag{5-28}$$

"For the top hat profile, $R = b$ and $w = U$" (Zhao, 2003). It is important to note that the equations derived in this subsection assume a Gaussian profile unless explicitly stated.

It is assumed that the variation of density in the plume along the cross section is small that $\rho(r,z)$ can be approximated by ρ_0. This assumption combined with the Gaussian velocity and buoyancy profiles, reduces the integral equations to the following (Zhao, 2003):

$$\frac{d}{dz}(b^2U) = 2\alpha bU, \tag{5-29}$$

$$\frac{d}{dz}(\rho_0 b^2 U^2) = 2\lambda^2 b^2 g(\rho_\infty - \rho_0), \tag{5-30}$$

$$\frac{d}{dz}\left[b^2U\left(\rho_{\infty,0} - \rho_0\right)\right] = 2b^2U\frac{d\rho_\infty}{dz}. \tag{5-31}$$

When density variation in the ambient is small relative to $\rho_{\infty,0}$, and if we assume an equal spread rate for momentum and mass, the above equations can be reduced further to the following form (Zhao, 2003; Baines, 1969) :

$$\frac{d}{dz}(b^2U) = 2\alpha bU, \tag{5-32}$$

$$\frac{d}{dz}(b^2U^2) = 2b^2g', \tag{5-33}$$

$$\frac{d}{dz}[b^2Ug'] = 2b^2U\frac{g}{\rho_{\infty,0}}\frac{d\rho_\infty}{dz}, \tag{5-34}$$

If we assume the ambient fluid is of uniform density, the plume centerline properties can be expressed in terms of powers of z and the buoyancy flux (Zhao, 2003):

$$b = \frac{6}{5}\alpha z, \tag{5-35}$$

$$U = \frac{5}{6\alpha}\left(\frac{18}{5\pi}\alpha B\right)^{1/3} z^{-1/3}, \tag{5-36}$$

$$g' = \frac{5}{3\pi}\left(\frac{5\pi}{18}\right)^{1/3} \alpha^{-4/3}B^{2/3}z^{-5/3}, \tag{5-37}$$

where z is the elevation from the source and the entrainment constant, α, is defined as the fraction of entrainment (inward) velocity to the centerline velocity U(Zhao, 2003). This is described mathematically

$$v_r = -\alpha|U| \tag{5-38}$$

where v_r is the radial velocity using a cylindrical polar coordinate system and the entrainment constant, α, is empirically determined (Zhao, 2003).

The volumetric flow rate of the buoyant jet is defined as,

$$Q_{bj} \triangleq 2\pi\int_0^\infty \bar{u}rdr \triangleq \pi Ub^2. \tag{5-39}$$

Replacing with the derived expressions for radius, b, and centerline velocity, U, yields

$$Q_{bj}(z) = \frac{6\pi}{5}\alpha^{4/3}\left(\frac{18}{5\pi}\right)^{1/3} B^{1/3}z^{5/3}. \tag{5-40}$$

The buoyancy flux, B is defined for a heat source by Equation (3.5). For an injected fluid, the buoyancy flux, B, is defined mathematically as

$$B \triangleq \int_{A_c} \vec{v}(\vec{r}) \cdot \vec{n}\frac{\rho(\vec{r}) - \rho_{ref}}{\rho_{ref}}\vec{g} \cdot \vec{d}A, \tag{5-41}$$

where $\vec{v}$ is the velocity vector, ρ_{ref} is the reference density, $\vec{g}$ is the gravity vector and $\vec{n}$ is a unity vector normal to the surface A_c, pointing in a direction for which the flux is considered positive.

$\rho_{ref} = \rho_a$ for a 1D stratified environment. Assuming an axisymmetric buoyant jet like the one shown in Fig. 5-2, the buoyancy flux (along the flow direction of the buoyant jet) can be written as

$$B = \int_0^b -\omega(r) g \frac{\rho_{jet}(r) - \rho_{amb}}{\rho_{amb}} 2\pi r \cdot dr. \tag{5-42}$$

5.2 STRATIFIED WETWELL MODEL

This wetwell model is capable of simulating thermal stratification due to a low steam mass injection rate. With a low mass flow rate, the model assumes that all the steam condenses within the pipe and the resulting plume can be approximated with a purely buoyant, heat-source driven model. It does not consider the momentum source due to steam injection and the resulting pool mixing effects.

Most systems-level nuclear safety analysis codes have no dedicated wetwell component and instead rely on generic volume components that use a well-mixed assumption where the entire water volume is lump together. There is currently a zero-D, nonstratified dedicated wetwell component in RELAP-7 (Zhao et al., 2014). It consists of a gas space and a water space, each of which has conservation of mass and energy governing equations. A diagram of the zero-D wetwell model can be seen in Fig. 5-3. There are closure relations used to compute water level, gas density, and water density. Pressure and temperature of the gas and water are calculated from EOS relationships. Similar to the majority of systems-level wetwell models, the entire water pool is assumed to be well-mixed. Figure 5-3 shows the schematic of the simplified model.

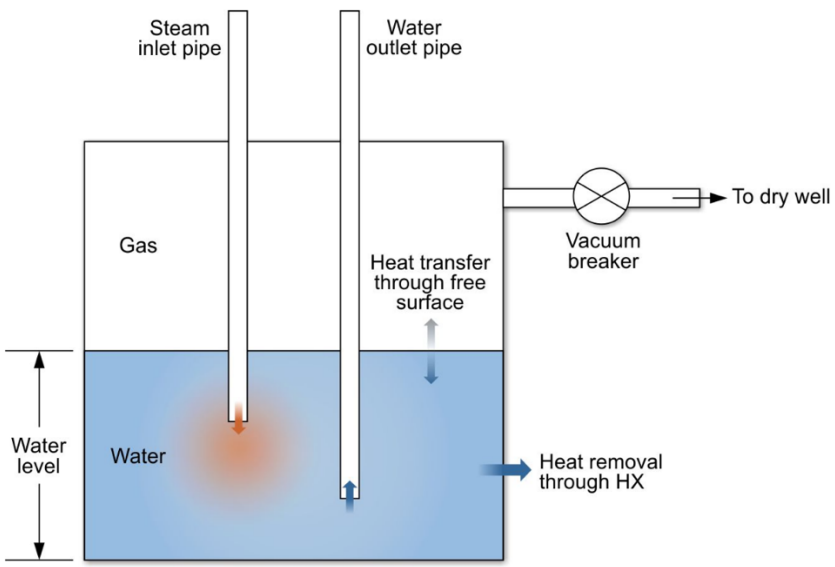

Figure 5-3. RELAP-7's simplified wetwell model diagram (Berry et al., 2016).

Major assumptions include:

1. the hot and cold water zones are separate; within each zone the pool is well mixed,
2. the kinetic energy in both spaces is ignored, therefore the water space pressure follows a hydrostatic distribution,
3. no mass transfer between water and gas space,
4. the geometry of the wetwell is rectangular, and
5. no steam venting from drywell to the suppression pool.

The wetwell model developed with these assumptions is adequate to simulate slow transients such as extended SBO transients. However, the current model is not suitable for more rapidly progressing scenarios in which pool mixing would be significant, e.g. Loss of Coolant Accidents (LOCAs). With these assumptions, mass and energy balance equations apply for gas, hot water, and cold water spaces. The mass conservation equation for the gas space is

$$\frac{dm_g}{dt} = -\dot{m}_v, \tag{5-43}$$

where m_g is the gas mass and $\dot{m}_v$ is the venting mass flow rate to the drywell which is obtained from the connected pipe controlled by the vacuum breaker.

The energy conservation equation for the gas space is

$$\frac{d(me)_g}{dt} = A_c \alpha_{hw,g}\left(T_{hw} - T_g\right) - \dot{m}_v H_v, \tag{5-44}$$

where $(me)_g$ is the total internal energy (also total energy since kinetic energy is assumed to be 0) for the gas space, A_c the average cross section area for the wetwell, $\alpha_{hw,g}$ the effective heat transfer coefficient between the hot water and gas as given by user input, T_{hw} and T_g are temperatures for hot water and gas, respectively. H_v is the total enthalpy from the connected upstream boundary condition. The small pressure work due to the change of the volume is ignored since the change of water volume is slow and very small compared to its large volume.

The mass conservation equation for the hot water space is

$$\frac{dm_{hw}}{dt} = \dot{m}_{plume}, \tag{5-45}$$

where m_{hw} is the total mass of hot water and $\dot{m}_{plume}$ is the thermal plume mass flow rate. The model for $\dot{m}_{plume}$comes from Morton (Morton, 1959).

The mass conservation equation for the cold water space is

$$\frac{dm_{cw}}{dt} = -\dot{m}_{out} - \dot{m}_{entrained}, \tag{5-46}$$

where m_{cw} is the total mass of cold water, $\dot{m}_{entrained}$ is the mass flow rate of ambient water entrained by the plume as it rises (calculated as the difference between $\dot{m}_{plume}$ and $\dot{m}_{in}$),

$$\dot{m}_{entrained} = \dot{m}_{plume} - \dot{m}_{in}, \tag{5-47}$$

$\dot{m}_{in}$ in is the inlet steam mass flow rate and obtained from the connected steam pipe boundary condition, and $\dot{m}_{out}$ is the outlet water mass flow rate

$$\dot{m}_{out} = (\rho u A)_{out}, \tag{5-48}$$

where $(\rho u A)_{out}$ is the flow model conserved variable for momentum which is coupled from the connected water pipe.

The total energy conservation equation for hot water space is

$$\frac{d(me)_{hw}}{dt} = \dot{m}_{entrained} H_{cw} + \dot{m}_{in}(H_{in} - H_{cw}) - A_c \alpha_{hw,g}\left(T_{hw} - T_g\right), \tag{5-49}$$

where $(me)_{hw}$ is the total internal energy for the hot water space, H_{in} is the total enthalpy coupled from the connecting steam pipe, and $\dot{m}_{in}(H_{in} - H_{cw})$ represents the heating rate due to steam condensation. The gravitational potential energy difference from flow between the hot and cold water volumes is small relative to the other energy terms and has been neglected.

The total energy conservation equation for cold water space is

$$\frac{d(me)_{cw}}{dt} = -\dot{m}_{out} H_{out} - \dot{m}_{entrained} H_{cw} - \dot{q}_{hxr}. \tag{5-50}$$

$\dot{q}_{hxr}$ is the active heat removal rate from the immersed heat exchanger and total enthalpy for water being pumped out of the wetwell is defined as

$$H_{out} = \left(e_{cw} + \frac{p_{cw}}{\rho_{cw}(p_{cw}, T_{cw})}\right) + \frac{1}{2} u_{out}^2. \tag{5-51}$$

u_{out} is the exit speed obtained from coupled water pipe end. For inflow condition, H_{out} will be coupled from the pipe end.

Both of the water energy conservation equations are solved for the water temperature as their primary variable. This is possible because the water energies (e_{cw} and e_{hw}) are calculated using an equation of state relationship as a function of pressure and temperature.

Reference pressure in the hot water space is defined at the interface between hot and cold water,

$$p_{hw} = p_g + (L_w - L_I)\rho_{hw} g, \tag{5-52}$$

where p_{hw} is the reference hot water pressure and p_g the gas pressure. Reference pressure in the cold water space is defined at the bottom elevation of the pool,

$$p_{cw} = p_g + (L_w - L_I)\rho_{hw}g + L_I\rho_{cw}g. \tag{5-53}$$

Hot and cold water interface level L_i, measured from pool bottom, is calculated using a relationship between hot water mass, density, and volume.

$$m_{cw} = L_I A_c \rho_{cw} \tag{5-54}$$

Total water level L_w, measured from pool bottom, is calculated using a relationship between hot water mass, density, and volume.

$$m_{hw} = (L_w - L_I)A_c\rho_{hw} \tag{5-55}$$

Hot and cold water density is calculated using an equation of state relationship.

In the code implementation of the wetwell model, m_g, $(me)_g$, m_{hw}, m_{cw}, T_{hw}, T_{cw}, p_{hw}, p_{cw}, L_i, and L_w are designated as the primary variables to be solve for, with corresponding Equations (4.1), (4.2), (4.3), (4.4), (4.7), (4.8), (4.10), (4.11), (4.12), and (4.13). Another set of auxiliary variables is defined to close the system, which include gas density ρ_g, hot/cold water densities ρ_{hw}/ρ_{cw}, and hot/cold water energies e_{hw}/e_{cw}. Gas density is calculated according to

$$\rho_g = \frac{m_g}{A_c(L_t - L_w)}, \tag{5-56}$$

where L_t is the total effective height of the wetwell. The hot and cold water densities and energies are calculated using an equation of state fluid property function of pressure and temperature, $f(p, T)$.

The model for plume entrainment comes from (Morton, 1959) and can be seen in Section 3.1.3.2.

In this current iteration of the stratified wetwell model, it is assumed that the plume of hot water is due only to the buoyancy effect. The driving energy force of the plume comes from the steam injection into the wetwell and its assumed that all the energy from the condensed steam goes into the plume. The heat flux into the plume is

$$\dot{q} = \dot{m}_{in}(H_{in} - H_{cw}). \tag{5-57}$$

This heating rate, $\dot{q}$, drives the buoyancy flux, B which is defined for a heat source by Equation (3.5).

Using Peterson's (Peterson, 1994) definition for volumetric flow rate carried by a buoyant jet

$$Q_{plume} = k_\mu B^{1/3}(L_i - z_{in})^{5/3}, \tag{5-58}$$

where $k_\mu$is Taylor's entrainment constant. The mass flow rate of the plume is calculated as shown Equation (4.17).

$$\dot{m}_{plume} = \dot{Q}_{plume} * \rho_{cw} \tag{5-59}$$

Initial conditions for the primary variables are calculated according to the initial water level $L_w(0)$, gas pressure $p_g(0)$, and gas temperature $T_g(0)$.

Boundary conditions for three connecting pipes are set similarly as for the reverse pump boundary conditions. For example, the inlet steam pipe needs one boundary condition p_{in}

$$p_{in} + \frac{1}{2}(\rho u^2)_{in} = p_i + K_{in}\frac{1}{2}(\rho u^2)_{in} \tag{5-60}$$

where K_{in} is the form loss coefficient and p_i is the water pressure at the elevation of inlet steam pipe end,

$$p_i = p_{hw} - z_i \rho_{cw} g. \tag{5-61}$$

The other two pipe boundary conditions are set in a similar manner.

5.2.1 POOL HEATER EXPERIMENT

The stratified wetwell model has been benchmarked against a simple analytical solution of a pool heater experiment. Figure 5-4 shows a diagram of the experimental setup. An analytical solution to the location of the first front of the descending hot water layer is detailed in (Christensen and Peterson, 2001).

"The analytical test case matches an earlier experiment (Peterson, 1994) that submerged an electrical heater into a cylindrical tank. The heat produces an upward directed vertical plume which penetrates all the way to the water surface at the top of the cylindrical tank. After the plume reaches the water surface it spreads out and forms a layer which is warmer than the fluid below. The transient evolution of the vertical temperature distribution was measured using a number of thermo-couples" (Christensen and Peterson, 2001).

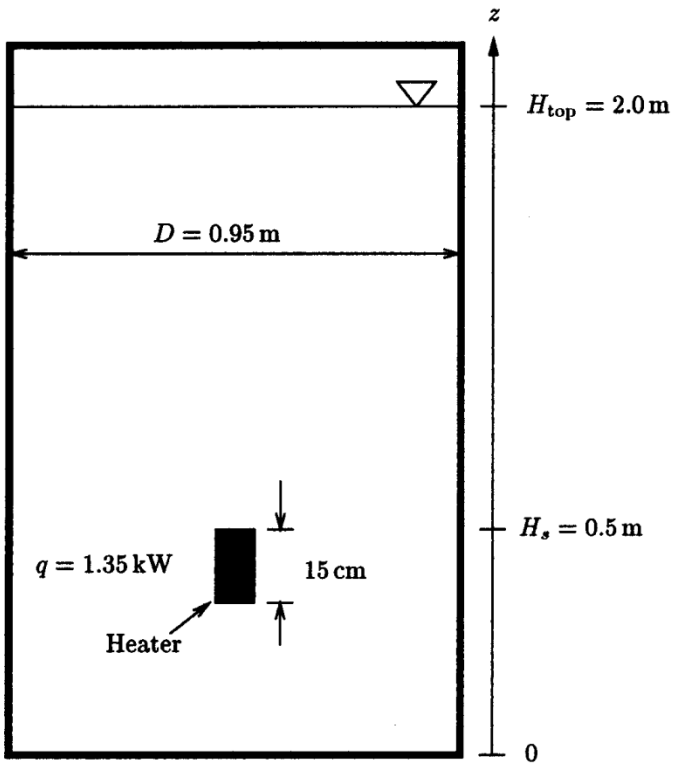

Figure 5-4. Thermal stratification experiment in cylindrical water tank (Christensen and Peterson, 2001).

In the experiment

$$A_c = \frac{\pi}{4} D^2 = 0.709\ m^2 \tag{5-62}$$

, and

$$H_{eff} = H_{top} - H_s = 1.5\ m, \tag{5-63}$$

where A_c is the cross-sectional area of the tank and H_{eff} is the effective height defined as the difference between the plume discharge location (pool surface) and the source elevation (top of heater). The simulation assumes that the heater is a point source when in reality it has a length.

The buoyancy flux for a heat source was calculated based on the driving heat flux of 1.35 kW and properties of water at 20°C.

$$B = \frac{g\beta q}{\rho_{av} c_p} = 6.7 \times 10^{-7}\ [m^4 s^{-3}] \tag{5-64}$$

These heat and buoyancy flux values were hardcoded in the stratified wetwell model (only for this simulation) in order to accurately drive the plume heat and mass transfer.

The buoyant thermal plume transports hot water from the heat source elevation up to the top of the pool; this creates a hot upper layer of water which grows and moves downward. The interface between the growing hot water section and the shrinking cold water section can be referred to as the first front. The position of the first front, z_{k_0}, is defined as the elevation relative to the source where heating first occurs The plume is created by the heater and is purely buoyant, thus an analytical solution for the location of the first front can be written as (Baines, 1969)

$$z_{k_0} = H_{eff}\left[1 + \frac{1}{5}\left(\frac{18}{5}\right)^{1/3}\tau\right]^{-3/2}, \tag{5-65}$$

where τ is a dimensionless time parameter defined as

$$\tau \triangleq 4\pi^{2/3}\alpha^{4/3}H_{eff}^{2/3}A_c^{-1}B^{1/3}t. \tag{5-66}$$

Using the data for the given experimental setup results in an expression for first front as a function of time.

$$z_{k_0}(t) = 1.5\left[1 + 0.30652\frac{t}{189.977\ s}\right]^{-3/2} \tag{5-67}$$

Figure 5-5 shows a comparison of the first front position for the simulation performed with the new wetwell model in RELAP-7 and analytical solution. There is visually no difference between the two solutions, and thus the difference, or error of z_{k_0} has been depicted in Fig. 5-6.

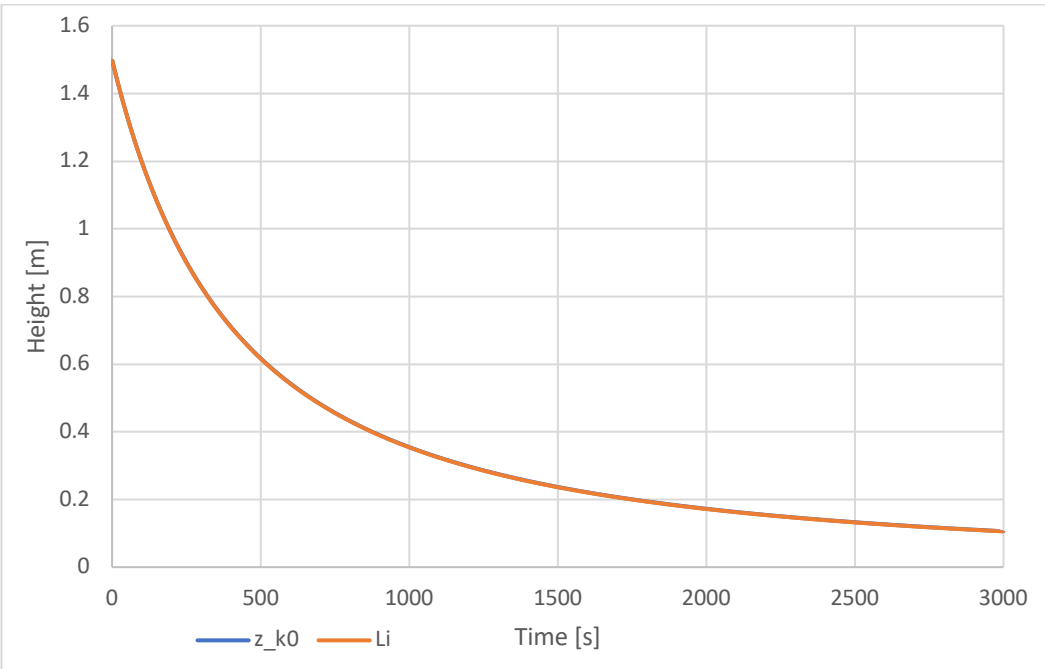

Figure 5-5. Comparison of the numerically and analytically calculated location of the first front.

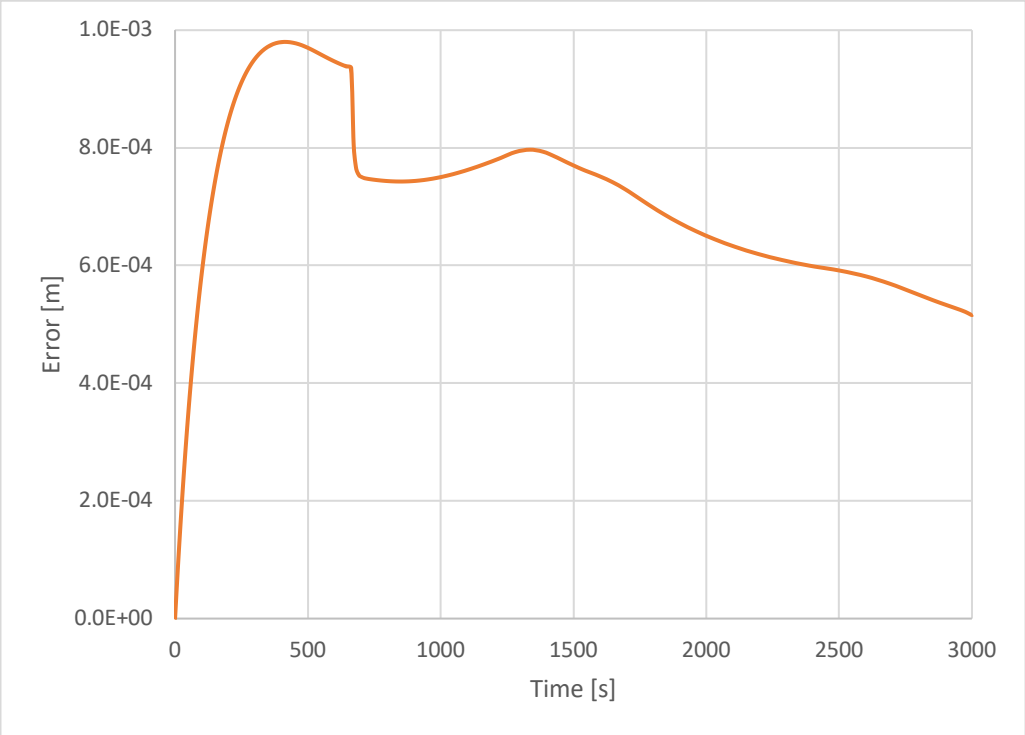

Figure 5-6. Error in the numerically calculated first front position.

5.2.2 POOLEX STB-20 EXPERIMENT

The Condensation POOL EXperiments (POOLEX) is a research project started in 2003 by the SAfety of Nuclear Power Plants - FInnish National Research Programme (SAFIR). The main objective of the POOLEX project is to increase the understanding of phenomena, such as stratification and mixing, in the condensation pool during steam injection. The specific STB-20 experiment was chosen as a benchmark for the stratified wetwell model for two main reasons: (1) the test rig steam injection pipe is a downward facing, open-ended, vertical pipe (2) the steam injection rate was kept low enough to make sure steam condensed within the injection pipe, thus ensuring negligible mixing effects.

The POOLEX test rig was designed as a scaled down version of the Olkiluoto 1 and 2 BWRs. Figure 5-7 shows a diagram of the POOLEX test rig. Table 5-1 shows a comparison of relevant scaling parameters between the POOLEX test rig and the Olkiluoto BWRs.

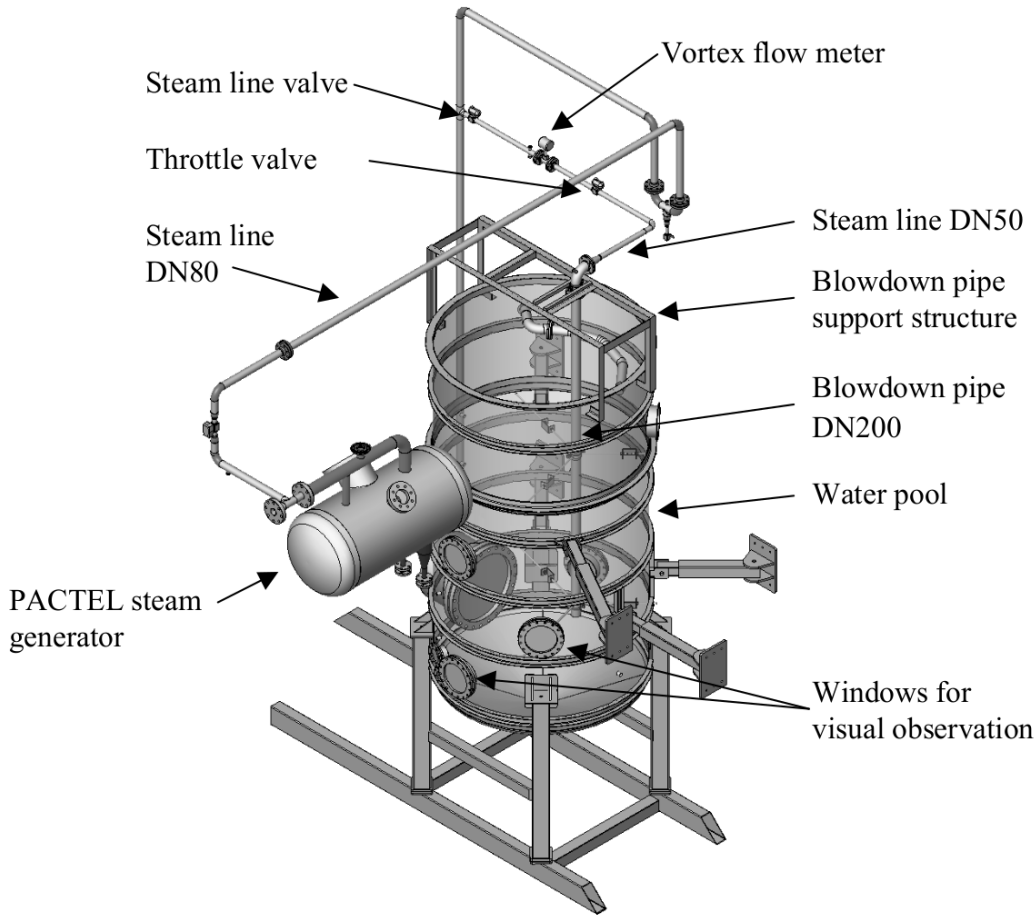

Figure 5-7. POOLEX test rig (Laine and Puustinen, 2005).

Table 5-1. Test rig vs. Olkiluoto 1 and 2 BWRs (Laine and Puustinen, 2005).

	Test rig	Olkiluoto 1 and 2
Number of blowdown pipes	1	16
Inner diameter of blowdown pipes [mm]	214.1	600
Pool cross-sectional area [m^2]	4.5	287.5
Water level in the pool [m]	2.95	9.5
Pipes submerged [m]	1.81	6.5
Pool water volume [m^3]	12	2700
A_{pipes}/A_{pool}x100%	0.8	1.6

The total duration of the POOLEX STB-20 experiment was approximately 52 hours which included a heat up phase due to steam injection and a cool down phase with no steam injection. Only the heat up phase was simulated. The pool was at a uniform temperature of 30 °C before the steam blowdown was initiated. The pool water was heated with steam injection during the first four hours of the experiment. The steam flow rate was initiated at 55 g/s and was slowly reduced to 25 g/s "during the experiment to make sure that steam condenses inside the blowdown pipe and the steam-water interphase remains close to the blowdown pipe outlet"

(List, 1982). Because the steam condensed within the blowdown pipe, there was little pool mixing and there was strong thermal stratification of the pool water during the heating phase. After four hours of steam injection, the upper part of the pool reached a temperature of 67 °C while "the temperature below the blowdown pipe outlet level stayed at the initial value of 30 °C" (Laine and Puustinen, 2005).

Figure 5-8 shows the vertical temperature distribution in the test rig during the heat up phase. A diagram of the vertical thermocouple placement in the test rig can be seen in Fig. 5-9.

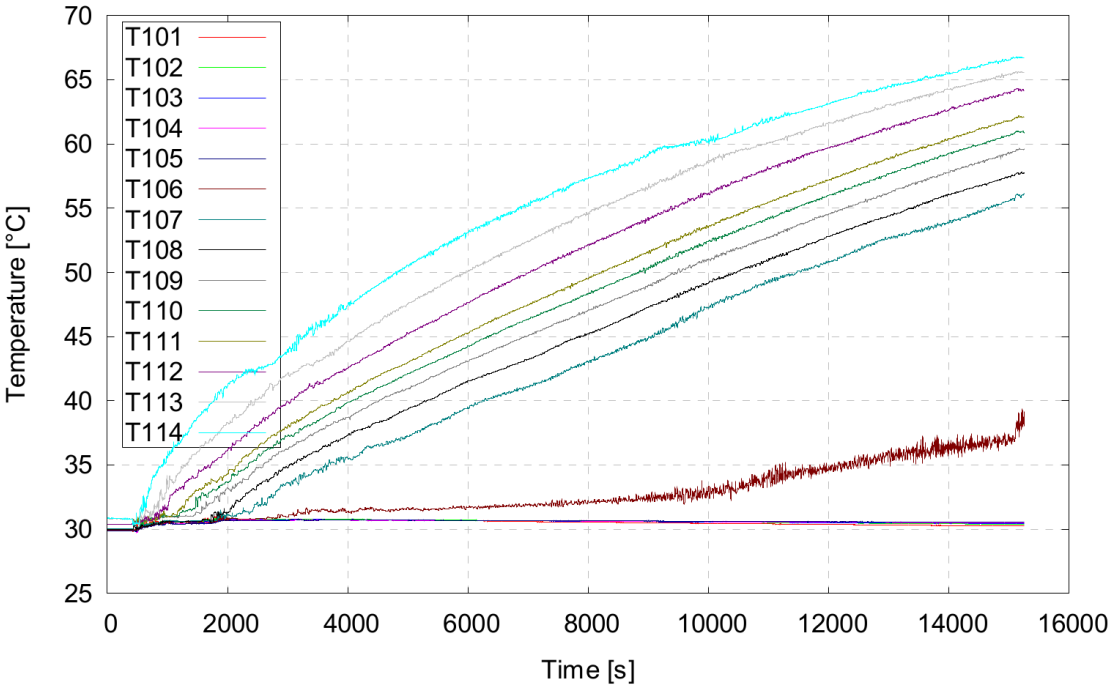

Figure 5-8. Measured vertical temperature distribution in the pool in STB-20 during the heating phase.

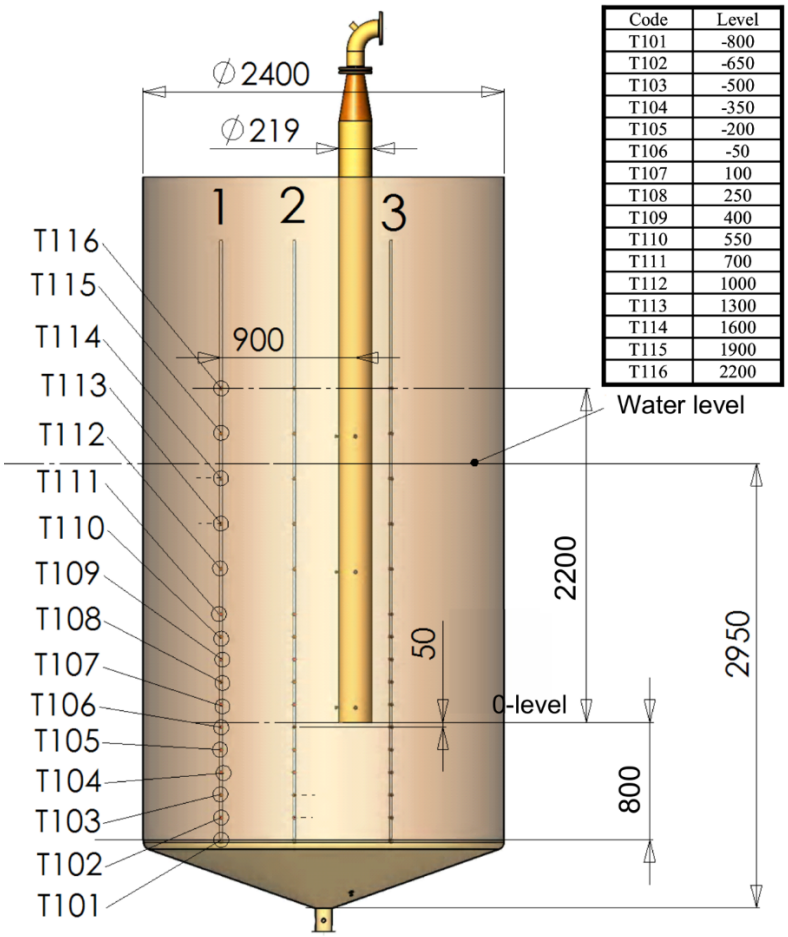

Figure 5-9. POOLEX thermocouple placement (Laine and Puustinen, 2005).

The stratified wetwell model produced simulation results which agree reasonably well with the experimental data. Figure 5-10 shows the simulation vertical temperature profile results for various snapshots in time. As time increases, the hot water section can be clearly seen heating and growing downwards as the cold water section shrinks smaller while maintaining the same temperature.

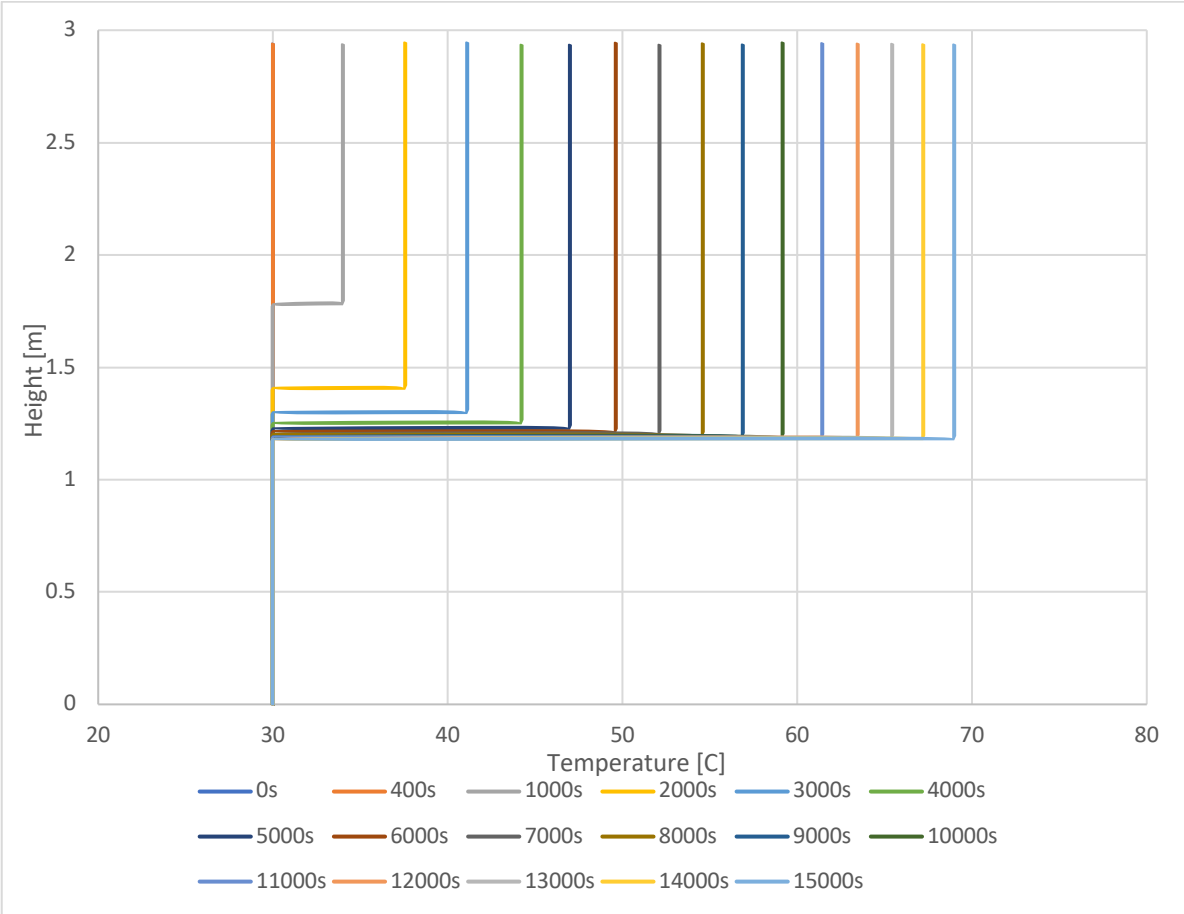

Figure 5-10. Simulation vertical temperature distributions at various times.

The wetwell model conserves mass and energy, but it only has two water zones so it cannot capture the same stratification detail as 14 vertical thermocouples. A pool temperature versus time comparison of the simulation and experimental results is shown in Fig. 5-11. The simulated hot water temperature is close to the temperature of the upper, hot water experimental data; the simulated cold water temperature is close to the temperature of the water below the experiment steam injection pipe.

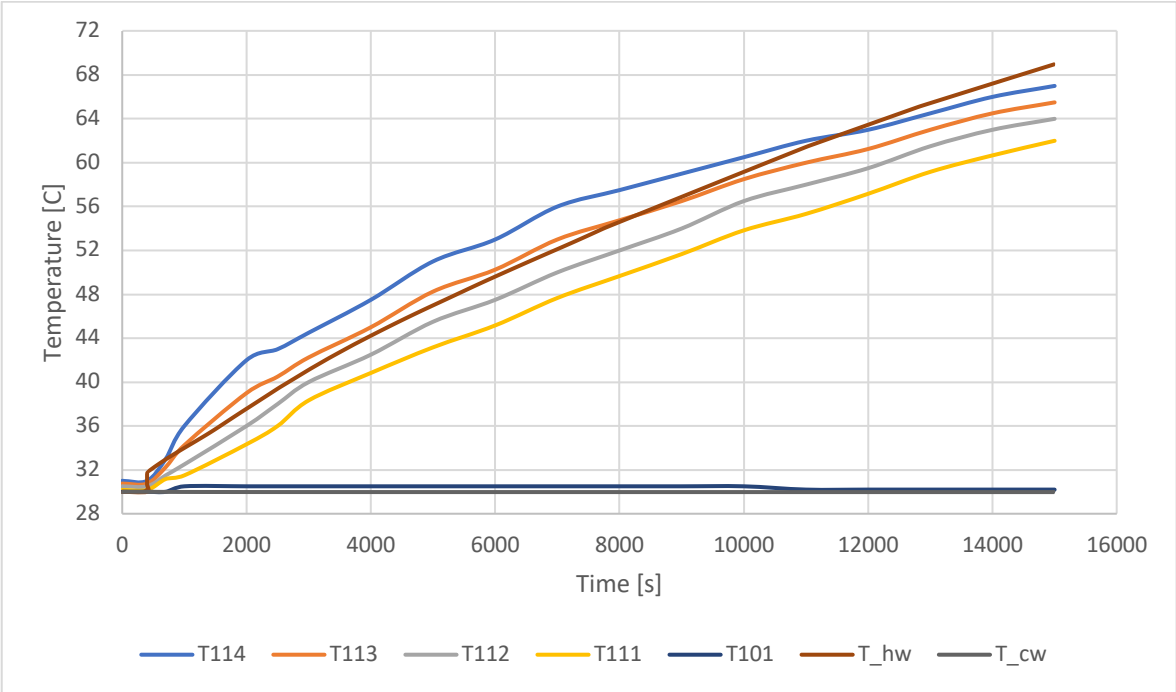

Figure 5-11. Pool temperature versus time comparison of the simulation and experimental results.

Towards the end of the test, the simulated hot water temperature exceeds the measured hot water in the experiment. This discrepancy comes from the fact that the simulation does not take into account heat losses through the test rig or from the exposed pool surface.

5.3 SUMMARY

This section presents the development and implementation of a novel two-zone stratified wetwell model. The suppression pool temperature distribution has a very large impact on both RPV and containment pressure. Thus, the project novel contributions come mainly from an improved, systems-level wetwell model which can capture buoyancy-induced thermal stratification effects due to steam injection and condensation. A two-zone stratified wetwell model has been implemented in RELAP-7. This wetwell model is capable of simulating thermal stratification due to a low steam mass injection rate.

6. CONCLUSIONS

In this report, we have summarized our development work on the two-phase nozzle model, physical-based RCIC model and two-zone stratified wetwell model, and the implementation in the system-level analysis codes.

The 1D two-phase four-fluid model employed in the present work considers four separate fluid fields. The vapor, liquid film and entrained droplet fields are calculated separately, and the condensed droplet field is merged into the vapor field if the condensation occurs. The flow governing equations, critical flow model, nucleation condensation model, flashing model and numerical techniques were presented and discussed in detail. The mechanistic nozzle model developed in this report has provided a much-needed capability for modeling and simulation of complex two-phase flow processes and phenomena through a convergent-divergent nozzle, which is largely missing in current thermal-hydraulic system analysis codes and CFD software. The work is of significant importance for the understanding and analysis of dynamic responses of the RCIC system under BDBA conditions, in which Terry turbine nozzle flow plays a vital role.

The accuracy of the nozzle model was evaluated by comparing with the available test data and the CFD simulation results. The presented simplified four-fluid nozzle model has the capability to model and predict the transonic steam flow with condensation in the nozzle for a wide range of inlet pressure conditions. The numerical results of the nozzle model show reasonable accuracy compared with the Moore nozzle test and Barschdorff nozzle test, which are both low pressure nozzle steam flow tests. The applicability of the nucleation condensation model, three-fluid critical model, and solution method have been verified. The results of the nozzle model for higher pressure condensing steam flow of the Kneass nozzle tests also show good agreement with the test data and CFD results.

A mechanistic RCIC model was developed and implemented in TARCE to demonstrate its capabilities. The governing equation is based on a control volume formulation of the angular momentum balance approach. The TRACE model in this report has a reasonably detailed nodalization of RPV, and all of the major flow paths and system components including SRVs and containment components. The dynamic response of the RCIC system during a postulated SBO accident was simulated. The short-term SBO simulations were also performed for two cladding materials: Zircaloy and FeCrAl. Analyses are presented that illustrate the impact of the FeCrAl cladding material on the fuel performance under BDBA conditions.

In addition, a novel two-zone stratified wetwell model was developed and implemented in system-level analysis code. The suppression pool temperature distribution has a very large impact on both RPV and containment pressure. Thus, the project novel contributions come mainly from an improved, systems-level wetwell model which can capture buoyancy-induced thermal stratification effects due to steam injection and condensation. A two-zone stratified

wetwell model has been implemented in RELAP-7. This wetwell model is capable of simulating thermal stratification due to a low steam mass injection rate.

REFERENCES

Ansys Inc., 2015. ANSYS FLUENT User's Guide. Version 16.2, July, Canonsburg, PA, http://www.ansys.com.

Avramova M.N., and Salko R.K., 2016. CTF theory manual. No. ORNL/TM--2016/430. Oak Ridge National Laboratory, Oak Ridge, TN, United States.

Baines W.D., 1969. Turbulent buoyant convection from a source in a confined region. Journal of Fluid Mechanics, 37(1), 51-80.

Barschdorff D., Dunning W.J., Wegener P., and Wu B., 1972. Homogeneous Nucleation in Steam Nozzle Condensation. Nat. Phys. Sci., 240: 166-167.

Beeny B., 2017. Computational multiphase fluid dynamics analyses and systems-level model development for a reactor core isolation cooling system terry turbine. Office of Graduate and Professional Studies of Texas A&M University.

Berry R.A., Peterson J.W., Zhang H., Martineau R. C., Zhao H., Zou L., ... and Hansel J., 2018. Relap-7 theory manual (No. INL/EXT-14-31366-Rev003). Idaho National Lab.(INL), Idaho Falls, ID (United States).

Cardoni J., Ross K., Beeny B., and Osborn D., 2018. Terry turbine expanded operating band: Sandia National Laboratories Terry turbine analytical efforts. Sandia National Lab, Albuquerque, NM, United States.

Chen R., Zhang P., Ma P., Tan B., Wang Z., Zhang D., Tian W., Qiu S., and Su G.H., 2020. Experimental investigation of steam-air condensation on containment vessel. Annals of Nuclear Energy, 136: 107030.

Chen R., Zhang P., Tan B., Ma P., Wang Z., Zhang D., Tian W., Qiu S., and Su G.H., 2019. Steam condensation on a downward-facing plate in presence of air. Annals of Nuclear Energy, 132: 451-460.

Cheng L., Ribatski G., and Thome J.R., 2008. Two-phase flow patterns and flow-pattern maps: fundamentals and applications. Applied Mechanics Reviews, 61(5): 050802.

Christensen J. and Peterson F., 2001. A one-dimensional Lagrangian model for large-volume mixing. Nuclear Engineering and Design, 204(1-3), 299-320.

Cousins L.B., 1965. Liquid Mass Transfer in Annular Two-Phase Flow. In Symposium on Two-Phase Flow, 2: 401-430.

French L.G., 1907. Steam Turbines: Practice, and Theory. Hill Publishing, New York, NY, United States.

Garajau F.S., Guerra M.S.L., Maia B.T., and Cetlin P.R., 2019. Effects of post combustion temperature on the wear of the supersonic nozzles in BOF lance tip. Engineering Failure Analysis, 96: 175-185.

Gebhart, B., Jaluria, Y., Mahajan, R. L., & Sammakia, B., 1988. Buoyancy-induced flows and transport. Washington, D.C.: Hemisphere Pub. Corp.

Geng L., Liu H., and Wei X., 2019. CFD analysis of the flashing flow characteristics of subcritical refrigerant R134a through converging-diverging nozzles. International Journal of Thermal Sciences, 137: 438-445.

Halama J., and Fort J., 2012. Numerical simulation of steam condensation in a nozzle. EPJ Web of Conferences, 25: 01020. EDP Sciences.

Henry R.E., and Fauske H.K., 1971. The Two-Phase Critical Flow of One-Component Mixtures in Nozzles, Orifices, and Short Tubes. Transactions of ASME, Journal of Heat Transfer, 93: 179-187.

Hunt G.R. and van den Bremer T.S., 2010. Classical plume theory: 1937-2010 and beyond. IMA Journal of Applied Mathematics, vol. 76, pp. 424-448.

Kataoka I., Ishii M., and Mishima K., 1983. Generation and size distribution of droplet in annular two-phase flow. Journal of Fluids Engineering, 105(2): 230-238.

Kim C.H., Park, J.H., Kim, D.I., and Baek, J.H., 2017. Numerical analysis of non-equilibrium steam condensing flows in various Laval nozzles and cascades. Engineering Applications of Computational Fluid Mechanics, 11(1): 172-183.

Kirkland K.V., Ross K., Beeny B., Luthman N., Strater Z., 2017. Multi-phase model development to assess RCIC system capabilities under severe accident conditions. Texas A&M Engineering Experiment Station, College Station, TX, United States.

Kronig R., and Brink J., 1950. On the Theory of Extraction From Falling Droplets. Applied Scientific Research, A2: 142-154.

Kuhn S.Z., Schrock V.E., and Peterson P.F., 1994. Final Report on U. C. Berkeley Single Tube Condensation Studies. University of California, Berkeley, United States.

Laine J. and Puustinen M., 2005. Thermal stratification experiments with the condensation pool test rig. Lappeenranta.

Law W.P., and Gimbun J., 2019. Thermal performance enhancement of non-premixed syngas combustion in a partial combustion unit by winged nozzle: Experimental and CFD study. Energy, 182:148-158.

Lax P., and Wendroff B., 1960. Systems of conservation laws. Communications on Pure and Applied mathematics, 13(2): 217-237.

Li H., Kudinov P., and Villanueva W., 2011. Development and Validation of Effective Models for Simulation of Stratification and Mixing Phenomena in a Pool of Water. No. NKS-248, Nordisk Kernesikkerhedsforskning.

Li H., Villanueva W., and Kudinov P., 2014. Approach and development of effective models for simulation of thermal stratification and mixing induced by steam injection into a large pool of water. Science and Technology of Nuclear Installations, vol. 2014.

List E.J., 1982. Mechanics of Turbulent Buoyant Jets and Plumes. Turbulent Buoyant Jets and Plumes, New York: Pergamon Press

McDonald J.E., 1962. Homogeneous Nucleation of Vapor Condensation. I. Thermodynamic Aspects. American Journal of Physics 30, 870.

McDonald J.E., 1963. Homogeneous Nucleation of Vapor Condensation. II. Kinetic Aspects. American Journal of Physics 31, 31.

Mesina G.L., 2016. A history of RELAP computer codes. Nuclear Science and Engineering, 182(1): v-ix.

Moore M.J., and Sieverding C.H., 1976. Two-phase steam flow in turbines and separators: theory, instrumentation, engineering. Hemisphere publishing, London, United Kingdom.

Moore M.J., Walters P.T., Crane R.I., and Davidson B.J., 1973. Predicting the fog-drop size in wet-steam turbines. Wet steam, 4: 101-109.

Morton B.R., 1959. Forced plumes. Journal of Fluid Mechanics, vol. 5, no. 1, pp. 151-163.

Nuclear Energy Agency, 2015. NEA Benchmark Study of the Accident at the Fukushima Daiichi Nuclear Power Station (BSAF) Project. https://www.oecdnea.org/jointproj/bsaf.html.

Okawa R. and Furuya M., 2019. TRACE code demonstration of thermal stratification in BWR suppression pool. Nuclear Engineering and Design, 355 (2019): 110357.

Ott L.J., Robb K.R., & Wang D., 2014. Preliminary assessment of accident-tolerant fuels on LWR performance during normal operation and under DB and BDB accident conditions. Journal of Nuclear Materials, 448(1-3), 520-533.

Paleev I.I., and Filippovich B.A., 1966. Phenomena of Liquid Transfer in Two-Phase Dispersed Annular Flow. International Journal of Heat and Mass Transfer, 9:1089-1093.

Patterson B.J., 1979. Mark I Containment Program, Monticello T-Quencher Thermal Mixing Test, Final Report.

Pandey A., 2014. Numerical Modelling of Non-Equilibrium Condensing Steam Flows. Delft University of Technology, Delft, Netherlands.

Pellegrini M., Araneo L., Ninokata H., Ricotti M., Naitoh M., and Achilli A., 2016. Suppression pool testing at the SIET laboratory: experimental investigation of critical phenomena expected in the Fukushima Daiichi suppression chamber. Journal of Nuclear Science and Technology, vol. 53, no. 5, pp. 614-629.

Peterson P.F., 1994. Scaling and analysis of mixing in large stratified volumes. International Journal of Heat and Mass Transfer, vol. 37, no. SUPPL. 1, pp. 97-106.

Ransom V.H., Trapp J., and Wagner R., 2001. RELAP5/MOD3. 3 code manual Volume IV: models and correlations. Information Systems Laboratories, IR, Maryland Idaho Falls, Idaho, United States.

Ross K., Cardoni J., Osborn D., Gauntt R., Wilson C., Morrow C., 2015. Modeling of the Reactor Core Isolation Cooling Response to Beyond Design Basis Operations–Phase 1. SAND2015-10662, Sandia National Laboratories, Albuquerque, NM, United States.

Ruangtrakoon N., Thongtip T., Aphornratana S., Sriveerakul T., 2013. CFD simulation on the effect of primary nozzle geometries for a steam ejector in refrigeration cycle. International Journal of Thermal Sciences, 63: 133-145.

Sokolowski L., and Kozlowski T., 2010. Assessment of two-phase critical models performance in RELAP5 and TRACE against Marviken critical flow test. Transactions of the American Nuclear Society, 102: 655-657.

Solom M.A., 2016. Experimental Study on Suppression Chamber Thermal-Hydraulic Behavior for Long-Term Reactor Core Isolation Cooling System Operation. PhD Dissertation.

Song D., Erkan N., Jo B., and Okamoto K., 2014. Dimensional analysis of thermal stratification in a suppression pool. International Journal of Multiphase Flow, vol. 66, pp. 92-100.

Spore J.W., Elson J.S., Jolly-Woodruff S.J., Knight T.D., Lin J.C., Nelson R.A., Pasamehmetoglu K.O., Steinke R.G., Unal C., Mahaffy J.H., and Murray C., 2000. TRAC-M/Fortran 90 (Version 3.0) Theory Manual. Los Alamos National Lab., Los Alamos, NW, United States.

Starzmann J., Hughes F.R., Schuster S., et al., 2018. Results of the international wet steam modeling project. Proceedings of the Institution of Mechanical Engineers, Part A: Journal of Power and Energy, 232(5): 550-570.

Sushma L., Deepik A.U., Sunnam S.K., and Madhavi M., 2016. CFD Investigation for different nozzle jets. International Conference on Advancements in Aeromechanical Materials for Manufacturing (ICAAMM-2016).

Trapp J.A., and Ransom V.H., 1982. A choked-flow calculation criterion for nonhomogeneous, nonequilibrium, two-phase flows. International Journal of Multiphase Flow, 8(6): 669-681.

U.S. NRC, 2010. TRACE V5. 0 Theory Manual, Field Equations, Solution Methods, and Physical Models. United States Nucl. Regul. Comm.

Wagner W., and Kretzschmar H.J., 2008. IAPWS industrial formulation 1997 for the thermodynamic properties of water and steam. International Steam Tables: Properties of Water and Steam Based on the Industrial Formulation IAPWS-IF97: 7-150.

Wang D., Mohaffy J.H., and, Staudenmeier J., Thurston C.G., 2013. Implementation and Assessment of High-Resolution Numerical Methods in TRACE. Nuclear Engineering and Design, 263, 327-341.

Wang D., Mohaffy J.H., and Staudenmeier J., 2015. Solving Two-Phase Flow Transport Equations Using the Lax-Wendroff Scheme. Trans. AM. Nucl. Soc., 112.

Wróblewski W., Dykas S., and Gepert A., 2009. Steam condensing flow modeling in turbine channels. International Journal of Multiphase Flow, 35(6): 498-506.

Wurtz J., 1978. An Experimental and Theoretical Investigation of Annular Steam-Water flow in Tubes and Annuli at 30 to 90 Bar. Technical Report 372, RISO National Laboratory, Denmark.

Yang Y., Walther J.H., Yan Y., and Wen C., 2017. CFD modeling of condensation process of water vapor in supersonic flows. Applied Thermal Engineering, 115: 1357-1362.

Young J.B., 1992. Two-Dimensional Nonequilibrium, Wet-Steam Calculations for Nozzles and Turbine Cascades. Journal of Turbomachinery, 114: 569-579.

Yousefi Rad E., and Mahpeykar M.R., 2017. A novel hybrid approach for numerical modeling of the nucleating flow in Laval nozzle and transonic steam turbine blades. Energies, 10(9): 1285.

Zhao H., 2003. Computation of Mixing in Large Stably Stratified Enclosures. PhD Dissertation.

Zhao H., Zou L., and Zhang H., 2014. Simulation of thermal stratification in BWR suppression pools with one dimensional modeling method. Annals of Nuclear Energy, vol. 63, pp. 533-540.

Zhao H., Zou L., Zhang H., Andrs D., and Martineau R., 2014. Developing Fully Coupled Dynamical Reactor Core Isolation System Models in RELAP-7 for Extended Station Black-Out Analysis (No. INL/CON-13-29971). Idaho National Laboratory (INL).

Zhao H., Zhang H., Zou L., O'Brien J., 2016. Single phase analytical models for Terry turbine nozzle. Idaho National Lab., Idaho Falls, ID, United States.

Zhao H., and O'Brien J, 2017. Preliminary Two-Phase Terry Turbine Nozzle Models for RCIC Off-Design Operation Conditions. Idaho National Lab., Idaho Falls, ID, United States.

Zori L., and Kelecy F., 2005. Wet steam flow modeling in a general CFD flow solver. 35th AIAA fluid dynamics conference and exhibit.

APPENDICES

A. PROGRAM STRUCTURE OF NOZZLE TWO-PHASE MODEL

The 1D nozzle code is developed to solve the two-phase critical flow through the convergent-divergent nozzle. The program structure about subroutines is shown in Fig. A-1 and the detailed annotations about the code are added in the source code. The function of each subroutine in the nozzle code is described as follows:

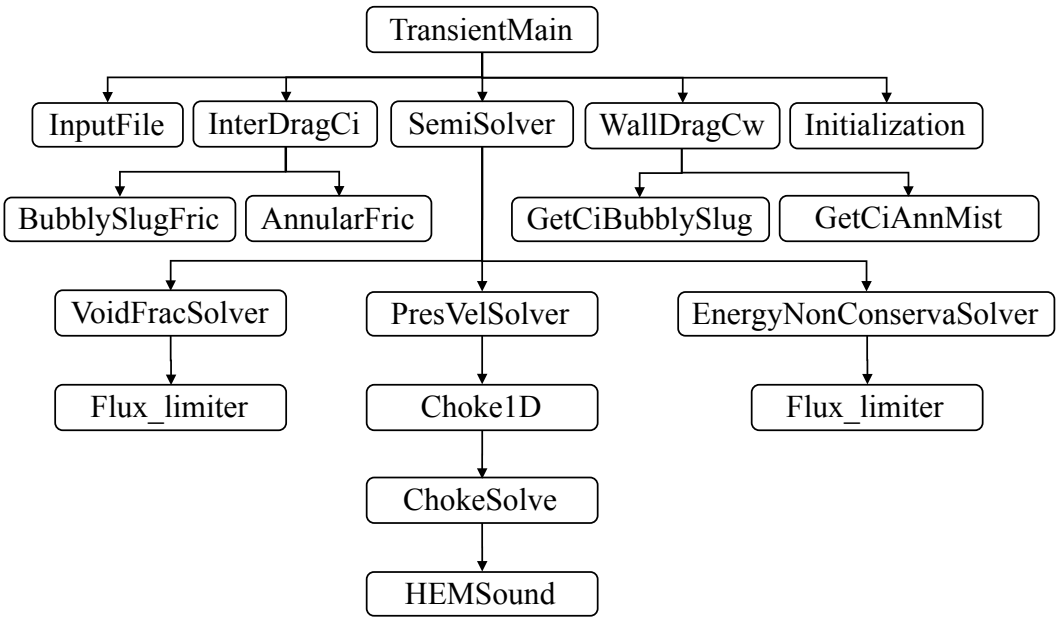

Figure A-1 Schematic about subroutines

TransientMain	Main driver of program. Call the InputFile, Initialization, InterDragCi, WallDragCw, SemiSolver subroutines and attempts to execute sequential programs.
InputFile	Read basic parameters including initial time step, total number of mesh, boundary and initial conditions, convergence criterion and maximum iterative number and so on.
Initialization	Initialize the program parameters, boundary and initial conditions, defines geometry of the nozzle in detail (for example, inlet, throat and outlet diameters and length of inlet straight, converging and diverging sections).
InterDragCi	Calculate the interfacial drag coefficients based on donor cell property parameters for different two-phase flow regimes.
WallDragCw	Calculate the wall friction coefficients based on donor cell property parameters for different two-phase flow regimes.

SemiSolver	Calculate the pressure, vapor and liquid velocity, void fraction, vapor and liquid temperature, mass transfer based on heat transfer model; and Call the PresVelSolver, VoidFracSolver and EnergyNonConservaSolver subroutines
PresVelSolver	Calculate the pressure, vapor and liquid velocity using two-phase SIMPLE iterative method, and Call the Chok1D subroutine to check whether choking flow happens or not.
VoidFracSolver	Calculate the void fraction based on mass conservation equations. Call the flux_limiter subroutine to adopt the Lax-wendroff scheme with different flux limiter and to discrete the mass equations
EnergyNonConservaSolver	Solve the two-phase energy equations and mass transfer based on heat transfer model; Call the flux_limiter subroutine to adopt the Lax-wendroff scheme with different flux limiter and to discrete the energy equations; Call the InterHfgAi subroutine to calculate the heat transfer coefficients and flashing model coefficients for different flow regions.
Chok1D	Calculate the property parameters (for example, P, α, α_D, ρ_k, V_g ,V_f , V_D and so on) at the upstream cell where the choking flow happens and Call ChokeSolve subroutine to check whether choking flow happens or not and calculate the choking velocities of vapor and liquid.
ChokeSolve	Calculate the choking velocities of vapor and liquid based on characteristic analysis approach. Call the HEMSound subroutine to obtain property parameters at the edge where the choking flow happens.
HEMSound	Solve the property parameters at the edge where the choking flow happens based on parameters at the upstream cell and the equilibrium condition indicator (iequil=-1,0,1,100), for example, complete nonequilibrium (frozen model) for iequil=-1,stagnation conditions in sound computed under nonequilibrium for iequil= 0, complete equilibrium for iequil= 1, iequil = 100 for flag that indicates that equilibrium stagnation conditions were not found by HEMSound.
Flux_limiter	Lax_Wendroff with different flux limiter for convection terms, SpaceMethod=0 for upwind scheme, SpaceMethod=1 for Traditional Lax_Wendroff scheme, SpaceMethod=2 for Second-order ENO scheme, SpaceMethod=3 for Van Leer 2 scheme and SpaceMethod=4 for OSPRE scheme.
WaterProp/IAPWS_IF97	Water and steam table to calculate the property parameters.

B. NOZZLE STEAM FLOW TABLES

Nozzle inlet pressure = 2MPa.

Case	αl_inlet	αD_inlet	m_v	V_g	m_l	V_l	m_D	V_D	m_N	V_N
			kg/s	m/s	kg/s	m/s	kg/s	m/s	kg/s	m/s
A200	0.0%	0.0%	0.8976	753.22	0	0	0.0016	300	0.0875	753.22
A201	0.0%	1.0%	0.8946	736.88	0	0	0.0761	143.04	0.0839	736.88
A202	0.0%	2.0%	0.9204	727.58	0	0	0.1765	108.11	0.0831	727.58
A203	0.0%	3.0%	0.9559	713.96	0	0	0.3093	108.57	0.0821	713.96
A204	0.0%	4.0%	0.9757	690.96	0	0	0.5153	111.86	0.0792	690.96
A205	0.0%	5.0%	0.9735	672.5	0	0	0.6651	111.08	0.0764	672.5
A210	1.0%	0.0%	0.9017	736.5	0.0098	81.18	0.0347	300	0.0849	736.5
A211	1.0%	1.0%	0.9233	724.46	0.0117	82.87	0.122	118.74	0.0835	724.46
A212	1.0%	2.0%	0.9534	715.02	0.0105	84.6	0.2287	108.04	0.0827	715.02
A213	1.0%	3.0%	0.9782	692.72	0.0053	88.56	0.4371	112.36	0.08	692.72
A214	1.0%	4.0%	0.9768	675.17	0.0049	87.72	0.5809	111.85	0.0774	675.17
A215	1.0%	5.0%	0.976	655.81	0.0046	86.72	0.7464	111.22	0.0745	655.81
A220	2.0%	0.0%	0.9176	732.49	0.0222	69.6	0.066	269.56	0.0847	732.49
A221	2.0%	1.0%	0.9403	721.2	0.0253	70.83	0.1543	112.26	0.0833	721.2
A222	2.0%	2.0%	0.9805	704.09	0.0125	76.78	0.3444	113.98	0.0818	704.09
A223	2.0%	3.0%	0.9797	685.57	0.0124	75.94	0.4932	113.2	0.079	685.57
A224	2.0%	4.0%	0.9788	666.71	0.0114	75.03	0.6515	112.51	0.0762	666.71
A225	2.0%	5.0%	0.9275	609.6	0.0004	72.4	1.0574	110.04	0.0672	609.6
A230	3.0%	0.0%	0.9153	721.46	0.0065	64.03	0.144	136.8	0.0831	721.46
A231	3.0%	1.0%	0.978	716.17	0.0202	72.21	0.2426	115.65	0.0835	716.17
A232	3.0%	2.0%	0.9788	697.99	0.02	71.42	0.3862	113.93	0.0808	697.99
A233	3.0%	3.0%	0.979	679.77	0.0185	70.58	0.537	113.21	0.0782	679.77
A234	3.0%	4.0%	0.9314	623.98	0.0008	68.08	0.935	110.89	0.0694	623.98
A235	3.0%	5.0%	0.9261	610.82	0.0012	67.79	1.0462	110.08	0.0674	610.82
A240	4.0%	0.0%	0.9533	727.37	0.0454	63.09	0.1283	235.87	0.0847	727.37
A241	4.0%	1.0%	0.9759	711.59	0.0266	69.13	0.2722	115	0.0828	711.59
A242	4.0%	2.0%	0.9779	694.28	0.0244	68.35	0.4133	113.79	0.0803	694.28
A243	4.0%	3.0%	0.9796	674.08	0.0245	67.5	0.5822	113.04	0.0773	674.08
A244	4.0%	4.0%	0.9317	621.44	0.0014	65.43	0.9603	110.66	0.0691	621.44
A245	4.0%	5.0%	0.9224	601.77	0.0015	64.99	1.1226	109.49	0.066	601.77
A250	5.0%	0.0%	0.9984	728.24	0.0411	65.83	0.1641	173.07	0.0859	728.24
A251	5.0%	1.0%	0.9921	711.19	0.0438	66.17	0.2856	113.52	0.083	711.19
A252	5.0%	2.0%	0.9783	690.17	0.0294	66.33	0.4451	113.57	0.0797	690.17
A253	5.0%	3.0%	0.9429	658.44	0.0045	64.84	0.6681	112.64	0.0748	658.44
A254	5.0%	4.0%	0.9289	618.06	0.002	63.77	0.9927	110.44	0.0684	618.06
A255	5.0%	5.0%	0.9191	594.95	0.0019	63.26	1.1811	109.03	0.0649	594.95

Nozzle inlet pressure = 3MPa.

Case	αl_inlet	αD_inlet	m_v	V_g	m_l	V_l	m_D	V_D	m_N	V_N
			kg/s	m/s	kg/s	m/s	kg/s	m/s	kg/s	m/s
A300	0.0%	0.0%	1.31	759.89	0	0	0.0016	300	0.1435	759.89
A301	0.0%	1.0%	1.2921	742.05	0	0	0.096	162.23	0.1366	742.05
A302	0.0%	2.0%	1.3165	733.02	0	0	0.2137	125.25	0.135	733.02
A303	0.0%	3.0%	1.3432	720.06	0	0	0.3571	123.91	0.133	720.06
A304	0.0%	4.0%	1.3705	707.61	0	0	0.5002	124.63	0.131	707.61
A305	0.0%	5.0%	1.4243	687.56	0	0	0.7632	129.87	0.1277	687.56
A310	1.0%	0.0%	1.2951	741.26	0.0048	97.89	0.0409	300	0.1383	741.26
A311	1.0%	1.0%	1.3253	730.78	0.0069	98.45	0.1446	138.38	0.136	730.78
A312	1.0%	2.0%	1.3486	721.01	0.006	99.45	0.2693	123.83	0.1343	721.01
A313	1.0%	3.0%	1.389	705.97	0.0038	101.94	0.4495	126.53	0.1321	705.97
A314	1.0%	4.0%	1.4282	690.4	0.0019	106.1	0.6571	130.59	0.1294	690.4
A315	1.0%	5.0%	1.4212	674.45	0.0017	105.33	0.8234	129.83	0.1254	674.45
A320	2.0%	0.0%	1.3095	729.42	0.0012	85.56	0.1487	180.21	0.1359	729.42
A321	2.0%	1.0%	1.3426	727.97	0.017	84.18	0.1793	130.93	0.1359	727.97
A322	2.0%	2.0%	1.3716	717.24	0.014	85.41	0.3144	124.99	0.1342	717.24
A323	2.0%	3.0%	1.4365	700.61	0.0055	92.09	0.5546	131.77	0.1321	700.61
A324	2.0%	4.0%	1.4302	683.94	0.005	91.59	0.7276	131.01	0.1279	683.94
A325	2.0%	5.0%	1.4252	667.78	0.0046	90.95	0.9017	130.27	0.1239	667.78
A330	3.0%	0.0%	1.3388	735.5	0.0207	78.93	0.1089	255.94	0.1384	735.5
A331	3.0%	1.0%	1.3668	725.6	0.0225	79.92	0.2255	127.48	0.1362	725.6
A332	3.0%	2.0%	1.4362	710.74	0.0084	87.64	0.4475	133.18	0.1346	710.74
A333	3.0%	3.0%	1.4318	694.41	0.008	86.87	0.6152	132.26	0.1306	694.41
A334	3.0%	4.0%	1.4284	680.82	0.0072	86.4	0.7617	131.78	0.1272	680.82
A335	3.0%	5.0%	1.4226	661.14	0.0071	85.12	0.9729	130.28	0.1222	661.14
A340	4.0%	0.0%	1.3276	723.58	0.0052	76.38	0.2289	153.8	0.1349	723.58
A341	4.0%	1.0%	1.3816	723.51	0.0319	76.86	0.2524	126.37	0.1361	723.51
A342	4.0%	2.0%	1.428	708.5	0.0103	84.71	0.464	133.52	0.1339	708.5
A343	4.0%	3.0%	1.4261	691.72	0.0099	83.82	0.6396	132.47	0.1298	691.72
A344	4.0%	4.0%	1.4237	676.76	0.0091	83.08	0.8015	131.68	0.1261	676.76
A345	4.0%	5.0%	1.3653	641.89	0.0011	81	1.0996	130.82	0.1168	641.89
A350	5.0%	0.0%	1.3725	731.77	0.0392	74.17	0.1711	243	0.1384	731.77
A351	5.0%	1.0%	1.4065	720.69	0.035	76.42	0.2966	127.74	0.1361	720.69
A352	5.0%	2.0%	1.421	704.48	0.0125	82.43	0.4992	133.1	0.1328	704.48
A353	5.0%	3.0%	1.4213	688.6	0.0118	81.59	0.6698	132.2	0.129	688.6
A354	5.0%	4.0%	1.4175	668.35	0.0126	80.15	0.8834	130.52	0.1239	668.35
A355	5.0%	5.0%	1.4198	655.88	0.0094	79.77	1.0359	130.51	0.1209	655.88

Nozzle inlet pressure = 4MPa.

Case	αl_inlet	αD_inlet	m_v	V_g	m_l	V_l	m_D	V_D	m_N	V_N
			kg/s	m/s	kg/s	m/s	kg/s	m/s	kg/s	m/s
A400	0.0%	0.0%	1.7033	762.28	0	0	0.0016	300	0.2062	762.28
A401	0.0%	1.0%	1.6747	740.09	0	0	0.158	161.95	0.1945	740.09
A402	0.0%	2.0%	1.7275	731.06	0	0	0.3065	140.34	0.1934	731.06
A403	0.0%	3.0%	1.7355	715.51	0	0	0.4898	140.38	0.1887	715.51
A404	0.0%	4.0%	1.7698	706.97	0	0	0.6162	139.6	0.1871	706.97
A405	0.0%	5.0%	1.7437	677.47	0	0	0.9532	140.41	0.1766	677.47
A410	1.0%	0.0%	1.6987	743.23	0.0009	116.51	0.0543	296.82	0.1996	743.23
A411	1.0%	1.0%	1.7326	731.69	0.0014	115.35	0.2018	149.27	0.1955	731.69
A412	1.0%	2.0%	1.728	715.65	0.0009	116.24	0.3957	140.8	0.1898	715.65
A413	1.0%	3.0%	1.7858	705.12	0.0009	117.39	0.5587	141.72	0.1885	705.12
A414	1.0%	4.0%	1.7745	688.82	0.0007	116.77	0.7507	141.08	0.1827	688.82
A415	1.0%	5.0%	1.7669	672.38	0.0006	115.49	0.9523	140.24	0.1769	672.38
A420	2.0%	0.0%	1.6986	731.95	0.0004	99.36	0.1715	187.12	0.1951	731.95
A421	2.0%	1.0%	1.7206	725.57	0.0036	100.49	0.2718	144.15	0.193	725.57
A422	2.0%	2.0%	1.7491	712.04	0.0032	101.14	0.4485	141.93	0.1896	712.04
A423	2.0%	3.0%	1.7465	691.55	0.0023	99.33	0.6912	141.82	0.1828	691.55
A424	2.0%	4.0%	1.7861	684.3	0.0026	101.36	0.8151	141.8	0.1817	684.3
A425	2.0%	5.0%	1.8029	671.3	0.0024	101.46	0.9988	141.83	0.1778	671.3
A430	3.0%	0.0%	1.7438	737.56	0.0071	92.32	0.1292	235.75	0.1994	737.56
A431	3.0%	1.0%	1.7557	723.79	0.006	96.03	0.3151	144.04	0.1938	723.79
A432	3.0%	2.0%	1.7433	702.05	0.0041	93.37	0.5621	142.48	0.1862	702.05
A433	3.0%	3.0%	1.7523	689.73	0.0047	93.2	0.7187	141.68	0.1824	689.73
A434	3.0%	4.0%	1.8252	683.3	0.0041	96.85	0.8659	143.68	0.1826	683.3
A435	3.0%	5.0%	1.7812	662.96	0.0039	94	1.0866	141.18	0.1744	662.96
A440	4.0%	0.0%	1.7169	723.38	0.0013	89.52	0.3019	158.17	0.1926	723.38
A441	4.0%	1.0%	1.812	723.12	0.0071	95.14	0.3614	146.07	0.1958	723.12
A442	4.0%	2.0%	1.8484	710.46	0.0059	95.71	0.5457	146.41	0.1927	710.46
A443	4.0%	3.0%	1.8036	692.5	0.0061	93.67	0.7299	143.85	0.1852	692.5
A444	4.0%	4.0%	1.8177	678.93	0.0054	93.8	0.9181	143.8	0.1809	678.93
A445	4.0%	5.0%	1.7825	658.37	0.0053	90.39	1.1502	141.2	0.1729	658.37
A450	5.0%	0.0%	1.7706	734.02	0.0154	86.11	0.1959	225.39	0.1992	734.02
A451	5.0%	1.0%	1.8183	720.27	0.0083	94.1	0.4036	147.07	0.1952	720.27
A452	5.0%	2.0%	1.7694	701.84	0.009	90.23	0.588	143.1	0.1872	701.84
A453	5.0%	3.0%	1.7663	680.71	0.0076	87.89	0.8448	142.22	0.18	680.71
A454	5.0%	4.0%	1.7762	667.45	0.0071	87.87	1.0246	141.62	0.1759	667.45
A455	5.0%	5.0%	1.7907	643.03	0.0046	88.22	1.3656	142.23	0.168	643.03

Nozzle inlet pressure = 5MPa.

Case	αl_inlet	αD_inlet	m_v	V_g	m_l	V_l	m_D	V_D	m_N	V_N
			kg/s	m/s	kg/s	m/s	kg/s	m/s	kg/s	m/s
A500	0.0%	0.0%	2.0886	763.52	0	0	0.0015	300	0.2768	763.52
A501	0.0%	1.0%	2.0563	746.52	0	0	0.1015	207.2	0.2632	746.52
A502	0.0%	2.0%	2.2701	737.33	0	0	0.3277	168.06	0.2692	737.33
A503	0.0%	3.0%	2.0951	728.29	0	0	0.3816	148.19	0.2562	728.29
A504	0.0%	4.0%	2.2573	713.64	0	0	0.6556	164.57	0.2578	713.64
A505	0.0%	5.0%	2.2496	700.79	0	0	0.8361	163.7	0.2516	700.79
A510	1.0%	0.0%	2.076	745.68	0.0018	122.46	0.0456	300	0.2685	745.68
A511	1.0%	1.0%	2.2644	736.62	0.0002	139.34	0.2243	180.01	0.271	736.62
A512	1.0%	2.0%	2.2591	725.15	0.0002	138.58	0.3965	165.24	0.265	725.15
A513	1.0%	3.0%	2.2525	713.32	0.0003	137.81	0.5599	164.45	0.2593	713.32
A514	1.0%	4.0%	2.2451	700.47	0.0002	136.95	0.7398	163.59	0.2531	700.47
A515	1.0%	5.0%	2.1813	691.74	0.001	126.62	0.8367	151.41	0.2462	691.74
A520	2.0%	0.0%	2.2625	745.42	0.0009	120.53	0.0951	242.98	0.2762	745.42
A521	2.0%	1.0%	2.2603	734.26	0.001	120.08	0.2607	173.64	0.2697	734.26
A522	2.0%	2.0%	2.255	724.59	0.0016	119.67	0.4036	165.1	0.2647	724.59
A523	2.0%	3.0%	2.2472	709.19	0.0008	118.98	0.6151	164.16	0.2573	709.19
A524	2.0%	4.0%	2.2394	695.86	0.0007	118.37	0.802	163.26	0.2509	695.86
A525	2.0%	5.0%	2.2281	674.75	0.0003	117.34	1.1021	161.82	0.2409	674.75
A530	3.0%	0.0%	2.0819	728.42	0.0005	104.61	0.2613	167.65	0.2588	728.42
A531	3.0%	1.0%	2.257	733.34	0.0036	112.49	0.2764	171.51	0.2692	733.34
A532	3.0%	2.0%	2.2514	723.5	0.0043	112.1	0.4191	164.93	0.2641	723.5
A533	3.0%	3.0%	2.2425	706.63	0.0015	111.49	0.6523	163.96	0.2561	706.63
A534	3.0%	4.0%	2.2332	689.43	0.0008	110.84	0.8931	162.82	0.2479	689.43
A535	3.0%	5.0%	2.2228	672.92	0.0005	110.22	1.1305	161.66	0.2399	672.92
A540	4.0%	0.0%	2.1264	737.42	0.0095	96.12	0.1617	266.06	0.2669	737.42
A541	4.0%	1.0%	2.2539	731.7	0.007	108.28	0.3021	168.8	0.2683	731.7
A542	4.0%	2.0%	2.246	718.44	0.0034	107.88	0.4914	164.66	0.2617	718.44
A543	4.0%	3.0%	2.2395	708.74	0.0048	107.55	0.6262	163.97	0.2569	708.74
A544	4.0%	4.0%	2.232	697.9	0.0051	107.16	0.7788	163.22	0.2516	697.9
A545	4.0%	5.0%	2.2174	671.15	0.0008	106.35	1.159	161.51	0.2389	671.15
A550	5.0%	0.0%	2.144	735.36	0.0112	94.25	0.2024	250.84	0.2667	735.36
A551	5.0%	1.0%	2.2505	729.68	0.0103	105.59	0.3333	166.61	0.2672	729.68
A552	5.0%	2.0%	2.2422	717.2	0.0058	105.27	0.511	164.5	0.261	717.2
A553	5.0%	3.0%	2.234	704.23	0.0043	104.9	0.6919	163.69	0.2547	704.23
A554	5.0%	4.0%	2.2218	682.3	0.0011	104.27	1.0001	162.3	0.2443	682.3
A555	5.0%	5.0%	2.2123	669.76	0.0012	103.9	1.182	161.39	0.2382	669.76

Nozzle inlet pressure = 6MPa.

Case	αl_inlet	αD_inlet	m_v	V_g	m_l	V_l	m_D	V_D	m_N	V_N
			kg/s	m/s	kg/s	m/s	kg/s	m/s	kg/s	m/s
A600	0.0%	0.0%	2.4635	763.48	0	0	0.0015	300	0.3553	763.48
A601	0.0%	1.0%	2.7	747.87	0	0	0.1651	216.94	0.355	747.87
A602	0.0%	2.0%	2.6965	737.21	0	0	0.3465	180.59	0.3473	737.21
A603	0.0%	3.0%	2.4598	726.86	0	0	0.4178	159.15	0.3272	726.86
A604	0.0%	4.0%	2.682	712.82	0	0	0.7265	176.32	0.332	712.82
A605	0.0%	5.0%	2.5064	703.75	0	0	0.7915	160.45	0.3172	703.75
A610	1.0%	0.0%	2.686	749.08	0.0001	152.36	0.0627	300	0.359	749.08
A611	1.0%	1.0%	2.6889	736.37	0.0001	151.6	0.2403	192.87	0.3495	736.37
A612	1.0%	2.0%	2.6833	724.85	0.0001	150.77	0.433	177.08	0.3416	724.85
A613	1.0%	3.0%	2.6761	713.78	0.0002	149.98	0.605	176.27	0.3347	713.78
A614	1.0%	4.0%	2.5294	703.9	0.0005	136.78	0.697	161.18	0.321	703.9
A615	1.0%	5.0%	2.6595	692.58	0.0002	148.39	0.9434	174.75	0.3212	692.58
A620	2.0%	0.0%	2.4362	732.16	0.0003	121.98	0.199	190.78	0.3331	732.16
A621	2.0%	1.0%	2.6837	734.22	0.0005	131.36	0.2782	186.41	0.3479	734.22
A622	2.0%	2.0%	2.6772	721.94	0.0004	130.79	0.4769	176.82	0.3398	721.94
A623	2.0%	3.0%	2.6686	707.27	0.0003	130.13	0.7043	175.83	0.3307	707.27
A624	2.0%	4.0%	2.5458	700.67	0.0017	118.68	0.7564	161.94	0.3203	700.67
A625	2.0%	5.0%	2.6531	691.26	0.0007	129.26	0.964	174.61	0.3204	691.26
A630	3.0%	0.0%	2.6822	741.6	0.0007	123.56	0.1563	219.31	0.3533	741.6
A631	3.0%	1.0%	2.6787	732.23	0.0012	123.26	0.3168	182.01	0.3464	732.23
A632	3.0%	2.0%	2.6719	721.11	0.0011	122.84	0.4938	176.71	0.3392	721.11
A633	3.0%	3.0%	2.6628	706.82	0.0006	122.37	0.7161	175.75	0.3303	706.82
A634	3.0%	4.0%	2.6518	688.56	0.0004	121.6	1.0015	174.48	0.3191	688.56
A635	3.0%	5.0%	2.6414	675.76	0.0004	121.07	1.2092	173.52	0.311	675.76
A640	4.0%	0.0%	2.4503	723.83	0.0006	110.94	0.3532	166.97	0.3287	723.83
A641	4.0%	1.0%	2.6737	730.22	0.002	118.83	0.3554	179.22	0.345	730.22
A642	4.0%	2.0%	2.6654	716.48	0.001	118.42	0.5687	176.41	0.3363	716.48
A643	4.0%	3.0%	2.6553	700.23	0.0006	117.93	0.8208	175.31	0.3262	700.23
A644	4.0%	4.0%	2.6457	687.72	0.0006	117.48	1.0198	174.4	0.3184	687.72
A645	4.0%	5.0%	2.6392	684.71	0.0015	117.28	1.0743	174.1	0.3161	684.71
A650	5.0%	0.0%	2.5101	734.07	0.0058	103.41	0.2211	247.72	0.3407	734.07
A651	5.0%	1.0%	2.6686	728.19	0.003	116	0.393	177.67	0.3435	728.19
A652	5.0%	2.0%	2.6603	715.77	0.002	115.69	0.585	176.31	0.3357	715.77
A653	5.0%	3.0%	2.6498	700.19	0.001	115.3	0.8275	175.27	0.326	700.19
A654	5.0%	4.0%	2.6384	684.04	0.0007	114.8	1.0827	174.12	0.316	684.04
A655	5.0%	5.0%	2.6277	672.34	0.0007	114.43	1.274	173.22	0.3085	672.34

Nozzle inlet pressure = 7MPa.

Case	αl_inlet	αD_inlet	m_v	V_g	m_l	V_l	m_D	V_D	m_N	V_N
			kg/s	m/s	kg/s	m/s	kg/s	m/s	kg/s	m/s
A700	0.0%	0.0%	2.8275	762.08	0	0	0.0015	300	0.4424	762.08
A701	0.0%	1.0%	3.1185	745.89	0	0	0.171	229.95	0.4447	745.89
A702	0.0%	2.0%	3.1162	735.38	0	0	0.3639	191.65	0.4351	735.38
A703	0.0%	3.0%	3.1098	724.26	0	0	0.5567	187.75	0.426	724.26
A704	0.0%	4.0%	3.1017	712.46	0	0	0.759	186.89	0.4166	712.46
A705	0.0%	5.0%	3.0921	699.77	0	0	0.9815	185.94	0.4065	699.77
A710	1.0%	0.0%	2.7758	742.4	0.0002	144.93	0.0534	300	0.4251	742.4
A711	1.0%	1.0%	3.1063	734.34	0.0001	162.61	0.2594	203.11	0.4375	734.34
A712	1.0%	2.0%	3.1012	724.49	0.0001	161.83	0.4423	187.88	0.4289	724.49
A713	1.0%	3.0%	3.0934	711.89	0.0001	160.84	0.6573	186.75	0.4188	711.89
A714	1.0%	4.0%	3.0852	702.34	0.0001	160.08	0.8255	186.02	0.411	702.34
A715	1.0%	5.0%	3.0756	691.8	0.0002	159.22	1.0143	185.22	0.4024	691.80
A720	2.0%	0.0%	2.7847	730.61	0.0003	131.4	0.2011	199.37	0.4138	730.61
A721	2.0%	1.0%	3.0998	732.11	0.0003	141.69	0.303	196.41	0.4355	732.11
A722	2.0%	2.0%	3.0938	721.5	0.0003	141.16	0.4939	187.4	0.4265	721.5
A723	2.0%	3.0%	3.0855	709.46	0.0003	140.54	0.7001	186.54	0.4168	709.46
A724	2.0%	4.0%	3.0763	697.87	0.0003	139.95	0.9042	185.67	0.4074	697.87
A725	2.0%	5.0%	3.0635	680.33	0.0003	138.93	1.2113	184.37	0.3936	680.33
A730	3.0%	0.0%	2.8215	735.78	0.0016	117.91	0.1431	279.49	0.4232	735.78
A731	3.0%	1.0%	3.0935	730.02	0.0005	133.28	0.348	191.96	0.4335	730.02
A732	3.0%	2.0%	3.0867	719.3	0.0005	132.87	0.5357	187.22	0.4246	719.3
A733	3.0%	3.0%	3.0785	708.91	0.0006	132.44	0.7155	186.46	0.4162	708.91
A734	3.0%	4.0%	3.0673	693.15	0.0004	131.83	0.9895	185.32	0.4036	693.15
A735	3.0%	5.0%	3.0548	678.03	0.0004	131.12	1.2565	184.17	0.3916	678.03
A740	4.0%	0.0%	2.7993	723.04	0.0005	119.99	0.3547	177.35	0.4088	723.04
A741	4.0%	1.0%	3.087	727.51	0.0008	128.68	0.4001	189.01	0.4312	727.51
A742	4.0%	2.0%	3.0793	716.02	0.0007	128.31	0.5969	186.98	0.4218	716.02
A743	4.0%	3.0%	3.0717	708.13	0.0011	127.95	0.7355	186.37	0.4153	708.13
A744	4.0%	4.0%	3.0594	691.26	0.0005	127.47	1.0282	185.17	0.4019	691.26
A745	4.0%	5.0%	3.0466	676.42	0.0005	126.89	1.2909	184.03	0.39	676.42
A750	5.0%	0.0%	2.8633	731.34	0.0028	112.15	0.2403	243.12	0.4223	731.34
A751	5.0%	1.0%	3.0806	725.41	0.0011	125.76	0.4438	187.83	0.4292	725.41
A752	5.0%	2.0%	3.0723	713.98	0.0009	125.45	0.6382	186.82	0.42	713.98
A753	5.0%	3.0%	3.0634	703.87	0.001	125.11	0.8142	186.07	0.4118	703.87
A754	5.0%	4.0%	3.0516	689.65	0.0007	124.71	1.0628	185.03	0.4004	689.65
A755	5.0%	5.0%	3.0461	688.67	0.0023	124.29	1.0878	184.82	0.3991	688.67

Nozzle inlet pressure = 8MPa.

Case	αl_inlet	αD_inlet	m_v	V_g	m_l	V_l	m_D	V_D	m_N	V_N
			kg/s	m/s	kg/s	m/s	kg/s	m/s	kg/s	m/s
A800	0.0%	0.0%	3.1822	759.87	0	0	0.0015	300	0.538	759.87
A801	0.0%	1.0%	3.5268	743.56	0	0	0.1631	247.4	0.5448	743.56
A802	0.0%	2.0%	3.5273	732.33	0	0	0.3777	201.75	0.5326	732.33
A803	0.0%	3.0%	3.5216	722.49	0	0	0.565	197.32	0.5228	722.49
A804	0.0%	4.0%	3.5133	708.9	0	0	0.8175	196.32	0.5098	708.9
A805	0.0%	5.0%	3.504	699.37	0	0	0.9999	195.56	0.5004	699.37
A810	1.0%	0.0%	3.1165	739.54	0.0001	154.35	0.0562	300	0.5157	739.54
A811	1.0%	1.0%	3.5145	731.95	0.0001	172.69	0.261	215.21	0.536	731.95
A812	1.0%	2.0%	3.5106	721.67	0.0001	171.82	0.4661	197.45	0.5251	721.67
A813	1.0%	3.0%	3.5036	712.26	0.0001	171.03	0.6432	196.42	0.5159	712.26
A814	1.0%	4.0%	3.4951	702.32	0.0002	170.18	0.8328	195.65	0.5061	702.32
A815	1.0%	5.0%	3.4823	684.2	0.0002	168.56	1.1745	194.28	0.4887	684.20
A820	2.0%	0.0%	3.1238	728.37	0.0003	140.06	0.1951	211.76	0.5029	728.37
A821	2.0%	1.0%	3.5071	729.35	0.0002	151.25	0.3156	206.64	0.5331	729.35
A822	2.0%	2.0%	3.5017	718.01	0.0003	150.65	0.5351	196.86	0.5215	718.01
A823	2.0%	3.0%	3.4942	708.72	0.0003	150.13	0.7111	196.14	0.5124	708.72
A824	2.0%	4.0%	3.4846	697.9	0.0003	149.5	0.9158	195.31	0.5018	697.9
A825	2.0%	5.0%	3.4717	681.77	0.0003	148.52	1.223	194.07	0.4862	681.77
A830	3.0%	0.0%	3.1634	732.43	0.0008	126.47	0.1523	276.56	0.513	732.43
A831	3.0%	1.0%	3.4997	727.16	0.0004	142.64	0.367	201.69	0.5305	727.16
A832	3.0%	2.0%	3.4936	717.64	0.0004	142.24	0.5496	196.79	0.5208	717.64
A833	3.0%	3.0%	3.484	703.24	0.0004	141.64	0.8171	195.74	0.507	703.24
A834	3.0%	4.0%	3.4731	690.68	0.0004	141.04	1.0552	194.77	0.4948	690.68
A835	3.0%	5.0%	3.4616	679.66	0.0004	140.5	1.2699	193.88	0.4839	679.66
A840	4.0%	0.0%	3.141	720.17	0.0006	128.32	0.3699	186.25	0.4966	720.17
A841	4.0%	1.0%	3.4922	725.07	0.0006	137.93	0.4165	198.88	0.528	725.07
A842	4.0%	2.0%	3.4854	715.66	0.0006	137.57	0.5938	196.62	0.5187	715.66
A843	4.0%	3.0%	3.4754	702.63	0.0005	137.15	0.8371	195.67	0.506	702.63
A844	4.0%	4.0%	3.4635	688.67	0.0005	136.6	1.1009	194.6	0.4925	688.67
A845	4.0%	5.0%	3.4519	678.04	0.0005	136.15	1.3089	193.74	0.4819	678.04
A850	5.0%	0.0%	3.4893	729.48	0.0005	135.25	0.335	204.37	0.5326	729.48
A851	5.0%	1.0%	3.4846	723.04	0.0008	134.93	0.464	197.48	0.5257	723.04
A852	5.0%	2.0%	3.4771	713.2	0.0008	134.62	0.6475	196.43	0.516	713.2
A853	5.0%	3.0%	3.4693	705.95	0.0012	134.17	0.7861	195.82	0.5087	705.95
A854	5.0%	4.0%	3.4539	686.62	0.0006	133.79	1.148	194.43	0.4901	686.62
A855	5.0%	5.0%	3.4423	676.62	0.0006	133.39	1.3445	193.62	0.4801	676.62

C. LIST OF PUBLICATIONS SUPPORTED BY THE PROJECT

1. W. Zhang, D. Wang, A. Renganathan, H. Zhang, "Modeling and assessment of two-phase transonic steam flow with condensation through the convergent-divergent nozzle," Nuclear Engineering and Design, (2020).

   https://doi.org/10.1016/j.nucengdes.2020.110632

2. W. Zhang, D. Wang, "Development and Implementation of a Mechanistic Reactor Core Isolation Cooling System Model for the Extended Station Black-out Accident," (in preparation).

The Texas A&M University PI and graduate student plan to write the following manuscripts for submission to journals based on the efforts described in this report.

- Development of a Buoyancy-induced Stratified Wetwell Model
  - Description of model development
  - Simulation results from pool heater experiment and POOLEX STB-20, both experiments in which the steam injection rate was low and buoyancy was the primary force inducing mixing.
  - Journals under consideration: Annals of Nuclear Engineering or Progress in Nuclear Energy
- Modeling of a Stratified Wetwell with Both Buoyancy and Momentum Mixing Effects
  - Description of model development to include momentum-driven mixing in the water pool.
  - Simulation results from the POOLEX experiments with higher steam mass flow rates and significant mixing effects due to inlet momentum.
  - Possibly simulate experiments conducted as part of Matt Solom's dissertation [5].
- RELAP-7 RCIC system implementation
  - Description of turbine and pump model implementation into RELAP-7
  - Validation against available data